Wave propagation in mechanical metamaterials

Zhou, Y.; Zhou Y.

WAVE PROPAGATION IN MECHANICAL METAMATERIALS

PROEFSCHRIFT

ter verkrijging van
de graad van Doctor aan de Universiteit Leiden,
op gezag van Rector Magnificus prof. mr. C.J.J.M. Stolker,
volgens besluit van het College voor Promoties
te verdedigen op dinsdag 17 oktober 2017
klokke 10.00 uur

door

Yujie Zhou

geboren te HANGZHOU, CHINA in 1987

Promotor:	prof. dr. V. Vitelli
Promotiecommissie:	prof. dr. C. W. J. Beenakker
	prof. dr. E. R. Eliel
	dr. M. Fruchart
	dr. W. T. M. Irvine (University of Chicago)
	prof. dr. H. Schiessel

Casimir PhD series 2017-32
ISBN 978-90-8593-316-8
An electronic version of this thesis is available at the Leiden University Repository (https://openaccess.leidenuniv.nl).

The research done for this thesis was conducted at the Lorentz Institute, Leiden University. The author was sponsored by the China Scholarship Council (CSC).

The cover shows a sketch originally produced in the research process of this thesis. The sketch is a twisted kagome lattice with the twisting angle $\theta = 45^\circ$. The arrows indicate one of the four finite-frequency vibrational modes at the four-band crossing at the Γ point in Fig. 4.9. Some zigzag lines along three directions are marked in the colors of red, green, and blue. These lines give a hint to the physical reason for the doubly degenerate band structure.

The colored lines were drawn freehand on a piece of paper printed with a kagome framework. They were drawn by the author and dr. M. Fruchart during a discussion. The source code for the framework and mode analysis is credited to dr. J. Paulose.

Contents

Chapter 1

Introduction

People conventionally use simple mechanical properties to classify states of matters: a solid maintains both fixed volume and shape, a liquid maintains a fixed volume but has a variable shape, and a gas has both variable volume and shape [1]. In recent years, new forms of matter called mechanical metamaterials appeared with unique properties [2–14]. Such metamaterials are artificial structures with effective mechanical properties that qualitatively differ from those of their base materials. An example from this thesis is the mechanical kagome lattice model shown in Fig. 1.1. This model has a free mechanism for deformation so that it does not maintain either shape or volume. This is a mechanical property that is independent of the LEGO base materials of solid plastics.

Structure determines properties [15]. The structure of mechanical metamaterials begins with repeating unit cells as building blocks. Each unit cell can be regarded as a tiny mechanical device transforming input forces and motions into a designed set of output forces and motions. The unit cells are connected to each other, forming a whole piece of material. In this way, the inputs and outputs of the unit cells are synthesized into an ordered pattern, which is just the macroscopic response of a metamaterial to a given macroscopic input. This macroscopic response can be described by linear waves [16, 17], solitary waves [18–20], or non-wavelike mechanical motions [4, 5, 9, 21]. Theoretical understanding of this physical process is indispensable for designing the structures and controlling the properties of metamaterials.

(a) **(b)**

Figure 1.1. Model of a mechanical metamaterial: twisted kagome lattice. As all the small triangles twist together, the whole structure in (**a**) contracts to the one in (**b**).

Mechanical metamaterials can affect the propagation of linear sound waves. Such acoustic metamaterials (c.f., electromagnetic metamaterials) can display special properties such as negative refractive indices that provide functionalities in acoustic cloaking devices [16, 22, 23]. In contrast with these linear-wave-based metamaterials, one can also consider mechanical metamaterials that involve large nonlinear deformations [1]. When mechanical stimuli are applied to the materials, their building blocks can display motions of rotation, twist, etc., with large amplitudes, which lead to significant changes of shape and volume of the whole system. This behavior of "large responses for small perturbations" is a key feature of *soft matter* [24].

In the past few years, the concept of topological phases was introduced into the field of mechanical metamaterials, leading to the so-called *topological mechanical metamaterials* [25, 26]. This concept not only merges the features of both acoustic waves and large deformations into one system, but also creates a link between the study of mechanical metamaterials and modern condensed matter physics. This thesis will explore the interplay between nonlinearities and the topological properties of mechanical metamaterials. First, we explain the topological phases in the next section.

[1] Sometimes they are simply referred to as *mechanical metamaterials* in a narrower sense, as opposed to acoustic metamaterials. In this thesis, we use the broader definition.

1.1 Topological mechanical metamaterials

We focus on the topological rotor chain as an example of topological mechanical metamaterials [2]. It is a chain of classical rotors connected by springs (see Fig. 1.2). The angles θ_n of the rotors are measured in an alternating fashion along the lattice, from the negative y-axis at odd-numbered sites and positive y-axis at even-numbered sites. The equilibrium angle $\overline{\theta}$ for a uniform lattice configuration can be either positive or negative, corresponding to two equilibrium states: all rotors leaning either to the right or to the left. We impose periodic boundary conditions, so the system is forbidden to switch from one equilibrium state to the other without deforming springs. In equilibrium states, all springs are at their rest length $\overline{\ell}$. When linear mechanical waves propagate in the chain, the angles θ_n oscillates around equilibrium. This causes spring deformations $\delta\ell_n$ that are determined by the displacements of the rotor angles $\delta\theta_n$. We will focus on $\delta\theta_n$ and $\delta\ell_n$ to demonstrate the idea of topological mechanics.

(a) $\overline{\theta} > 0$, right-leaning rotors **(b)** $\overline{\theta} < 0$, left-leaning rotors

Figure 1.2. Topological rotor chains with (**a**) positive and (**b**) negative equilibrium angles $\overline{\theta}$. The masses (blue dots) of rotors (black rods) rotate around fixed pivots (black crosses) and are connected to each other by springs (red dashed lines). The lattice spacing is a, the rotor length is r, and the spring equilibrium length is $\overline{\ell}$. Periodic boundary conditions are used, indicated by dangling springs at chain ends.

Because the rotors are in a one-dimensional lattice, their linear motion can be described by lattice waves. The normal modes representing a $\delta\theta$ wave

[2] B. G. Chen pointed out that a topological mechanism (essentially a rotor chain with pinning points displaced) was in one of Leonardo da Vinci's notebooks. See Ref. [27], particularly Fig. 5.

and a $\delta\ell$ wave with angular frequency ω and wave vector k are

$$\delta\theta(n,t) \propto \exp\left[i(kna - \omega t)\right], \tag{1.1}$$
$$\delta\ell(n,t) \propto \exp\left[i(kna - \omega t + \phi(k))\right] \tag{1.2}$$

where n is the nth rotor or spring along the chain, a is the lattice spacing, t is time, and $\phi(k)$ is a phase difference between a $\delta\theta$ wave and its corresponding $\delta\ell$ wave. ϕ is a crucial to the concept of topological mechanics, we will focus on it shortly after. Note that the lattice waves with wave vector k and $k + 2\pi/a$ are equivalent, because the physical quantities like $\delta\theta$ and $\delta\ell$ take values only at lattice points na, and $e^{i(2\pi/a)na} = e^{i2\pi n} = 1$.

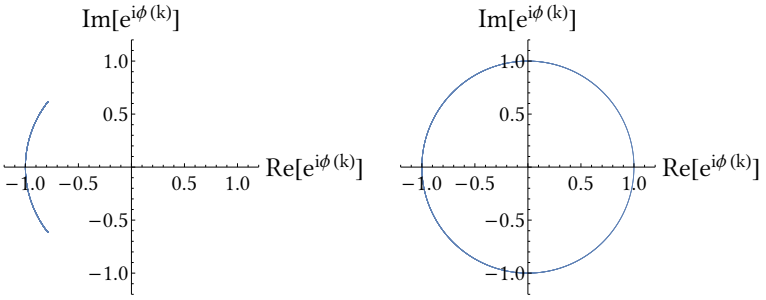

(a) $\overline{\theta} > 0$, right-leaning rotors **(b)** $\overline{\theta} < 0$, left-leaning rotors

Figure 1.3. Contour plot in the complex plane of $e^{i\phi(k)}$ for complete circuit of k from $k = 0$ to $k = 2\pi/a$. In (**a**), $e^{i\phi(k)}$ goes back and forth on the arc and indeed forms a closed loop.

As long as $\delta\theta$ and $\delta\ell$ do not vanish, the quotient $\delta\ell(k)/\delta\theta(k) \propto e^{i\phi(k)}$ is a non-zero complex number. When we tune the wave vector from $k = 0$ to $k = 2\pi/a$, in other words when we gradually decrease the wavelength from infinity to a (see Fig. 1.5 and Fig. 1.6), the phase shift between $\delta\theta$ and $\delta\ell$ waves $e^{i\phi(k)}$ runs through a closed loop on the complex plane (see Fig. 1.3). The number of times this loop turns around the origin is a *topological index*, and it has been shown [18, 25, 26] that this index is either 0 or 1, depending on which equilibrium state the chain is in (see also Eq. (1.4)). In other words, the phase of a $\delta\ell$ wave shifts by either *zero* (Fig. 1.5) or *one* (Fig. 1.6) more period

than its corresponding $\delta\theta$ wave. The correspondence between $\delta\ell$ and $\delta\theta$ as follows: we regard the $\delta\theta$ wave as $\exp[ikna]$ spatially and the $\delta\ell$ wave as $\exp[ik(na+\phi/k)]$, i.e., the effect of the phase ϕ on the $\delta\ell$ wave is a positional shift of the $\delta\theta$ wave in real space. As we will discuss later, it is the *difference* between the topological indices of the two equilibrium states of a rotor chain that make it a model of a topological mechanical material. Note that Eq. (1.1) and (1.2) make an arbitrary choice that $\delta\ell$ waves have the phase shift ϕ. We can also have $\delta\theta$ take the extra phase shift, and the reasoning remains the same.

In Fig. 1.5 and Fig. 1.6, we focus on spatial periods at $n = 0$ by thick colored lines, in order to eliminate the direct contribution of k to the phases and single out the effect of $\phi(k)$. The number of periods of extra wave shifts of $\delta\ell$ is the topological invariant.

The physical reason for this extra phase shift ϕ is the following: the deformation $\delta\ell(n,t)$ of a spring depends *asymmetrically* on the angular displacement of its two neighbor rotors, say $\delta\theta(n,t)$ and $\delta\theta(n+1,t)$. Indeed at linear order

$$\delta\ell(n,t) = -b\delta\theta(n,t) + c\delta\theta(n+1,t) \tag{1.3}$$

where b and c are prefactors that are not equal for rotor chains with $\overline{\theta} \neq 0$. Combining this equation and Eq. (1.1) and (1.2), $\delta\ell$ waves can be expressed

$$\delta\ell(n,t) \propto (c\exp[ika] - b)\delta\theta(n,t). \tag{1.4}$$

We see that the complex term $(c\exp[ika] - b)$ is the origin of the phase difference between $\delta\theta$ and $\delta\phi$ waves. This term's complex argument is just $\phi(k)$. It has been shown that the two states of right-leaning and left-leaning rotors have their b and c's values exchanged [18, 25, 26, 28]. The topological indices are defined only when $b \neq c$, i.e., the deformation depends asymmetrically on the displacements. When $b = c$, then the complex term goes to zero at $k = 0$, so the phase $\phi(k = 0)$ is not well defined, which in turn means the topological index is not well defined either [3]. The system corresponds to

[3]This is why a gapped band structure where this complex term never equals zero is necessary for a system to be "topological".

$\overline{\theta} = 0$, which is clearly symmetrical, meaning that the rotors are vertically up and down alternatively, leaning towards neither the left nor the right.

As mentioned in Ref. [25], topological indices depend on how the labels of rotors and springs are assigned. Our assignment shown in Fig. 1.5 and Fig. 1.6 produces topological indices 0 (right-leaning) and 1 (left-leaning). Other assignments may give different results. For instance, with the assignment that the nth spring connecting the $(n+1)$th and $(n+2)$th rotors (see Fig. 1.4), the same chain has topological indices 1 (right-leaning) and 2 (left-leaning). This is intuitive, since the right-leaning state and the left-leaning state are mirror symmetrical, so they cannot have intrinsic *a priori* preference in topological indices. While the topological indices depend on arbitrary choices, their differences, for example at an interface, have a well-defined physical meaning.

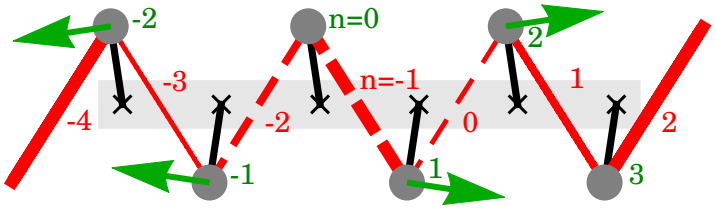

Figure 1.4. The same chain as in Fig. 1.6 but with the assignment of the nth spring connecting the $(n+1)$th and $(n+2)$th rotors. It has a topological index 2.

In the above example, the rotor chain with periodic boundary conditions is forbidden to go from one equilibrium state to the other without deforming springs. Strictly speaking, in such a case, the aforementioned assignments of labels of rotors and springs lack global consistency, because it is not possible to know whether the assignments are the same for the two states when one state cannot be *continuously* translated into the other. In other words, we have to make two assignments separately for the two states and cannot guarantee that they are consistent with each other. To avoid this, we can consider a system with positive energy so that finite spring deformation is allowed. We can also use free boundary conditions so that the two equilibrium states can be transformed into each other via zero-energy nonlinear waves, as we will see in Chapter 2. Alternatively, we can have a system with two or multiple

states put together with interfaces. In any such cases, we are able to make the assignment only once so that it is guaranteed to be consistent for all different states. Then the use of topological indices is rigorously valid.

Since Kane and Lubensky [25] introduced the concept of "band topology" into classical mechanical systems, the research of topological mechanical metamaterials has become a booming field. Many models have been proposed [13, 14, 17–19, 26, 28–46], and a universal classification of topological phonons has been provided [47]. One can map quantum mechanical problems to classical mechanics, and using spring extensions and mass displacements is not the only way of introducing topology into mechanical system. Still, we hope that the interpretation of topological phase shift in rotor chains given in this section will provide guidance in investigating wave propagation in topological mechanical systems.

This thesis will focus on linear and nonlinear propagation of waves and their interaction with impurities in mechanical metamaterials. In the next section, we present the outline of this thesis.

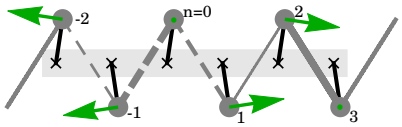

(a) $\delta\theta_n$ for $k = \frac{\pi}{3a}$, rotors right-leaning.

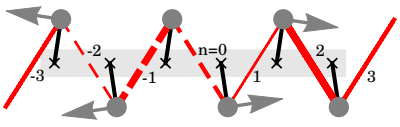

(b) $\delta\ell_n$ for $k = \frac{\pi}{3a}$, rotors right-leaning.

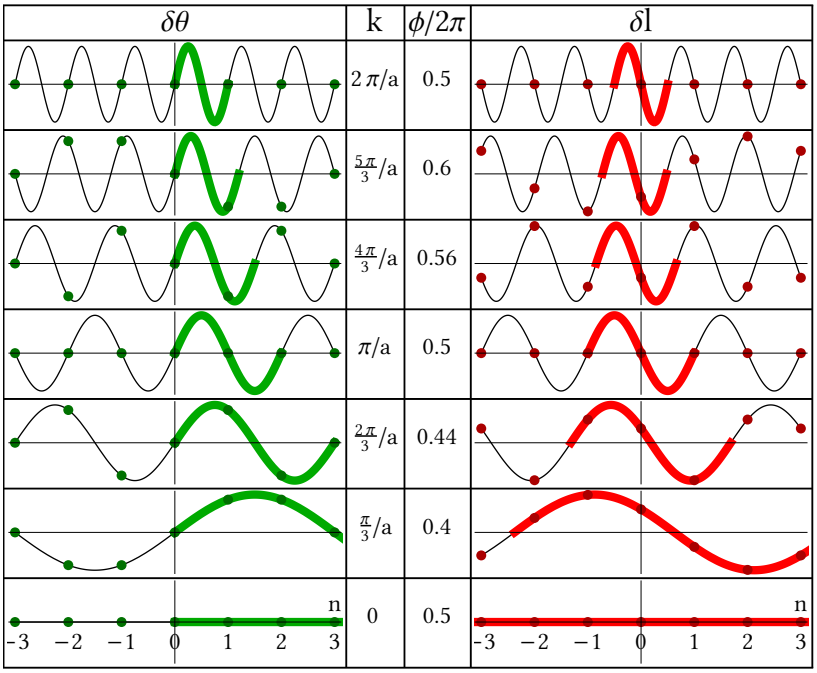

(c) Comparison of phases of $\delta\theta$ and $\delta\ell$ waves in real space with varying k.

Figure 1.5. Topological phases of a rotor chain's vibrational waves. In the configuration (**a**) and (**b**), the arrows indicate directions and amplitudes of rotor vibrations, i.e., $\delta\theta$ lattice waves, and the lines connecting rotors indicate spring deformations, i.e., $\delta\ell$ lattice waves. Dashed springs are stretched and solid springs are compressed, with their thickness proportional to deformation. In (**c**), the dots are wave values at lattice points, i.e., $\delta\theta_n$ and $\delta\ell_n$. One spatial period in the $\delta\theta$ wave and its counterpart in the $\delta\ell$ wave is emphasized by thick colored lines. The $\delta\ell$ wave stays around the same place in real space after k goes from 0 to $2\pi/a$. So the topological index of this chain with right-leaning rotors is zero. The geometrical parameters are $r/a = 0.8$ and $\bar{\theta} = +0.15$, i.e., the rotors are right-leaning.

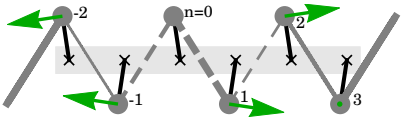

(a) $\delta\theta_n$ for $k = \frac{\pi}{3a}$, rotors left-leaning.

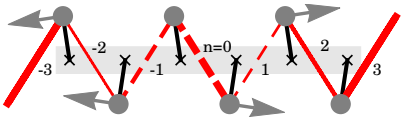

(b) $\delta\ell_n$ for $k = \frac{\pi}{3a}$, rotors left-leaning.

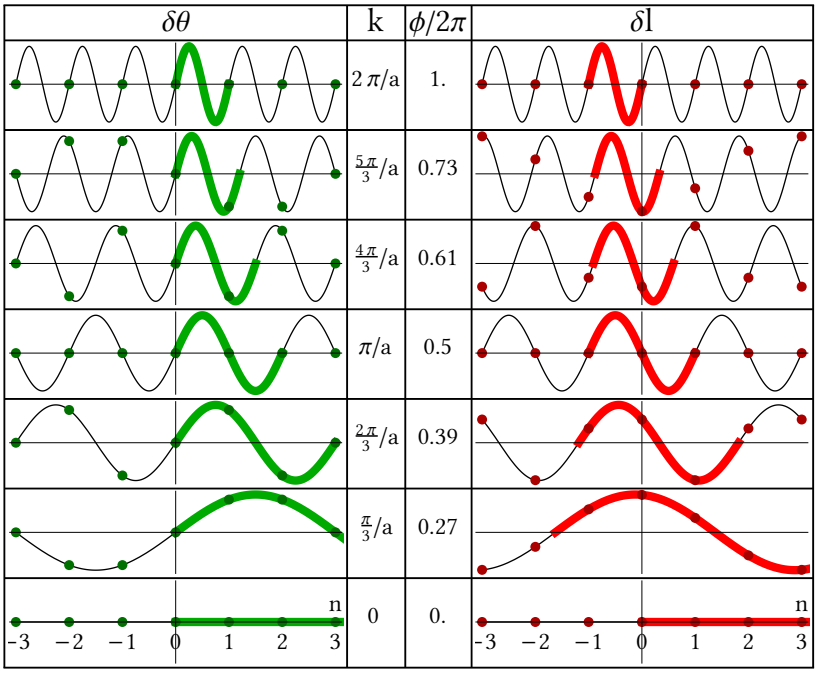

(c) Comparison of phases of $\delta\theta$ and $\delta\ell$ waves in real space with varying k.

Figure 1.6. The same setup as Fig. 1.5 except for a negative $\bar{\theta} = -0.15$, i.e., the rotors are left-leaning. The $\delta\ell$ wave drifts leftward by one period in real space after the wave vector k goes from 0 to $2\pi/a$. Thus the topological index of this chain is one.

1.2 Outline of this thesis

In mechanical metamaterials, large deformations can occur in systems which are topological from the point of view of linear waves. The interplay between such nonlinearities and topology affects wave propagation. Beyond perfectly periodic systems, defects provide a way to modify and control the properties of metamaterials, and can also interact with both nonlinearities and the bulk topology [48, 49].

While the Kane-Lubensky rotor chain (see Sec. 1.1) is an archetypal topological mechanical metamaterial, the kink and antikink solitons in the nonlinear Klein-Gordon equation are archetypal examples of nonlinear behavior [50–52]. In Chapter 2, we study the full nonlinear dynamics of this rotor chain. In the continuum description, we derive a nonlinear field theory which admits topological kinks and antikinks as nonlinear excitations. A topological boundary term, however, breaks the symmetry between the two and favors the kink configuration. Using a cobweb plot, we develop a fixed-point analysis for the kink motion and demonstrate that kinks propagate without the Peierls-Nabarro potential energy barrier typically associated with lattice models. Using continuum elasticity theory, we trace the absence of the Peierls-Nabarro barrier for the kink motion to the topological boundary term which ensures that only the kink configuration, and not the antikink, costs zero potential energy. Further, we study the eigenmodes around the kink and antikink configurations using a tangent stiffness matrix approach appropriate for pre-stressed structures to explicitly show how the usual energy degeneracy between the two no longer holds. In Chapter 3 , we show how the kink-antikink asymmetry also manifests in the way these nonlinear excitations interact with impurities introduced in the chain as disorder in the spring stiffness. Then we discuss the effect of impurities in the spring length and build prototypes based on simple linkages that verify our predictions.

To investigate similar nonlinear behavior in higher spatial dimensions, we first need a detailed understanding at the linear level (where interesting features already occur). Deformed kagome lattices are known to exhibit topological phases [13, 25], and as we shall see, may possess configurations where nonlinear effects cannot be ignored. In Chapter 4, we examine the linear mechanical waves in twisted kagome lattices, which are deformed from

the standard kagome lattice by a zero-energy twisting mechanism. In the perfect lattices, we find that this twisting mechanism tunes the phonon band structure by opening a band gap. At a critical twisting angle, we observe a surprising two-fold degeneracy of the phonon bands, which seems to be related to bonds becoming orthogonal. In Chapter 5, we introduce point defects into the lattices. Defect modes, which are spatially localized and spectrally isolated, appear in the band gap. We show that the hybridization of defect modes can be described by tight-binding models.

When the kagome lattice is untwisted (Fig. 1.1a), there are entire lines of aligned bonds which lead to zero modes at linear level [53]. Similarly, when the kagome lattice is twisted at the critical angle (Fig. 1.1b), neighboring bonds become orthogonal, and the phonon spectrum is two-fold degenerate. In both cases, such properties are related to a decoupling between some degrees of freedom which only occurs at the linear level, and we expect nonlinearities to change the picture. To prepare for a full nonlinear analysis of the kagome lattices, we first focus on a simpler one-dimensional model which should reproduce some of their key features. In Chapter 6, we investigate the propagation of nonlinear transverse elastic waves induced by a point impact of constant velocity in a tension-free flexible string. Transverse waves on a tension-free string have vanishing velocity up to linear order. Waves in the longitudinal and transverse directions are decoupled at linear level but become coupled at the nonlinear level. Even though they become shock waves when the string is under impact, they can be understood from the perspective of linear transverse waves riding on the tensioned region behind longitudinal wave fronts induced by the impact.

Chapter 2

Kink-antikink asymmetry in topological mechanical chains

2.1 Introduction

Topological ideas have led to recent advances in continuum mechanics often inspired by the physics of electronic topological insulators and the quantum Hall effect. In these electronic systems the basic question is whether a material is an insulator or a conductor. The answer depends on which portion of a topological insulator one examines: the bulk is usually gapped and hence insulating while the edge displays gapless edge modes whose existence is protected from disorder and variations in material parameters by the existence of integer-valued topological invariants [54]. In topological mechanical systems, the corresponding question is whether a material is rigid or floppy. The ability to modulate the rigidity of a structure in space allows to robustly localize the propagation of sound waves [17, 29–42, 47, 55, 56], change shape in selected portions [13, 18, 19, 25, 26, 28, 43–46] or focus stress leading to selective buckling or failure [14].

By translating the topological properties of bands of electronic states into the classical setting of vibrational bands, one can identify topologically

protected and hence robust properties of vibrational modes in both discrete lattices and continuous media. For example, the concept of "topological polarization" recently introduced by Kane and Lubensky [25] building on counting ideas from Maxwell and Calladine [57, 58] determines the existence and the position of zero-energy motions that are localized at edges and defects of a marginally rigid mechanical lattice (one in which constraints and degrees of freedom are exactly balanced).

Perhaps the simplest model of topological mechanical lattices is the rotor chain proposed in Ref. [25]. The system consists of a chain of classical rotors harmonically coupled with their nearest neighbours, as shown in Fig. 2.1a. There are two distinct classes of ground state configurations, one with all rotors leaning towards the left and the other where they lean towards the right. Mathematically, these two states may not be deformed to each other without the appearance of bulk zero modes; thus they may each be assigned a different winding number, associated with the Fourier transform of the compatibility matrix $C(q)$, which connects the linear displacement of rotors with the extension of springs; see Ref. [26] for a detailed explanation.

The above considerations arise from band theory and thus concern only the linearized zero-energy infinitesimal motions. Indeed, the vanishing of the linear response implies that nonlinear effects dominate. By developing a nonlinear theory of the rotor chain, it was shown in Ref. [18] that the infinitesimal zero-mode displacement integrates to a finite motion. This motion can be described in the continuum limit by objects similar to "kinks" in the ϕ^4 field theory [50], which connects the topological polarization invariant of the linear vibrations to the study of topological solitons [18, 19]. Although the two appearances of the term "topology" in the linear and nonlinear theory stem from different contexts, the latter encompasses the predictions of the former and also explains additional features exclusive to the nonlinear dynamics [19].

The nonlinear dynamics of this topological chain can be approximated by the critical trajectories of a Lagrangian written in the following form [18, 19]

$$L = \int \mathrm{d}x \quad \underbrace{\left(\frac{\partial u}{\partial t}\right)^2}_{\text{the kinetic term}} - \underbrace{\left(\frac{\partial u}{\partial x}\right)^2 - \frac{1}{2}(u^2-1)^2}_{\text{the classical } \phi^4 \text{ potential terms}} - \underbrace{\sqrt{2}\,\frac{\partial u}{\partial x}(u^2-1)}_{\text{the topological boundary term}} \quad . \tag{2.1}$$

The first term corresponds to the kinetic energy while the second and third are the ones encountered for example in the Landau theory of the Ising model. Note, however, that there is an additional boundary term that contributes to the energy but does not enter the Euler-Lagrange equation. Hence, one obtains static kink and antikink solitary wave solutions of the usual form [50]

$$u = \pm \tanh\left(\frac{x - x_0}{\sqrt{2}}\right). \tag{2.2}$$

The boundary term gives new properties to the solutions and breaks the symmetry between kinks and antikinks. For example, it predicts that the static kink configuration costs zero potential energy while the static antikink configuration has a finite potential energy. Previous work on this model has been motivated by the kink's zero-energy properties, and thus the shape and stability of the antikink and its dynamical behavior were not studied.

In this Chapter we explore the physics of these finite-energy configurations. We compare the dynamics of the kink and antikink sectors in the topological rotor chain and study their interaction with a lattice impurity. We find that differences arising from the topological boundary term are apparent in all of these aspects. In Sec. 2.2, we explain the discrete model and develop a fixed-point analysis of the kink motion using a cobweb plot. In Sec. 2.3, we review the continuum theory and compare the predictions for the antikink with the discrete model. In Sec. 2.4, we study the eigenmodes of the chain around a single kink or antikink profile. We exploit the tangent stiffness matrix approach developed by Guest [59] to analyze prestressed structures. In Sec. 2.5, we study the nonlinear transport properties. In a conventional continuum ϕ^4 field theory, owing to translation invariance, both the kink and antikink propagate at uniform speed. However, lattice discreteness effects breaks this invariance and generates the so-called Peierls-Nabarro (PN) barrier [60–62]. For the topological rotor model, we find that only the antikink has a finite PN barrier whereas the kink always propagates freely. We explain this phenomenon as a consequence of the zero-energy cost associated with the kink profile.

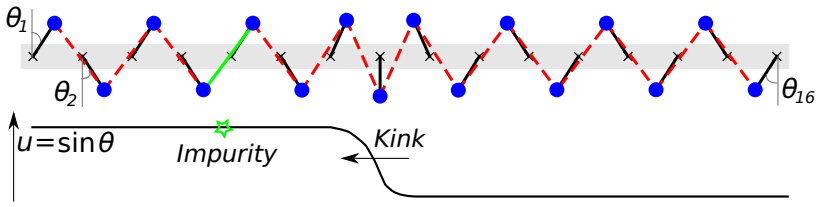

(a)

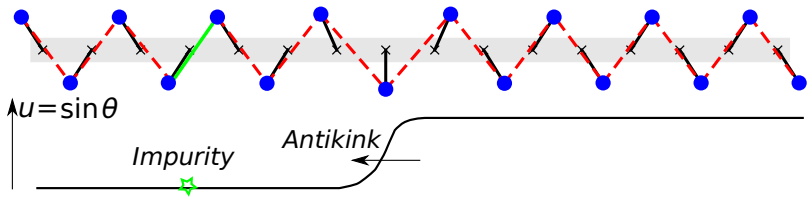

(b)

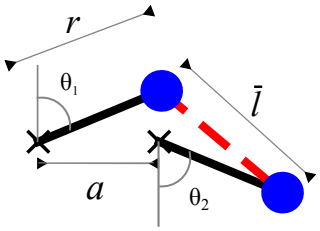

(c)

Figure 2.1. A kink (**a**) and an antikink (**b**) configuration in a topological chain (TC) model of rotors (blue) and springs (red dashed lines) in the presence of a single impurity (green solid lines) modeled as a spring with a different stiffness. For the kink profile, the springs in the chain are at their rest length, while for the antikink, they are stretched. A sketch of kink and antikink profiles in terms of the continuum field variable $u = \sin\theta$ (where θ is the rotor angle) is shown below each configuration. (**c**) A two-rotor system. The masses are the blue dots, the rigid rotors are the black lines, the pivots are the crosses, and the spring is the dashed red line. Here, a is the lattice spacing, r is the rotor length, $\bar{l}$ is the rest length of the springs and $\theta_{1,2}$ are the rotor angles with respect to the vertical.

2.2 Discrete model

The model we study consists of rotors of length r. The rotor pivots are placed on a 1D lattice with spacing a. The angles θ_i of the rotors are measured in an alternating fashion along the lattice, from the positive y-axis at odd-numbered sites and negative y-axis at even-numbered sites. The equilibrium angle is $\overline{\theta}$ for a uniform lattice configuration *without* a kink or antikink. The masses M at the tips of the rotors are connected by harmonic springs with identical rest lengths $\bar{l}$ and spring constants k. The two-rotor unit cell of the topological chain is illustrated in Fig. 2.1c.

We now construct the chain *with* a kink under free boundary conditions. There are n rotors and $n-1$ springs. If we assume that the springs are infinitely stiff ($k \to \infty$), the springs become $n-1$ constraints and the system only has a single independent degree of freedom. The angle of a single rotor determines all the others iteratively. This degree of freedom manifests itself as a mechanism which, as has been previously shown in [18], can be approximately described by the domain wall solution in a modified ϕ^4 theory [1]. We call this mechanism a "kink" and discuss its continuum theory in the following sections.

We use a cobweb plot to display the kink in Fig. 2.2. This is a tool for visualizing the process of iteratively solving the nonlinear constraint equations Eqn. (2.3) cell by cell. We construct the cobweb plot by drawing (1) a diagonal line $\theta_i = \theta_{i+1}$ and (2) a curve of the implicit function given by the nonlinear constraint equation that ensures the springs are not stretched,

$$(a + r\sin\theta_i - r\sin\theta_{i+1})^2 + (r\cos\theta_i + r\cos\theta_{i+1})^2 = \bar{l}^2. \qquad (2.3)$$

(An explicit relation between neighbouring rotor angles is derived analytically with complex notation in Appendix 2.A.)

[1] Varying the parameters $(a, r, \overline{\theta})$ yield other phases of the topological rotor chain. In this thesis, we only consider the topological chain in the *flipper* phase [18] where the ϕ^4 theory is a valid approximation. The name flipper describes the back-and-forth motion of the rotors as a kink propagates, in contrast to the *spinner* phase, where the rotors complete a full circle. The continuum limit of the spinner phase can be approximately described by the sine-Gordon theory

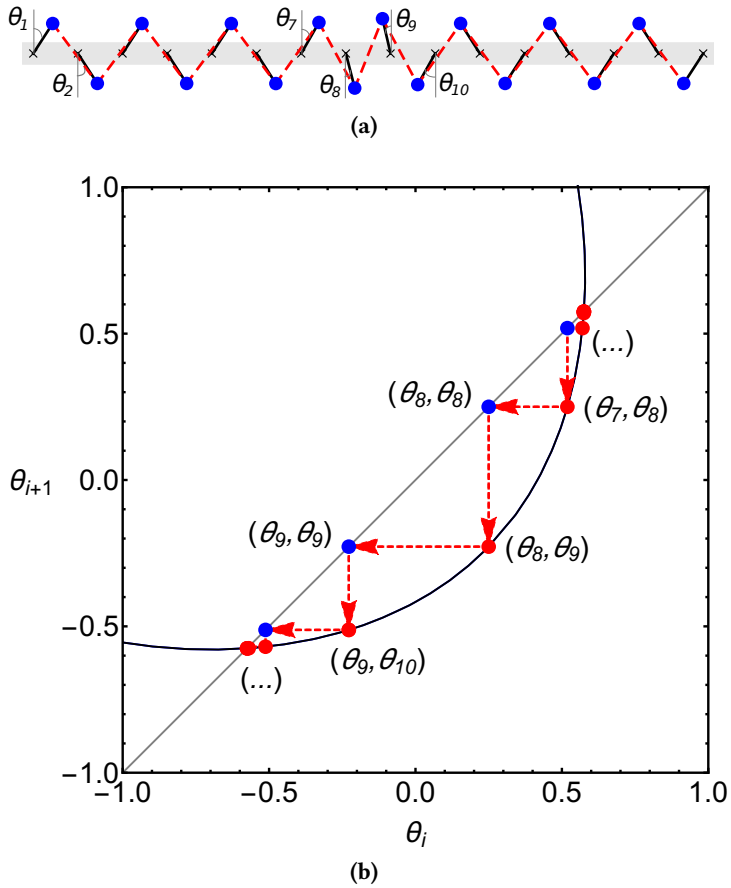

Figure 2.2. The configuration (**a**) and the corresponding cobweb plot (**b**) for the kink in a topological rotor chain with $r/a = 0.8$, $|\bar{\theta}| = 0.58$. The springs are at their rest lengths. In (**b**), the black curve is the constraint equation which ensures that the springs are unstretched, the gray diagonal line satisfies $\theta_{i+1} = \theta_i$, the blue point (θ_i, θ_i) represents rotor i, the red point (θ_i, θ_{i+1}) represents the spring connecting rotors i and $i+1$, and the red dashed lines with arrows indicates the iterative process that generates the kink profile. The iteration steps from θ_7 to θ_{10} are shown.

The iteration steps are as follows:

1. Given the angle θ_1 of the first rotor at the left end, find the point on the

function curve with coordinates (θ_1, θ_2).

2. Draw a horizontal line from (θ_1, θ_2) to the diagonal line. This gives the point (θ_2, θ_2).

3. Draw a vertical line from (θ_2, θ_2) to the function curve. This gives the point (θ_2, θ_3).

4. Repeat step 2 and 3 until the point (θ_{n-1}, θ_n) is found.

In Fig. 2.2b, we illustrate steps 2 and 3 from θ_7 to θ_{10}, which are near the kink center. The blue point with coordinates (θ_i, θ_i) stands for the ith rotor of angle θ_i. The red point with coordinates (θ_i, θ_{i+1}) represents the state of the spring that connects the rotors of θ_i and θ_{i+1}.

Note that in Fig. 2.2b, the diagonal line and the function curve intersect at two points. They are the fixed points of iteration. If all the red points (θ_i, θ_{i+1}) stay at one fixed point, the plot represents a uniform lattice. The iteration step proceeds from the leftmost rotor of the chain to the rightmost. We see that the flow proceeds outwards from one fixed point and then inwards towards the other fixed point.

The cobweb plot may be used to graphically derive the decay lengths of zero energy deformations, as they approach their uniform limits. As mentioned above, a fixed point corresponds to an intersection between the line $\theta_i = \theta_{i+1}$ and the function curve. Note that the behavior of θ_i as it approaches a fixed point resembles a "self-similar" zigzag motion between $\theta_i = \theta_{i+1}$ and the tangent line of the function curve. This motivates linearizing the function curve around the fixed point as follows:

$$\theta_{i+1} - \overline{\theta} = F'(\overline{\theta})(\theta_i - \overline{\theta}), \tag{2.4}$$

where $\overline{\theta}$, the equilibrium angle, is also just the value of the fixed-point angle and $F'(\overline{\theta})$ is the slope of the function curve at that point (which could be computed explicitly in terms of $r, a, \bar{l}$). This equation yields that $\theta_i - \overline{\theta} \propto \exp(\log F'(\overline{\theta})i)$, or that the decay length is $|1/\log F'(\overline{\theta})|$ (the sign of $\log F'$ tells us whether the fixed point is attracting or repelling). This result recovers the penetration depth of the boundary modes computed in Ref. [18] using band theory.

In the cobweb plot, the static kink appears as a sequence of points on the function curve interpolating between a repelling and attracting fixed point. The dynamics of the kink in the cobweb plot is therefore the flow of a cascade of points between a pair of fixed points (Movie S1). While the kink propagates, the points in the middle, such as (θ_7, θ_8), (θ_8, θ_9) and (θ_9, θ_{10}), corresponding to the kink center, move more than those points close to the fixed points, corresponding to the spatially localized nature of the kinetic energy.

Generating an antikink requires a few more steps, as it stretches springs, and thus does not satisfy a constraint function that we could iteratively solve. However, the continuum theory suggests that kinks and antikinks both have the same functional profiles with only their signs reversed (see Sec. 2.3). As a result, we use the same iterative procedure as that for the kink, and then simply swap the appearances of θ_i and θ_{i+1} in Eqn. (2.3) to obtain an approximation for the antikink profile. This method is equivalent to reflecting the red points in Fig. 2.2b across the diagonal line. The antikink constructed this way is not an equilibrium configuration and has unbalanced stresses in the springs. This is because generically, the profiles of the kink and antikink are not the same in a discrete topological rotor chain. We next relax the springs using *dissipative* Newtonian dynamics to remove the unbalanced stresses and obtain a stable profile, which we show in the cobweb plot in Fig. 2.3. In that figure, the spring connections (red dots) around the core of the antikink profile (rotors 8 and 9) do not fall on the curve which corresponds to unstretched springs. This implies large spring deformations which we show explicitly in Fig. 2.4b. The amount by which the springs are stretched is symmetrical around the 8th spring, which is in accordance with the fact that a stable antikink has balanced forces on each rotor. Note that we have fixed the boundary conditions to ensure that the antikink is in mechanical equilibrium, which is not generically true. As discussed later in Sec. 2.5, this has important consequences for the PN barrier.

2.3 Continuum theory

In this section, we review the continuum approximation to the kink and antikink profiles [18] and compare these with the discrete model developed in the previous section. The discrete Lagrangian for the topological rotor chain

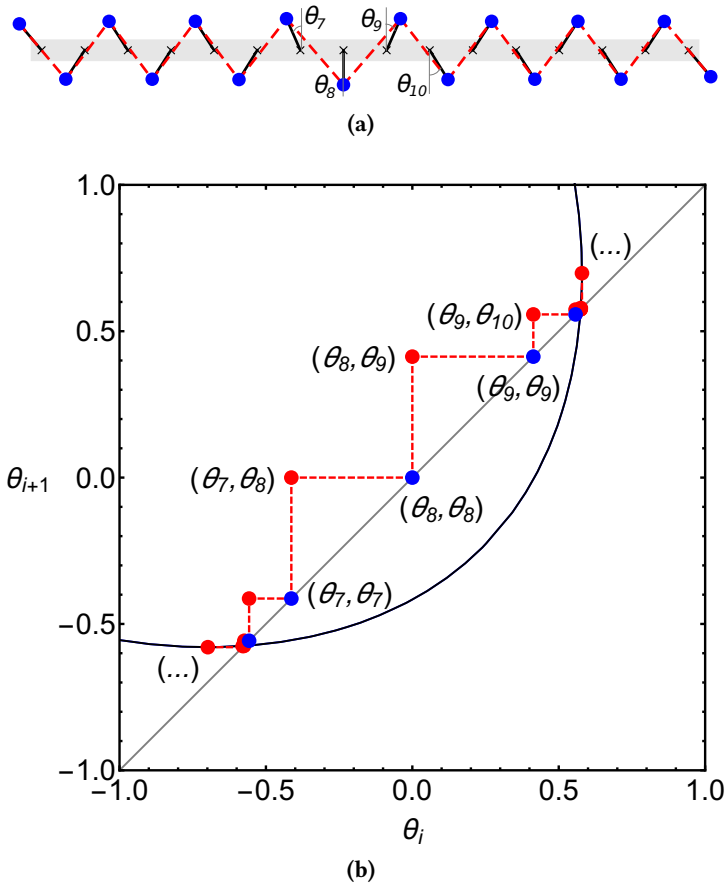

Figure 2.3. The configuration (**a**) and the corresponding cobweb plot (**b**) for an antikink profile in the topological rotor chain with $r/a = 0.8$, $|\overline{\theta}| = 0.58$, where we see that the springs are stretched. In (**b**) the same graphic notation as in Fig. 2.2 is used except that we have not used an iterative process for constructing the antikink profile, rather, depicted is only a visualization of the configuration of the rotor chain. The red points are obtained by first reflecting the red points in Fig. 2.2b across the diagonal line, and then relaxing the springs using dissipative Newtonian dynamics. Note that the two rotors at the edges need to be collinear with the springs to ensure force balance. This results in the angles overshooting at the fixed points.

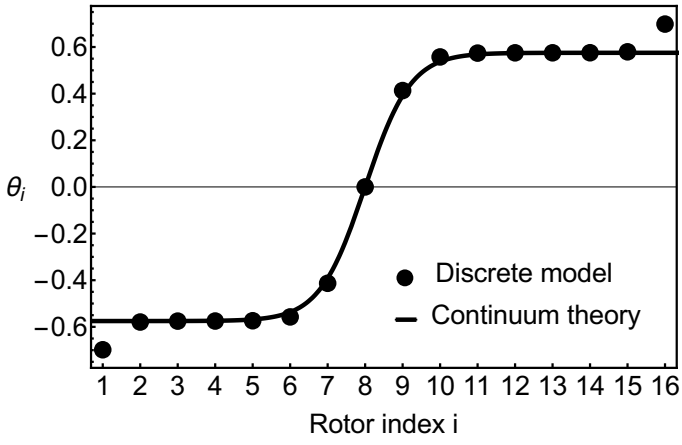

(a)

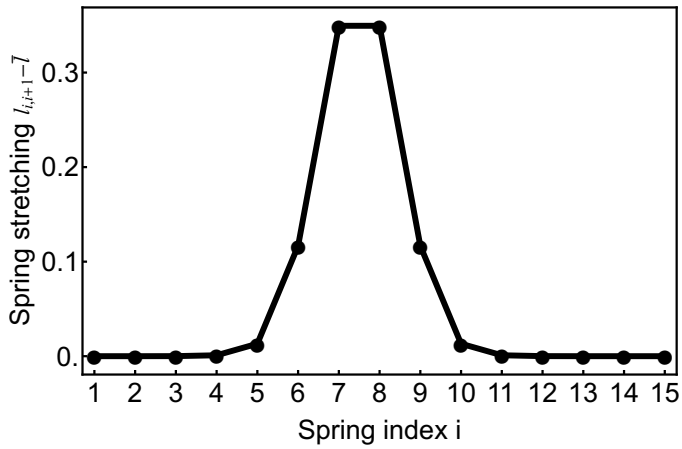

(b)

Figure 2.4. (**a**) The θ profile (rotor angles) for the antikink profile in Fig. 2.3a and the corresponding continuum prediction from Eqn. (2.13). Note that the two rotors at the edges need to be collinear with the springs to ensure force balance and this results in the rotor angles overshooting the equilibrium value $\overline{\theta} = \pm 0.58$. (**b**) The amount of spring stretching for the antikink profile.

(see also Fig. 2.2a) with free boundary conditions is

$$L = \sum_{i=1}^{n} \frac{1}{2} M r^2 \left(\frac{\mathrm{d}\theta_i}{\mathrm{d}t} \right)^2 - \sum_{i=1}^{n-1} \frac{1}{2} k (l_{i,i+1} - \bar{l})^2. \tag{2.5}$$

Here, n is the total number of rotors, M is the mass at the tip of a rotor, r is the rotor length, θ_i is the angle that rotor i makes with the vertical (measured alternately as shown in Fig. 2.2a), k is the spring constant, $\bar{l}$ is the rest length of the spring and $l_{i,i+1}$ is the instantaneous length of the spring that connects rotor i to rotor $i+1$. From geometry

$$l_{i,i+1}^2 = a^2 + 2ar(\sin\theta_{i+1} - \sin\theta_i) + 2r^2 + 2r^2\cos(\theta_i + \theta_{i+1}). \tag{2.6}$$

which in the uniform limit $\theta_i = \theta_{i+1} = \bar{\theta}$ gives the rest length of the spring $\bar{l}^2 = a^2 + 4r^2\cos^2\bar{\theta}$.

We make the working assumption that deformations do not stretch the springs significantly and hence we can neglect (or add) terms higher than quadratic order in $l_{i,i+1} - \bar{l}$ for all i. This is a reasonable approximation for the system configuration with a kink profile but is not well-justified for an antikink profile. However, in the limit that $\bar{\theta} \ll 1$, we find this to be a good approximation for both kinks and antikinks. Within this limit, we therefore express the potential energy term in Eqn. (2.5) as

$$\frac{1}{2} k (l_{i,i+1} - \bar{l})^2 \approx \frac{k}{8\bar{l}^2} \left(l_{i,i+1}^2 - \bar{l}^2 \right)^2. \tag{2.7}$$

Substituting the expression for $\bar{l}$ and Eqn. (2.6) into Eqn. (2.7), we express the potential energy as

$$V_{i,i+1} = \frac{kr^4}{2\bar{l}^2} \left(\frac{a}{r}(\sin\theta_{i+1} - \sin\theta_i) - \cos 2\bar{\theta} + \cos(\theta_i + \theta_{i+1}) \right)^2. \tag{2.8}$$

Now we take the continuum limit of the potential. First we define a continuum field for the rotor angles $\theta(x)$, where the spatial variable $x = ia + \frac{a}{2}$ is located symmetrically between two rotors in the unit cell. To leading order,

$\theta_i \to \theta(x) - (a/2)(\mathrm{d}\theta/\mathrm{d}x)$ and $\theta_{i+1} \to \theta(x) + (a/2)(\mathrm{d}\theta/\mathrm{d}x)$. Eqn. (2.8) can then be expressed as

$$aV[\theta] = \frac{2k}{\bar{l}^2}\left(\frac{a^2}{2}\frac{\mathrm{d}u}{\mathrm{d}x} + \overline{u}^2 - u^2\right)^2, \tag{2.9}$$

where we have defined the projection of the rotor position on the $x-$axis as a new field variable $u(x) \equiv r\sin\theta(x)$ and $\overline{u} \equiv r\sin\overline{\theta}$.

The kinetic energy density term in Eqn. (2.5) then assumes the form

$$aT[\dot{\theta}] = \frac{1}{2}\frac{Mr^2}{r^2 - u^2}\left(\frac{\mathrm{d}u}{\mathrm{d}t}\right)^2. \tag{2.10}$$

Next we approximate the Lagrangian Eqn. (2.5) as

$$\begin{aligned} L \approx \int \mathrm{d}x \Bigg\{ & \frac{M}{2a}\left(\frac{\partial u}{\partial t}\right)^2 - \frac{ka^3}{2\bar{l}^2}\left(\frac{\partial u}{\partial x}\right)^2 \\ & - \frac{2k}{a\bar{l}^2}(\overline{u}^2 - u^2)^2 - \frac{ka}{\bar{l}^2}\frac{\partial u}{\partial x}(\overline{u}^2 - u^2)\Bigg\}. \end{aligned} \tag{2.11}$$

where we have taken the leading order of the Taylor series expansion of the nonlinear kinetic term (in the variable u^2/r^2), which is valid in the limit when $u \ll r$ or equivalently $\sin\theta \ll 1$.

The first three terms in Eqn. (2.11) constitute the normal ϕ^4 theory. The last term linear in $\partial u/\partial x$, is an additional topological boundary term. Being a total derivative, it does not enter the Euler-Lagrange equation of motion and we obtain the usual nonlinear Klein-Gordon equation

$$\frac{M}{a}\frac{\partial^2 u}{\partial t^2} - \frac{ka^3}{\bar{l}^2}\frac{\partial^2 u}{\partial x^2} - \frac{8k}{a\bar{l}^2}\overline{u}^2 u + \frac{8k}{a\bar{l}^2}u^3 = 0, \tag{2.12}$$

whose kink and antikink solutions are given by

$$u_0 = \pm\overline{u}\tanh\left[\frac{x - x_0 - vt}{(a^2/2\overline{u})\sqrt{1 - v^2/c^2}}\right], \tag{2.13}$$

where the $\pm$ denotes an (+)antikink and (-)kink respectively. Here, v is the (anti)kink speed of propagation and $c = (a^2/\bar{l}\sqrt{k/M})$ is the speed of sound in the medium. See Fig. 2.4a for a comparison with the discrete profile.

Note how the additional boundary term makes the potential energy density $V[\theta]$ a perfect square, see Eqn. (2.9). For the kink configuration, $V[\theta]$ therefore vanishes as is the case in the discrete topological chain. For the antikink however, $V[\theta]$ is nonzero and is in fact twice of what we would expect in the normal ϕ^4 theory (where both the kink and antikink configurations have the same energy). This is an agreement with our discussion on the discrete model in Sec. 2.2.

Upon substituting the static ($v = 0$) antikink profile from Eqn. (2.13) into Eqn. (2.11) and completing the integral, we obtain the potential energy of the topological rotor chain with an antikink profile

$$V_{antikink}/(ka^2) = \frac{16}{3}\frac{(r/a)^3 \sin^3\overline{\theta}}{1 + 4(r/a)^2\cos^2\overline{\theta}}. \tag{2.14}$$

In Fig. 2.5, we compare this expression with the predictions from the discrete model. We see that the continuum theory agrees reasonably well with the discrete model as long as $\overline{\theta}$ is less than approximately 0.6, below which, the width of the antikink is larger than the lattice spacing and therefore, a continuum approximation well justified.

2.4 Linear modes

We now study small oscillations around the kink and antikink configurations, first in the continuum limit, and next in the discrete model by developing the tangent stiffness matrix approach. In the continuum limit, we make the ansatz $u = u_0 + \delta u$ and substitute into Eqn. (2.12) retaining only terms linear in δu:

$$\frac{M}{a}\frac{\partial^2 \delta u}{\partial t^2} - \frac{ka^3}{\bar{l}^2}\frac{\partial^2 \delta u}{\partial x^2} - \frac{8k}{a\bar{l}^2}(\overline{u}^2 - 3u_0^2)\delta u = 0 \tag{2.15}$$

If we Fourier transform Eqn. (2.15) with respect to time, we obtain a Schödinger-like equation with a solvable potential [63, 64]. This yields one continuous spectral band as well as two discrete modes – one translation mode for the

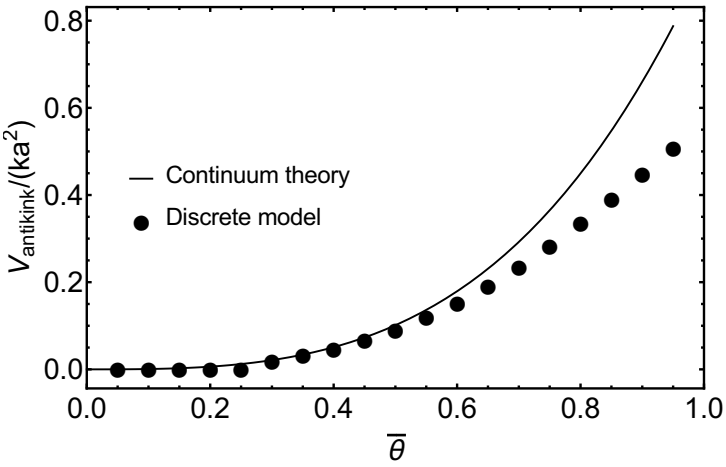

Figure 2.5. The normalized potential energy plotted against the equilibrium angle $\overline{\theta}$, for a static antikink configuration in a topological rotor chain with with $r/a = 0.8$. The discrete model has 60 rotors. Note that the wobbler transition [18] is around $\overline{\theta} = \sin^{-1}\left(\frac{a}{2r}\right) = 0.67$, which is close to where the continuum theory starts to significantly deviate from the discrete model.

(anti)kink and one shape mode [65], which corresponds to small deformations of the shape of the (anti)kink localized around the center of their profile. For the topological rotor chain, the frequencies of the two discrete modes are:

$$\omega_t = 0, \quad \text{for the translation mode} \tag{2.16}$$

$$\omega_s = (r/a)\sqrt{12k/M}\,\sin\overline{\theta}/\sqrt{1+4(r/a)^2\cos^2\overline{\theta}}, \quad \text{for the shape mode.} \tag{2.17}$$

In Fig. 2.6a and 2.6c, the kink and antikink are located in the middle of the chain. The mode arrows (in green) that all point in the same direction, correspond to a translation mode. In Fig. 2.6b and 2.6d, the arrows on either side of the (anti)kink, point in opposite directions and these correspond to shape deformations of the (anti)kink.

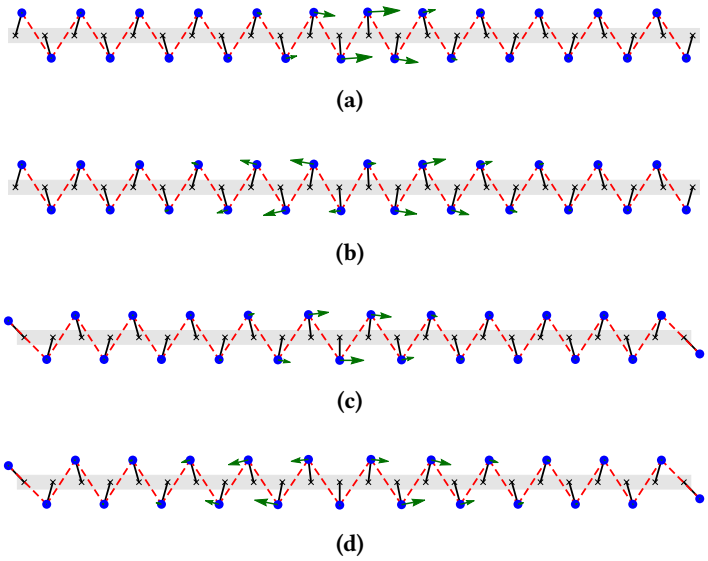

Figure 2.6. The configurations of (**a**) the kink translation mode, (**b**) the kink shape mode, (**c**) the antikink translation mode and (**d**) the antikink shape mode. The green arrows depict the mode component of each rotor.

In Appendix 2.B, we follow the approach proposed by Guest [59] to derive the *tangent stiffness matrix* $\mathbf{K}$ for prestressed mechanical structures. With $\mathbf{K}$ we numerically obtain the frequencies of localized modes for the discrete chain model and compare them with the predictions of the continuum theory (Eqn. (2.16) and Eqn. (2.17)) in Fig. 2.7. We find that the translation mode ω_t for the kink indeed vanishes (within machine-precision in our numerics) for all values of $\overline{\theta}$ and is thus absent in the range of the log-log plot shown in Fig. 2.7a). However, as seen in Fig. 2.7b, the translation mode (open circles) for the antikink is nonzero.

For the shape mode ω_s (filled circles), we find the numerical results for both the kink and antikink to be in good agreement with the continuum theory at small $\overline{\theta}$. Note that in Fig. 2.7b, although the antikink has a finite nonzero ω_t, the value is still significantly smaller than ω_s.

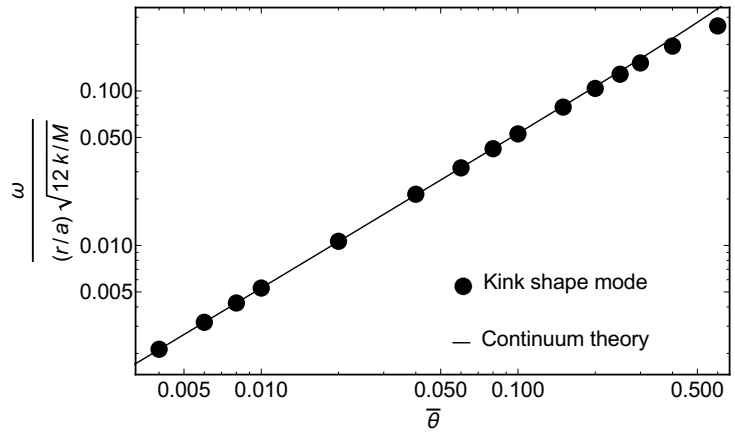

(a)

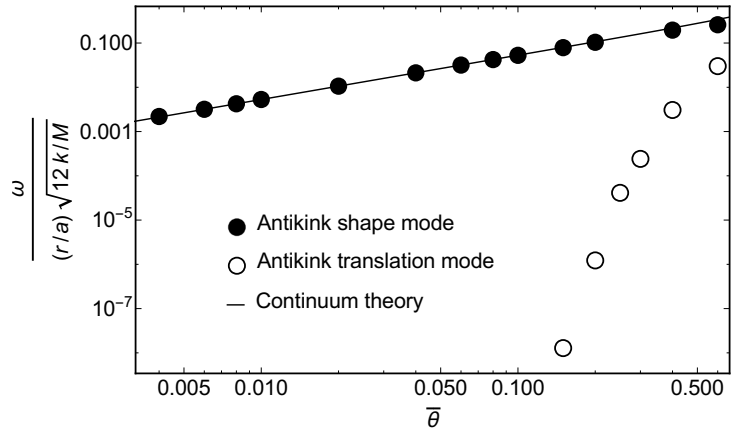

(b)

Figure 2.7. The frequencies ω of localized mode(s) for (**a**) the kink and (**b**) the antikink as a function of $\overline{\theta}$ for a rotor chain with $r/a = 0.8$. The data points are numerically obtained from the tangent stiffness matrix approach, filled circles correspond to the shape mode (ω_s), while open circles correspond to the translation mode (ω_t) . The curves are from the continuum theory. The frequencies for the kink translation mode for all $\bar{\theta}$ and the frequencies for the antikink translation mode for $\overline{\theta} < 0.1$ are effectively zero at machine precision and thus, not visible in the figure.

2.5 Nonlinear dynamics

In the previous section, we have seen that for the discrete topological chain, the energy of the translation mode for the kink is zero, whereas that for the antikink is non-zero. Note that the standard discretization of a ϕ^4 field theory leads to a non-zero translation mode for both the kink and antikink [62]. Thus, the kink here differs qualitatively from the antikink in that it has a zero mode even when we consider the discrete model. We next numerically simulate the propagation of a kink and antikink along the discrete chain and see how this difference manifests in their dynamics.

We numerically integrate Newtons equation of motion for the rotors using molecular dynamics simulations. (The simulation settings are described in Appendix 2.C.) A stable chain configuration with a single kink or antikink is used as the initial configuration (see Figs. 2.6a- 2.6c for the initial conditions used). An excitation is set in motion with a velocity along the direction of the translation mode, but with variable amplitudes.

In Fig. 2.8, we plot the kinetic energy (K.E.) of the chain as a function of time for a set of parameters, for a kink excitation (solid curve) and an antikink excitation (dashed curve). The K.E. of the kink remains nearly constant for all times with some small fluctuations (as the springs have to slightly deform to transport energy by simultaneously minimize the potential and kinetic energy). However in comparison, the K.E. of the antikink for the same set of initial parameters changes significantly as it propagates down the chain. The key point is that the kink and antikink do not propagate in the same way.

The asymmetry between a *static* kink and antikink configuration was discussed in [18]. Further, we also know from Eqn. (2.11) (and the ensuing discussion) that in the continuum limit, the topological rotor chain is approximately described by a ϕ^4 theory with an additional topological boundary term which ensures that the potential energy of the kink is zero while that for the antikink is nonzero (see Ref. [19] for an interpretation of this fact in terms of supersymmetry breaking). However, the additional boundary term does not affect the continuum equation of motion and thus, both the kink and antikink should have translational invariance in this limit and their dynamics should not have differed.

The reason for this asymmetrical behavior can be understood only if we

examine the discrete model. The system with free boundary conditions has n rotors and $n-1$ springs, and the static kink does not require any of the springs to be stretched. We can therefore interpret the springs as constraints. Thus, the discrete kink's equilibrium manifold is a continuous curve embedded in the n-dimensional configuration space of the rotor angles θ_i and the kink can be positioned stably anywhere along the chain. By contrast, an antikink requires the springs to be stretched. Forces on each of the rotors have to be balanced for the system to be in mechanical equilibrium. So the possible equilibrium configurations have to be symmetrical locally around the center of the antikink, as shown in Fig. 2.9. As a result, the equilibrium manifold for an antikink is not a continuous curve but rather, consists of a set of discrete points. These correspond to either saddle points or minima in the potential landscape. Any locally asymmetrical configuration is therefore not stable and will slide towards a minima.

The saddle points and their nearest minima can be connected by an "adiabatic trajectory" [61], which is a curve of steepest descent. The concept of an adiabatic trajectory is useful in two ways. First, it describes the slow motion of the antikink through the chain. The position of the antikink center can be defined by a coordinate along such a trajectory. Secondly, it helps to rigorously define the so-called Peierls-Nabarro (PN) potential [60–62], which is the effective periodic potential that the antikink feels as it moves along the adiabatic trajectory. A saddle point in the full potential energy landscape corresponds to a maximum along the adiabatic trajectory (while a minimum is still a minimum). Note that although the antikink's K.E. fluctuations in Fig. 2.8 do not strictly equal its PN potential barrier, the former reveals the existence of the latter.

In Appendix 2.D, we derive the PN potential barrier from the continuum theory

$$\begin{aligned} V_{PNB} &= \frac{4\pi^2\Big(\pi^2 + (a/w)^2\Big)}{3\Big(1 + 4(r/a)^2 - (a/w)^2\Big)\sinh(\pi^2 w/a)} \\ &\propto e^{-\pi^2 w/a} \qquad \text{for large } w/a. \end{aligned} \tag{2.18}$$

This shows that the PN barrier decays exponentially as the width w of the antikink increases.

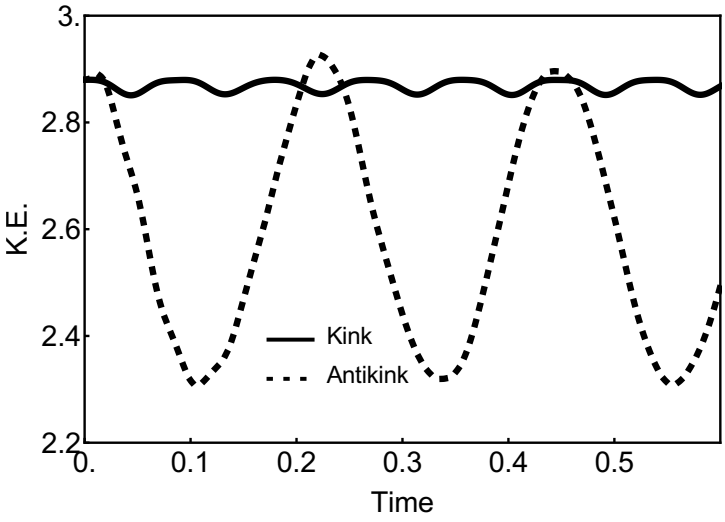

Figure 2.8. Time evolution of the kinetic energy for a kink (Fig. 2.6a) and an antikink (Fig. 2.6c) in a topological rotor chain with non-dimensional parameters $M = 1$, $k = 10000$, $r/a = 0.8$, $\overline{\theta} = 0.58$. The magnitude of initial velocity in both cases is $v_0 = 2.4$. The units of energy and velocity are determined by the aforementioned physical parameters. The kink propagation only results in small oscillation of the K.E. whereas we see significant fluctuations during the propagation of an antikink. These can be traced to the Peierls-Nabarro potential as shown in Fig. 2.9

We next compare the theoretical results with numerical simulations. We obtain the exact PN barrier by computing the difference in potential energy between the two types of equilibrium points: a minima and a saddle point, see Fig. 2.9, where for a given set of parameters, we find the barrier height to be $1359.75 - 1359.15 = 0.60$, consistent with the magnitude of the K.E. fluctuations shown in Fig. 2.8 for the same set of parameters. By repeating this calculation for systems with various antikink widths w, we obtain the dependence of the normalized PN barrier $V_{PNB}/(ka^2)$ on w/a, which we show in Fig. 2.10. We compare these with the predictions from the continuum theory, given by Eqn. (2.18). The numerical results (filled circles) obtained from the discrete lattice and the theoretical predictions (continuous curve) follow a similar trend, but differ by at least one order of magnitude. This can be explained

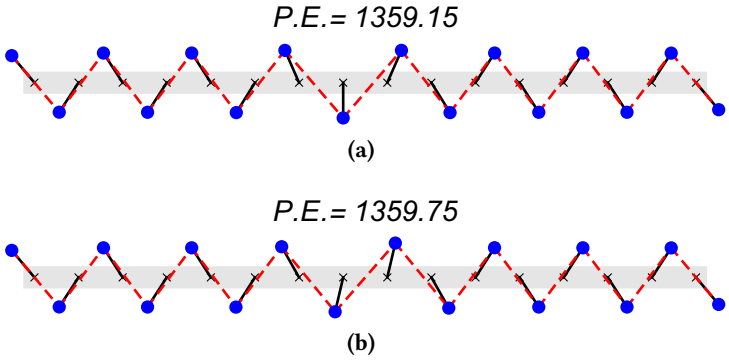

Figure 2.9. Two equilibrium configurations in the potential energy landscape of a static antikink: (**a**) a minimum and (**b**) a saddle point, respectively. The topological chain has the same configuration parameters as in Fig. 2.8.

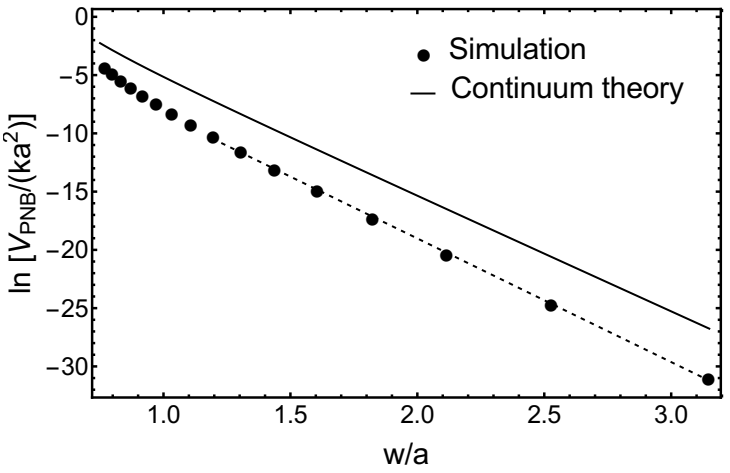

Figure 2.10. The dependence of the normalized PN barrier (V_{PNB}/ka^2) on the normalized antikink width (w/a), for both the discrete model (black circles) and the continuum theory (solid line). The slope of the dashed line (fit to simulation) is -10.6, in reasonable agreement with the predictions from the continuum theory in Eqn. (2.18), which gives a slope $-\pi^2 \approx -9.9$.

by the fact that the discreteness of the lattice is ignored in the theory when we take the continuum limit in going from Eqn. (2.8) to Eqn. (2.9). See [60] for a thorough discussion of the effect of lattice discreteness on the single-kink dynamics in a ϕ^4 model.

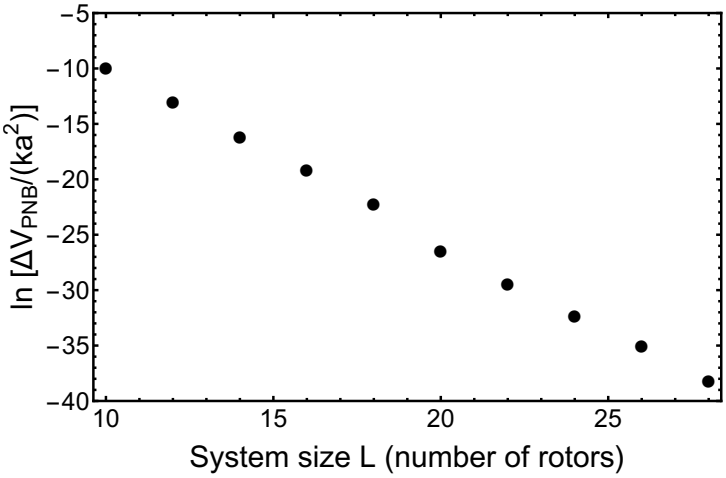

Figure 2.11. The finite-size effect on V_{PNB}. ΔV_{PNB} is defined as $V_{PNB}(L) - V_{PNB}(L = 60)$. The configuration parameters are $r/a = 0.8$ and $\overline{\theta} = 0.40$.

Further, we also investigate finite-size corrections to the PN barrier, or more precisely, the difference between V_{PNB} for a system with a small finite size and that for a system with a sufficiently larger size (60 rotors). We find that finite size effects decay quickly as an exponential function with increasing system size for a topological rotor chain with a central antikink (see Fig. 2.11). This is because an antikink configuration is a localized object. The components of its displacement, its translation mode, as well as its shape mode, decay exponentially away from its center and therefore, so does the effect of any boundaries.

To summarize, for the topological rotor chain that we study, the PN barrier for a kink vanishes and that for an antikink is finite. This, not only affects how their respective kinetic energies fluctuate over a lattice spacing, but also affects their dynamics over long distances. It is well known that ϕ^4 kinks and antikinks are non-integrable solutions [64]. Although the kinks and antikinks

are "topologically" robust objects, they still tend to dissipate energy into phonons and into shape fluctuations as they propagate. Once an antikink has lost too much kinetic energy to be able to overcome the PN barrier, it gets trapped in a PN potential minimum, as shown in Fig. 2.12. On the other hand, for the topological rotor chain that we study, the kink never gets trapped, since its PN barrier vanishes.

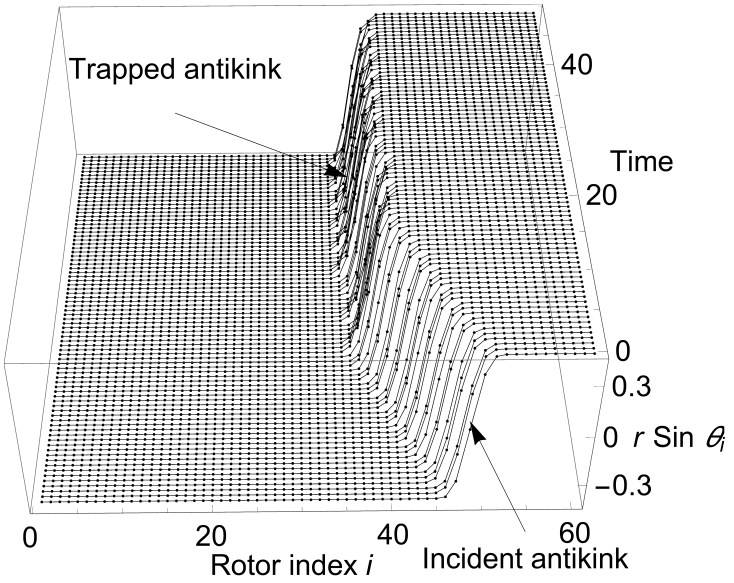

Figure 2.12. Perspective view of a moving antikink trapped in its Peierls-Nabarro barrier around Time $= 20$ near Rotor #35. The topological rotor chain has the same configuration parameters as in Fig. 2.8 and the initial antikink velocity is $v_0 = 1.1$ in non-dimensional units.

Appendix

2.A Complex notation

We use complex variables to derive the explicit relation between neighbouring rotor angles. Adopting the notation in Fig. 2.1c, we put the pivot of rotor 1 at the origin of complex plane and the pivot of rotor 2 at the coordinate (a,0). The positions of the rotor tips are

$$z_1 = ire^{-i\theta_1}, \tag{2.19}$$

$$z_2 = a - ire^{i\theta_2}. \tag{2.20}$$

We have two constraints (where a bar represents complex conjugations):

$$(z_2 - z_1)(\bar{z}_2 - \bar{z}_1) = l_0^2, \tag{2.21}$$

$$(z_2 - a)(\bar{z}_2 - a) = r^2. \tag{2.22}$$

Eliminating $\bar{z}_2$ from above two constraints, we find a quadratic equation for z_2,

$$Az_2^2 + Bz_2 + C = 0, \tag{2.23}$$

where

$$A = \frac{\bar{z}_1 - a}{a - z_1}, \tag{2.24}$$

$$B = \left(\frac{l_0^2 + a^2 - 2r^2}{a - z_1}\right) - a\left(\frac{\bar{z}_1 - z_1}{a - z_1}\right), \tag{2.25}$$

$$C = a^2 - r^2 - a\left(\frac{l_0^2 + a^2 - 2r^2}{a - z_1}\right). \tag{2.26}$$

We have two branches of the solution for z_2

$$z_2 = \frac{-B \pm \sqrt{B^2 - 4AC}}{2A}, \tag{2.27}$$

which explicitly expresses the black curve in Fig. 2.2b.

2.B Vibrational modes of prestressed mechanical structures

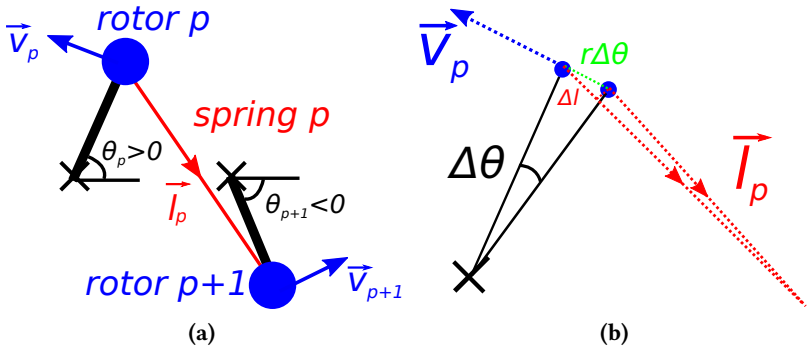

Figure 2.13. Detailed configurations around a single spring p.

We demonstrate how to use to the method of tangent stiffness matrix to calculate normal modes in prestressed mechanical structures [59].

Consider a single spring p in the configuration shown in Fig. 2.13a (note here, we are now specifying rotor angles θ with respect to the positive x-axis). From geometry, we find

$$\begin{aligned} f_p &= -\vec{v}_p \cdot \vec{l}_p \;\; \hat{t}_p \\ f_{p+1} &= \vec{v}_{p+1} \cdot \vec{l}_p \;\; \hat{t}_p. \end{aligned} \tag{2.28}$$

Here, f_p is the spring force projected along the tangent vector $\vec{v}_p$ of rotor p

$$\vec{v}_p = \begin{pmatrix} -\sin\theta_p \\ \cos\theta_p \end{pmatrix}. \tag{2.29}$$

$\vec{l}_p$ is the vector along the length of the spring p and points from rotor p to $p+1$,

$$\vec{l}_p = \begin{pmatrix} a + r\cos\theta_{p+1} - r\cos\theta_p \\ r\sin\theta_{p+1} - r\sin\theta_p \end{pmatrix}. \tag{2.30}$$

$\hat{t}_p$ is a scalar *tension coefficient* for spring p, defined as $\hat{t}_p \equiv t_p/|\vec{l}_p|$, where $t_p \equiv k_p(|\vec{l}_p| - \bar{l})$ for a harmonic spring. Here, $|\vec{l}_p|$ is the instantaneous length of spring p, $\bar{l}$ is the rest length of the spring, and k is the spring constant.

In order to find the tangent stiffness, we differentiate Eqn. (2.28) with respect to the rotor angles θ_p and θ_{p+1}

$$\frac{\partial f_p}{r\partial\theta_p} = \frac{\partial(-\vec{v}_p \cdot \vec{l}_p)}{r\partial\theta_p}\ \hat{t}_p - \vec{v}_p \cdot \vec{l}_p\ \frac{\partial \hat{t}_p}{r\partial\theta_p} \tag{2.31}$$

$$\frac{\partial f_p}{r\partial\theta_{p+1}} = \frac{\partial(-\vec{v}_p \cdot \vec{l}_p)p}{r\partial\theta_{p+1}}\ \hat{t}_p - \vec{v}_p \cdot \vec{l}_p\ \frac{\partial \hat{t}_p}{r\partial\theta_{p+1}} \tag{2.32}$$

$$\frac{\partial f_{p+1}}{r\partial\theta_p} = \frac{\partial(\vec{v}_{p+1} \cdot \vec{l}_p)}{r\partial\theta_p}\ \hat{t}_p + \vec{v}_{p+1} \cdot \vec{l}_p\ \frac{\partial \hat{t}_p}{r\partial\theta_p} \tag{2.33}$$

$$\frac{\partial f_{p+1}}{r\partial\theta_{p+1}} = \frac{\partial(\vec{v}_{p+1} \cdot \vec{l}_p)}{r\partial\theta_{p+1}}\ \hat{t}_p + \vec{v}_{p+1} \cdot \vec{l}_p\ \frac{\partial \hat{t}_p}{r\partial\theta_{p+1}}. \tag{2.34}$$

To simplify Eqn. (2.31), we express

$$\frac{\partial \hat{t}_p}{r\partial\theta_p} = \frac{\mathrm{d}\hat{t}_p}{\mathrm{d}|\vec{l}_p|}\ \frac{\partial|\vec{l}_p|}{r\partial\theta_p} \tag{2.35}$$

$$\frac{\mathrm{d}\hat{t}_p}{\mathrm{d}|\vec{l}_p|} = \frac{\mathrm{d}(t_p/|\vec{l}_p|)}{\mathrm{d}|\vec{l}_p|} = \frac{1}{|\vec{l}_p|}(g_p - \hat{t}_p) = \hat{g}_p/|\vec{l}_p|, \tag{2.36}$$

where $g_p \equiv \mathrm{d}t_p/d|\vec{l}_p|$ is defined as the axial stiffness and $\hat{g}_p \equiv g_p - \hat{t}_p$ is defined as the *modified axial stiffness*.

From Fig. 2.13b, we see that $\Delta l = r\Delta\theta\ (-\vec{v}_p \cdot \vec{l}_p)/|\vec{l}_p|$ and therefore,

$$\frac{\partial|\vec{l}_p|}{r\partial\theta_p} = \frac{(-\vec{v}_p \cdot \vec{l}_p)}{|\vec{l}_p|} \tag{2.37}$$

Substituting Eqn. (2.35 - 2.37) into Eqn. (2.31), we find

$$\frac{\partial f_p}{r\partial\theta_p} = \frac{\partial(-\vec{v}_p\cdot\vec{l}_p)}{r\partial\theta_p}\ \hat{t}_p - (\vec{v}_p\cdot\vec{l}_p)\ \frac{\hat{g}_p}{|\vec{l}_p|}\frac{(-\vec{v}_p\cdot\vec{l}_p)}{|\vec{l}_p|}. \tag{2.38}$$

Similarly, we simplify Eqns. (2.32 - 2.34)

With the above derivatives, we can now define the tangent stiffness matrix. For a single spring p, the tangent stiffness matrix, $\mathbf{K}_p$, relates small changes in rotor position to small changes in rotor forces

$$\begin{pmatrix}\delta f_p\\ \delta f_{p+1}\end{pmatrix} = \mathbf{K}_p\begin{pmatrix}r\delta\theta_p\\ r\delta\theta_{p+1}\end{pmatrix} \tag{2.39}$$

and can be expressed as

$$\mathbf{K}_p = \begin{pmatrix}n_p\\ n_{p+1}\end{pmatrix}\left[\hat{g}_p\right]\begin{pmatrix}n_p & n_{p+1}\end{pmatrix} + \mathbf{s_p}, \tag{2.40}$$

where $n_p \equiv -\vec{v}_p\cdot\vec{l}_p/|\vec{l}_p|$, $n_{p+1} \equiv -\vec{v}_{p+1}\cdot\vec{l}_p/|\vec{l}_p|$ and the *stress matrix* $\mathbf{s}_p$ is

$$\mathbf{s}_p = \begin{pmatrix} -\frac{\partial(\vec{v}_p\cdot\vec{l}_p)}{r\partial\theta_p}\ \hat{t}_p & -\frac{\partial(\vec{v}_p\cdot\vec{l}_p)}{r\partial\theta_{p+1}}\ \hat{t}_p \\ \\ \frac{\partial(\vec{v}_{p+1}\cdot\vec{l}_p)}{r\partial\theta_p}\ \hat{t}_p & \frac{\partial(\vec{v}_{p+1}\cdot\vec{l}_p)}{r\partial\theta_{p+1}}\ \hat{t}_p \end{pmatrix}. \tag{2.41}$$

To derive the total tangent stiffness $\mathbf{K}$ for the rotor chain, we first represent the tangent stiffness $\mathbf{K}_p$ in a global coordinate system as an $n\times n$ matrix, and then sum up all the $\mathbf{K}_p$ for the $n-1$ springs:

$$\mathbf{K} = \sum_{p=1}^{n-1}\mathbf{K}_p = \sum_{p=1}^{n-1}\mathbf{a}_p\left[\hat{g}_p\right]\mathbf{a}_p^T + \sum_{p=1}^{n-1}\mathbf{S}_p, \tag{2.42}$$

where

$$\mathbf{a}_p = \begin{pmatrix} 0 \\ \vdots \\ 0 \\ n_p \\ n_{p+1} \\ 0 \\ \vdots \\ 0 \end{pmatrix} \tag{2.43}$$

and

$$\mathbf{S}_p = \begin{pmatrix} \mathbf{O} & \cdots & & \mathbf{O} \\ \vdots & \mathbf{s}_{p11} & \mathbf{s}_{p12} & \vdots \\ \vdots & \mathbf{s}_{p11} & \mathbf{s}_{p12} & \vdots \\ \mathbf{O} & \cdots & & \mathbf{O} \end{pmatrix}. \tag{2.44}$$

In $\mathbf{a}_p$, the n_p and n_{p+1} terms are in the pth and $p+1$th row respectively, and all the other terms are zero. In $\mathbf{S}_p$, $\mathbf{s}_{pij}$ is the (i,j) element of the 2×2 stress matrix $\mathbf{s}_p$ for a single spring p and is located in the $(p-1+i, p-1+j)$ position of $\mathbf{S}_p$, and all the other terms in $\mathbf{S}_p$ are zero. Here $\mathbf{S}_p$ has a simpler form than that of Ref. [59] because we exploit the fact that only nearest neighbours are coupled in the topological chain.

2.C Simulation methods

We carry out the molecular dynamics simulations in Mathematica. The ODEs are solved by the function NDSolve, which uses a multi-step method (LSODA) by default.

In the simulations, we set the lattice spacing $a = 1$, the rotor mass $M = 1$, and an arbitrary time unit $t = 1$. The spring constant k is measured in units of M/t^2. The linear velocity of a rotor is measured in units of a/t. The initial velocity v_0 of a (anti)kink is defined as the velocity amplitude of the unit translation mode $\mathbf{e}^t$ and e_i^t is the mode component on the i-th rotor. Thus the initial kinetic energy is $\Sigma_i \frac{1}{2} m (v_0 e_i^t)^2 = \frac{1}{2} m v_0^2$.

2.D Peierls-Nabarro potential barrier via continuum theory

We derive the PN potential by discretizing the potential energy density in the continuum theory, i.e. taking the quasi-continuum limit. The PN potential is, by definition, the potential that the kink faces as it propagates along the adiabatic trajectory (ad. tr.) :

$$V_{PN}(X) = V(..., u_{n-1}, u_n, u_{n+1}, ...)|_{X \in ad.tr.}. \tag{2.45}$$

Here, X is the position of the (anti)kink center, u_n is the continuum field at lattice site n, V is a discretization of the potential energy density $V(\theta)$ in Eqn. (2.9) and is obtained by summing the potential $f(n, X)$ of each lattice site:

$$V(..., u_{n-1}, u_n, u_{n+1}, ...) = \sum f(n, X), \tag{2.46}$$

where

$$f(n, X) = \frac{2k}{\bar{l}^2}\left(\frac{a^2}{2}\frac{\mathrm{d}u_n}{\mathrm{d}(na)} + \overline{u}^2 - u_n^2\right)^2. \tag{2.47}$$

$f(n, X)$ is the approximate potential at a single site n when the (anti)kink center is at X. Here, we discretize the continuum potential energy density rather than directly use the exact form of the lattice potential in Eqn. (2.8), so that we can readily substitute u_n, the continuum field at site n, into $f(n, X)$ which results in an integrable solution. We choose the static solution ($v = 0$) of Eqn. (2.13) as the adiabatic trajectory:

$$u_n(X) = \pm\overline{u}\tanh\left(\frac{na - X}{w}\right), \tag{2.48}$$

where the "$+$" is for the antikink, "$-$" is for the kink, and the width of the (anti)kink $w = \frac{a^2}{2r\sin\overline{\theta}}$ [18]. Substituting Eqn. (2.48) into Eqn. (2.47), we find

$$\begin{aligned} f(n, X) &= 0 && \text{for the kink,} \\ f(n, X) &= \frac{8k\overline{u}^4}{\bar{l}^2}\operatorname{sech}^4\left(\frac{na - X}{w}\right) && \text{for the antikink.} \end{aligned} \tag{2.49}$$

Thus $V_{PN}(X) = 0$ for the kink, in accordance with the fact that the kink configuration does not stretch springs and hence costs zero potential energy. For the antikink, we use the Poisson summation formula to express:

$$\begin{aligned} V_{PN}(X) &= \sum_{n=-\infty}^{+\infty} f(n, X) = \sum_{k=-\infty}^{+\infty} \hat{f}(k, X) \\ &= \sum_{k=-\infty}^{+\infty} \int_{-\infty}^{+\infty} \mathrm{d}n f(n, X) e^{-2\pi i k n}. \end{aligned} \tag{2.50}$$

To leading order, we only consider the first harmonic terms $k = 1$ and $k = -1$ ($k = 0$ recovers the continuum approximation). For $k = 1$, we find

$$\begin{aligned} &\int_{-\infty}^{+\infty} \mathrm{d}n f(n, X) e^{-2\pi i n} \\ &= e^{-2\pi i (X/a)} \int_{-\infty}^{+\infty} \mathrm{d}n' \frac{8k\overline{u}^4}{\bar{l}^2} \operatorname{sech}^4\left(\frac{n'a}{w}\right) e^{-2\pi i n'}. \end{aligned} \tag{2.51}$$

The complex exponential suggests a sinusoidally varying potential along the coordinate X of the adiabatic trajectory, with a period that is equal to the lattice spacing a. We define the *PN barrier* (V_{PNB}) as the height of this sinusoidal potential. The last integral in Eqn. (2.51) can be completed using residues to yield

$$\begin{aligned} V_{PNB} &= \frac{4\pi^2\Big(\pi^2 + (a/w)^2\Big)}{3\Big(1 + 4(r/a)^2 - (a/w)^2\Big)\sinh(\pi^2 w/a)} \\ &\propto e^{-\pi^2 w/a} \qquad \text{for large } w/a. \end{aligned} \tag{2.52}$$

Chapter 3

Topological rotor chains with impurities

In this chapter we investigate topological rotor chains with impurities. In Sec. 3.1, we examine how kinks and antikinks interact with a spring stiffness impurity in the lattice. In Sec. 3.2, we make a connection between linear mode analysis and nonlinear dynamics of kink motion in the context of spring length impurities.

3.1 Spring stiffness impurities

In this section we numerically explore whether the kink-antikink asymmetry also manifests in the way these excitations interact with a single lattice impurity, a natural starting point to study their propagation in disordered lattices. For the conventional ϕ^4 models, previous studies on kink-impurity interactions (in both discrete models [66] and continuum field models [67]) have shown that scattering can result in transmission, trapping or reflection of kinks, depending on the type of the impurity, the attraction/repulsion strength of the impurity and the kink's initial velocity. Although similar scattering also occurs in the topological rotor chain model, we also find other novel phenomena, for instance, the kink can split into two kinks and one antikink. Moreover as we will see, kinks and antikinks no longer scatter in the same way

– a feature which underscores the kink-antikink asymmetry in our topological rotor chain. Fig. 3.1 summarizes all the possible scattering scenarios that we observe. In this chapter, we study impurities in properties of the springs, which yield a richer set of effects on the response than mass impurities.

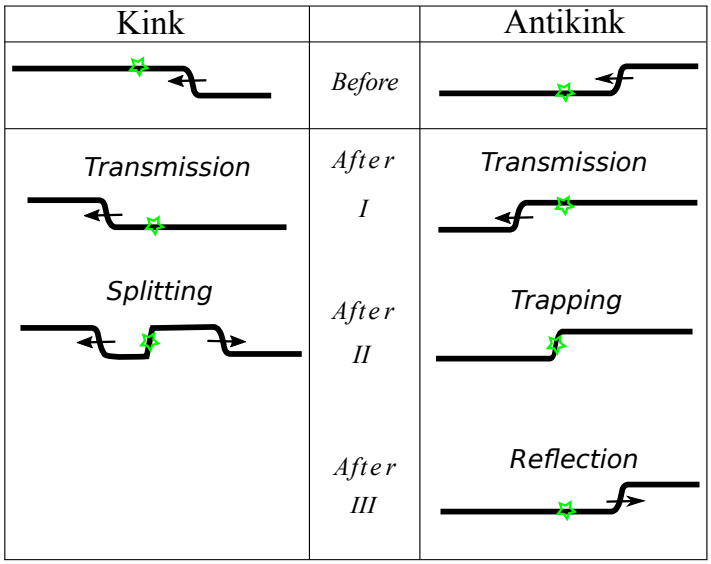

Figure 3.1. Illustrated are the possible scenarios for how the kink and antikink interact with a single impurity of spring stiffness. As indicated by the arrow, an initial kink or antikink approaches the impurity site (indicated by the green star) from the right. After scattering, the incident kink is either: (**I**) perfectly transmitted or (**II**) splits into a reflected kink, a transmitted kink and an antikink that gets trapped at the impurity site. The incident antikink is either: (**I**) perfectly transmitted, (**II**) trapped at the impurity site or (**III**) perfectly reflected.

In this section, we model an impurity by changing the spring stiffness constant at a single site (Fig. 2.1a). We study a topological chain with lattice spacing $a = 1$ and rotor length $r/a = 0.8$ and with equillibirum angle $\overline{\theta} = 0.28$. We perform Newtonian dynamics simulation on a system with 60 rotors using free boundary conditions, and for a range of impurity spring stiffness constant k_i and kink/antikink initial velocity v_0. See Fig. 3.1 for a table of the possible scattering scenarios that we observe.

Consider first the kink-impurity interaction. For most k_i and v_0, the kink simply passes through the impurity and may excite an impurity mode, which can be seen in the form of small fluctuations in the middle of the chain as shown in Fig. 3.2a. When the impurity spring is sufficiently soft, the incident kink splits into three: a transmitted kink, an antikink that is trapped at the impurity and a reflected kink. This is shown in Fig. 3.2b.

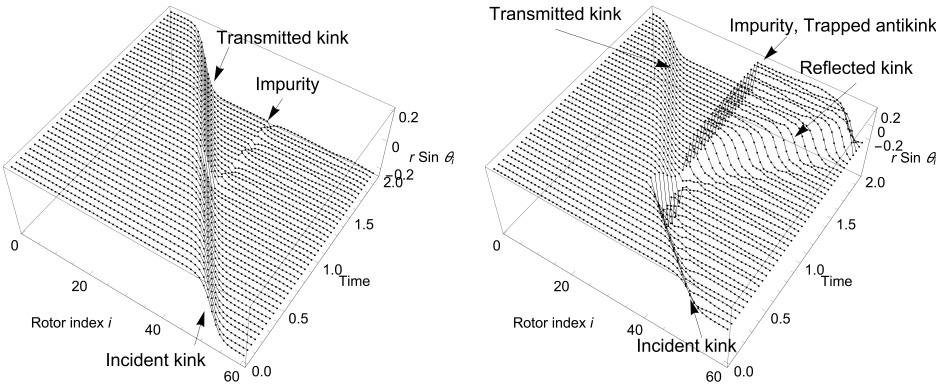

(a) **(b)**

Figure 3.2. A kink interacts with an impurity (different spring stiffness) and is either (**a**) transmitted, shown here for $v_0 = 4.0$ and $k_i/k = 0.10$ or (**b**) splits into a transmitted kink, a reflected kink and an antikink trapped at the impurity, shown here for $v_0 = 9.6$ and $k_i/k = 0.01$. The non-dimensional parameters are $M = 1, k = 10000, r/a = 0.8, \bar{\theta} = 0.28$.

Antikink scattering results in an ever richer set of behaviors. Recall that the springs near the location of an antikink are always stretched significantly, see Fig. 2.4b. For k_i/k near 1, the antikink gets transmitted with energy dissipation and thus slows down (Fig. 3.3a). Softening the impurity spring stiffness creates an attractive potential well for the antikink. The antikink may then release a part of its potential energy and get trapped at such an impurity site (Fig. 3.3b). If the impurity spring is made even softer, such that an antikink can no longer transfer its kinetic energy forward or dissipate it sufficiently quickly to be trapped, the incident antikink is completely reflected (Fig. 3.3c). For similar reasons, a stiffer impurity acts like a repulsive potential

well that can reflect slow moving antikinks.

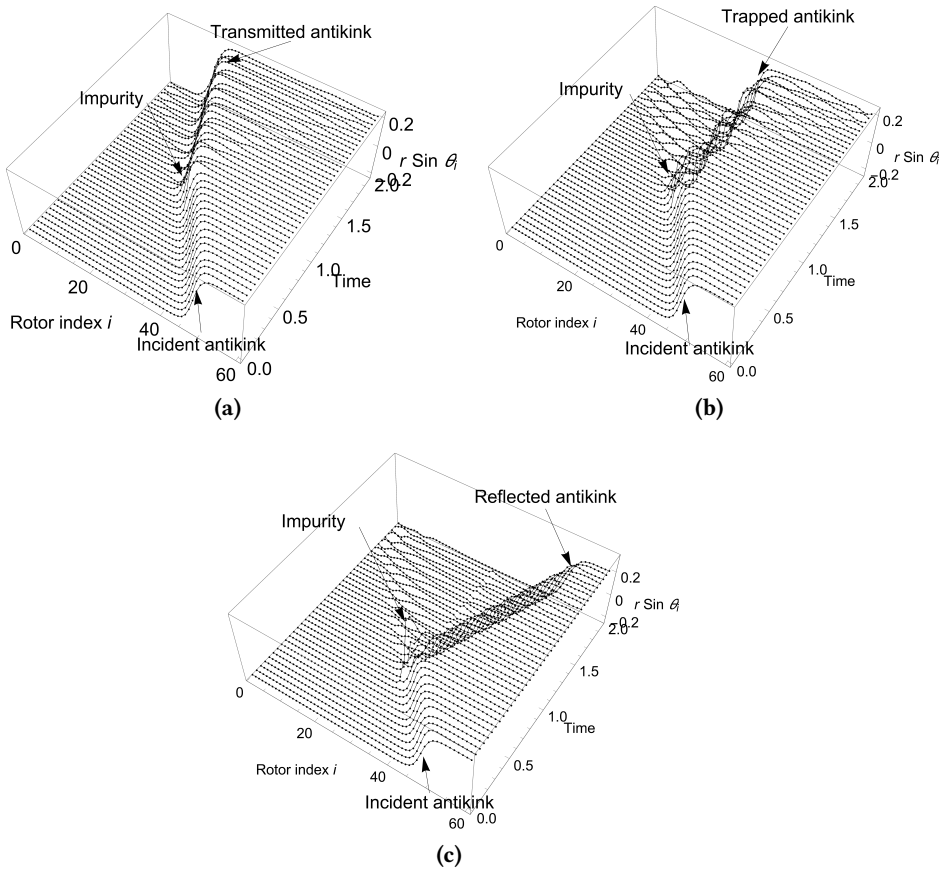

Figure 3.3. An antikink interacts with an impurity and is either (**a**) transmitted, shown here for $v_0 = 4.0$ and $k_i/k = 0.80$, (**b**) trapped, shown here for $v_0 = 4.0$ and $k_i/k = 0.70$ or (**c**) reflected, shown here for $v_0 = 4.8$ and $k_i/k = 0.20$. The system parameters are the same as Fig. 3.2.

These numerical results are summarized in the phase diagrams in the space of k_i and v_0 in Fig. 3.4. First, note that a kink (Fig. 3.4a) behaves quite differently from an antikink (Fig. 3.4b). For instance, a kink is never completely

trapped or reflected by an impurity. The reason is that it has zero intrinsic potential energy and thus, no potential energy to lose during a scattering event. As a collective object, the kink experiences a flat potential landscape along the chain. It will always go through the impurity, unless k_i is so soft or v_0 is so large that the initial kinetic energy of the kink is sufficient to stretch the impurity spring to form a pinned antikink. That is when scattering results in the kink being split. This also explains the positive slope of the boundary line between these two regimes. (The topological constraints of the field require that the number of kinks minus the number of antikinks remains constant [50], which is one for our boundary conditions.)

For an antikink, the scattering phase diagram has more regimes (Fig. 3.4b). The positive slope of the boundary curve at higher k_i between the upper reflection regime (square) and the transmission regime (circle) comes from the fact that the higher the barrier is, the faster the antikink needs to be, to get transmitted. The negative slope of the boundary between the transmission regime (circle) and the trapping regime (triangle), suggests that a softer impurity spring causes the antikink to dissipate more energy. The antikink then needs a sufficiently high initial velocity to avoid being trapped at such an impurity site. The positive slope of the curve between the trapped regime (triangle) and the lower reflection regime (square) suggests that if the impurity spring is so soft such that it can no longer transform the kinetic energy into other forms or channelize the kinetic energy to the other side of the impurity sufficiently "quickly", an antikink incident with sufficiently high energy will then be completely reflected. (In simulations we find that the maximum initial velocity with which we can launch an antikink is around $v_0 = 12$. Above this, the antikink itself becomes unstable and tends to quickly disintegrate.)

For the topological rotor chain, the antikink scattering behaviour is therefore very similar to the ones reported for kinks and antikinks in previous studies on the ϕ^4 model [66, 67]. In addition, for normal ϕ^4 kinks and antikinks, one also observes resonance windows which are alternating regimes of the excitation being reflected or trapped, along the axis of initial velocities for a given impurity strength. These have not been observed during our simulations of the discrete topological chain. Instead, we only observe a small range of alternating regimes where the antikink is transmitted or trapped, around $k_i/k = 0.75$ and $v_0 = 3.6$ in Fig. 3.4b. We leave a detailed

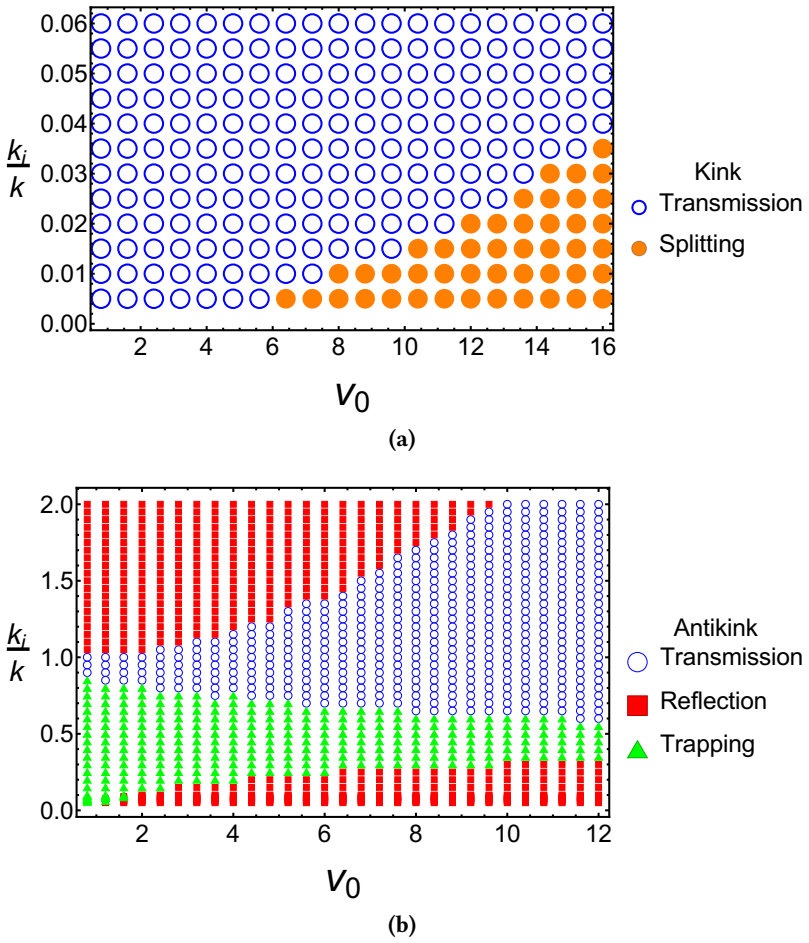

Figure 3.4. The phase diagram of the scattering behavior in the parameter space of normalized spring stiffness constant of impurity k_i/k and kink initial velocity v_0 for (**a**) the kink and (**b**) the antikink. The system parameters are the same as Fig. 3.2. The lower limit of v_0 for the antikink is around 0.7, below which even the PN barrier in a perfect chain will capture the antikink.

characterization of the resonance energy exchange between these modes for future studies.

3.2 Spring length impurities

In Sec. 2.4 we perform linear mode analysis of the topological chain, and in Sec. 3.1 we study the nonlinear motion of (anti)kinks with impurities. Here in this section we will show in a qualitative way that there is a connection between these two aspects. For convenience, we investigate another type of impurity: the spring length.

3.2.1 Linear mode analysis

We start with a qualitative observation of the linear vibrational modes. For a perfect topological rotor chain with free boundary conditions, there exists only one zero mode – the translation mode of the kink. This is what the Maxwell-Calladine counting predicts [57, 58]: the chain has n rotors as degrees of freedom and $n-1$ springs as constraints, and the former quantity minus the latter equals the number of zero modes minus the number of states of self stress. (In a perfect chain there is no states of self stress.) This counting does not depend on the geometrical parameters of the chain components.

Now we increase one geometrical parameter, namely the length of the middle spring l_0, so that it is an impurity in the system (Fig. 3.5). As long as no state of self stress is created, there remains only one zero mode. However, as l_0 approaches a critical value $l_{critical}$, several qualitative changes take place: (1) The profile of the chain varies significantly. There are two kinks, one on each side of the impurity spring. (2) Eigenmode analysis shows that the amplitude of the zero mode has two prominent parts that are spatially separated, each of which is localized around a kink as an individual translation mode. Both parts of the zero mode point towards the same direction. (3) An additional soft vibrational mode appears, whose amplitude also has two separated parts just like the zero mode. But the directions of these two parts are opposite to each other. This soft mode has a frequency close to zero, much lower than that of kink shape modes. (4) A soft tensional mode dual to the soft vibrational mode emerges, being localized around the impurity spring. (A tensional mode is a vector whose components are the infinitesimal spring tensions caused by the infinitesimal motion of the dual vibrational mode. The duality comes from the fact that the tensional mode is an eigenfunction of the

supersymmetrical "partner" of the dynamical matrix, while the vibrational mode is an eigenfunction of just the dynamical matrix. See [19, 25, 26] for more details.)

These changes do not contradict the Maxwell-Calladine counting: only one vibrational mode has strictly zero frequency, unless l_0 actually reaches $l_{critical}$. In that case, the frequencies of both the soft vibrational mode and the soft tensional mode go to zero. By definition the tensional mode becomes a state of self stress. Then the Maxwell-Calladine counting still holds as there are now two zero modes and one state of self stress.

The above analysis only considers infinitesimal oscillations around zero-energy equilibrium points. In the next section, we study qualitatively the nonlinear motion of kinks with finite energy, providing a perspective complementary to the linear analysis.

3.2.2 Nonlinear dynamics: linkage limit

3.2.2.1 Setup: Hamiltonian

To simplify the problem, we consider the linkage limit, where all the springs in a perfect chain are non-deformable rigid bars so that they are holonomic constraints. There is only one degree of freedom which is the translational motion of the kink. We choose the kink position x as a collective variable to describe this degree of freedom.

Then we introduce the impurity by replacing the middle rigid bar with a longer spring that is "soft" (i.e. with a finite spring stiffness constant) (Fig. 3.6a). A soft spring does not strictly constrain the angles of the two rotors it connects but rather gives a potential energy to deviations from its preferred length. The chain then has one fewer constraint, which in turn means that it has two degrees of freedom. We regard the whole chain as two linkage sub-chains, then the two degrees of freedom are shared by the two kinks of the sub-chains, which we call Kink 1 and Kink 2 with position x_1 and x_2 respectively. The coordinate system for the discrete chain model is illustrated in Fig. 3.6a, and its precise definition is contained in Appendix 3.A. We see that by taking the linkage limit, the number of degrees of freedom is reduced from the number of rotors (16 for the chain in Fig. 3.6a) to the number of kinks (2 for two kinks).

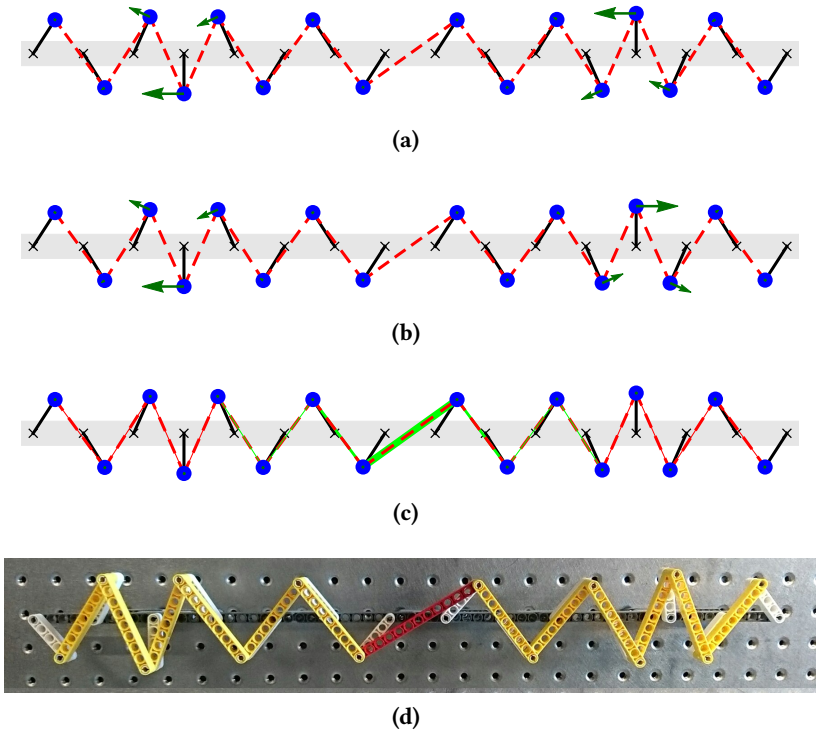

Figure 3.5. The zero vibrational mode (**a**), the soft vibrational mode (**b**), and the soft tensional mode (**c**) of a topological chain with a longer spring in the middle as an impurity. The configuration parameters are $\overline{\theta} = 0.58$, $r/a = 0.8$, $\overline{l}/a = 1.68$, $l_0/a = 2.30$ and $l_{critical}/a = 2.31$. The soft mode frequency is 7.7×10^{-9} in the unit of $(r/a)\sqrt{k/M}$, which means the mode is much "softer" than the kink shape mode whose frequency is of the order 10^{-2}. In (**a**) and (**b**), the arrows indicate the mode amplitude of the displacement of each rotor. In (**c**), the thickness of the green bars indicates the tensional mode amplitude on each spring. All the springs, both normal ones and the impurity, have the same stiffness. (**d**) shows a LEGO demonstration.

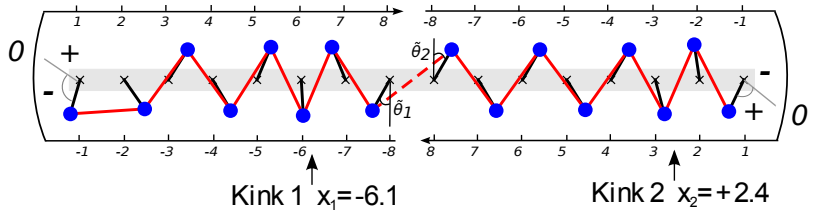

(a)

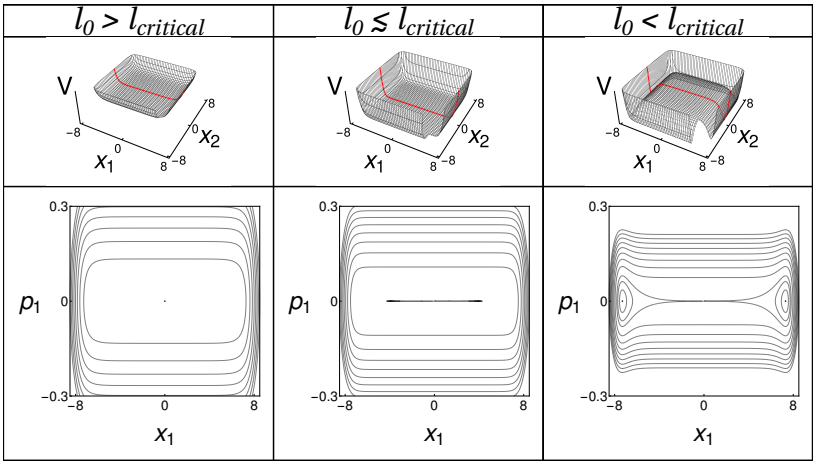

(b)

Figure 3.6. (**a**) Illustration of the coordinate system of a topological rotor linkage chain with $\overline{\theta} = 0.58$, $r/a = 0.8$, $\bar{l}/a = 1.68$ and $l_{critical}/a = 2.31$. The linkage bars are the solid lines and the impurity spring is the dashed line. In (**b**), the upper panels show the potential functions in 2D configuration space for various l_0. One corner of the function is trimmed for visualization. The red curve corresponds to the potential for Kink 1 in the one d.o.f. case where Kink 2 is fixed at $x_2 = 0$. The lower panels show the phase portraits of Kink 1.

Now we derive the Hamiltonian. Note that the potential energy only comes from the deformation of the impurity spring, which in turn just depends upon the angles of the head rotors $\tilde{\theta}_i$. Since x_i is the degree of freedom, it determines the state of the sub-chain i, including $\tilde{\theta}_i$. Thus from the continuum theory (Eq. 2.13 where $u = r\sin\theta$), we obtain $\tilde{\theta}_i(x_i)$:

$$\sin\tilde{\theta}_i(x_i) = \sin\overline{\theta}\tanh\left(\frac{r\sin\overline{\theta}(|x_i| - \tilde{x}_i)}{a^2}\right), \tag{3.1}$$

where $\overline{\theta}$ is the equilibrium angle of a perfect chain, a is the lattice spacing, r is the rotor length, and $\tilde{x}_i$ is the position of the head rotor.

Putting $\tilde{\theta}_i(x_i)$ into the Hookean spring potential $V = \frac{1}{2}k(l_{1,2} - l_0)^2$ where $l_{1,2}$ takes the form in Eq. (2.6) and l_0 is the rest length of the impurity spring, we obtain the potential function $V(x_1, x_2; l_0)$ as a function of the kink positions (Fig. 3.6b). We formally define the effective kink momentum p and mass m for the sub-chains in terms of the total kinetic energy of the rotors $T = \sum_{j=1}^{8}\frac{1}{2}mr^2\dot{\theta}_j^2 \equiv \frac{1}{2m}p^2$. Thus the Hamiltonian $H(x_1, x_2, p_1, p_2; l_0) = T(p_1, p_2) + V(x_1, x_2; l_0)$ is obtained.

3.2.2.2 Individual kink: Phase portrait

We first investigate a simple case where Kink 2 is fixed at $x_2 = 0$ and only Kink 1 is allowed to move. Then the chain has only one degree of freedom x_1. With the Hamiltonian, we draw the phase portraits of x_i for various l_0 in Fig. 3.6b. We find that there is a critical value for the rest length of the impurity spring

$$l_{critical} = \sqrt{(2r\sin\overline{\theta} + a)^2 + (2r\cos\overline{\theta})^2}, \tag{3.2}$$

which determines the pattern of the phase portrait and the qualitative behavior of the dynamics of the chain.

When $l_0 < l_{critical}$, the dumbbell-shaped separatrix curve extends almost across the whole reachable region of x_1. The two equilibrium points at $x_1 \approx +8$ and $x_1 \approx -8$ correspond to the kink being localized around the impurity spring. x_1 is either positive or negative depending on the orientation of the end rotor. At these two equilibrium points the impurity spring is not stretched.

The behavior of Kink 1 depends on whether E is above or below the separatrix curve's energy $E_c = \frac{1}{2}k(l_0 - l_{critical})^2$. If $E < E_c$, the trajectory in the phase plane stays inside the region enclosed by separatrix and circulates around one of the equilibrium points. In real space, Kink 1 makes small oscillations around the impurity spring at either $x_1 \approx -8$ or $x_1 \approx +8$. If $E > E_c$ the trajectory moves in the region outside of the separatrix. In real space, Kink 1 is able to go over the sub-chain end and move back and forth between $x_1 \approx -8$ and $x_1 \approx +8$.

When l_0 approaches $l_{critical}$ from below and exceeds $l_{critical}$, the separatrix curve shrinks and disappears. The two equilibrium points merge into one at $x_1 = 0$ at the end of the sub-chain [1]. In real space, the kink with finite energy oscillates around the sub-chain end $x_1 = 0$.

3.2.2.3 Two kinks: Accessible configuration space

The phase space of a chain with two kinks is 4D. For the convenience of visualization, we investigate the potential function $V(x_1, x_2; l_0)$ in the 2D configuration space. The shape of the potential depends on l_0 and determines the qualitative dynamics of the two kinks. We also perform simulations of Newtonian dynamics to investigate the qualitative behavior of the nonlinear motion of the kinks.

When $l_0 < l_{critical}$ (Fig. 3.7a), the potential looks like a square Mexican hat. The bottom of potential valley is a square ring, on which all the points are at zero energy. In linear mode analysis, we find a zero mode along the valley and a soft mode along the transverse direction. We will show that the nonlinear dynamics at finite energy possesses the traits that are closely related to those in the linear analysis at zero energy.

Note that the impurity spring is maximally stretched at $x_1 = x_2 = 0$, and the corresponding potential maximum $E_c = \frac{1}{2}k(l_0 - l_{critical})^2$. It is the minimal energy for both kinks to move away from the impurity. If $E < E_c$, the two kinks take turns moving on their respective sub-chains. One kink oscillates near the impurity spring, while the other kink moves away. The nonlinear dynamics of the kinks is visualized as a trajectory going along the

[1] In the language of dynamical systems, this process is called a *supercritical pitchfork bifurcation.*

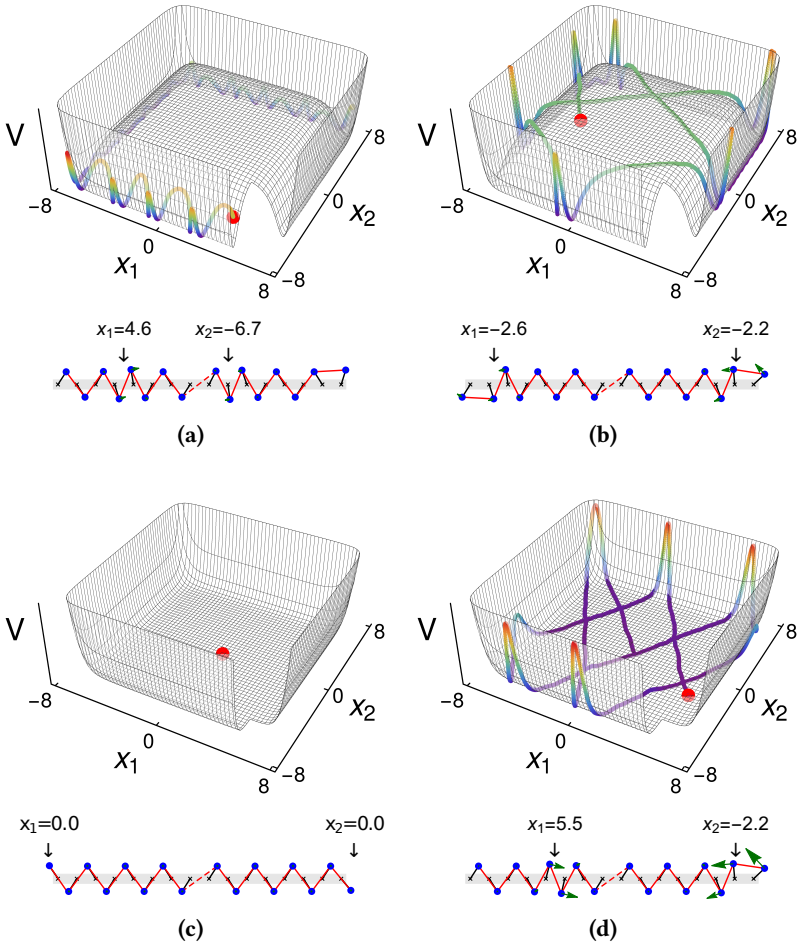

Figure 3.7. The trajectories of the chain generated by simulations of Newtonian dynamics on the theoretical potential function in the configuration space at **(a)** $l_0 < l_{critical}$, $E < E_c$, **(b)** $l_0 < l_{critical}$, $E > E_c$, **(c)** $l_0 = l_{critical}$, $E = E_c = 0$, and **(d)** $l_0 > l_{critical}$. In the top figures of **(a)** and **(b)**, the color scale of the trajectories indicates the potential energy of the chain in arbitrary units. The big red dots correspond to the configuration of the real-space chains shown in the bottom figures of each panel.

bottom of the potential valley. The accessible region in the configuration space is a square annulus, at the corner of which the major part of energy is transferred from the one kink to another. In fact, this can be interpreted as the motion of a single "split" kink through the system.

When $E \geq E_c$ (Fig. 3.7b), there is sufficient energy for both kinks to move away from the impurity spring simultaneously. In the configuration space, the trajectory gets out of the potential valley and climbs up to the 2D plateau in the middle. The accessible region now is a square disk. In real space, the kinks independently hit the impurity spring and get reflected.

When $l_0 = l_{critical}$ (Fig. 3.7c), the linear mode analysis predicts that the chain model in Fig. 3.7c has two zero modes, each being localized around the kink at the end of the respective sub-chain, and a state of self stress localized around the impurity spring. From the viewpoint of nonlinear dynamics, the potential function changes qualitatively: As l_0 approaches $l_{critical}$, the square ring of the potential valley shrinks into one point at $x_1 = x_2 = 0$, and E_c goes to zero. In other words, the Mexican hat transforms into a single basin. In this shrinking process, the soft mode, which corresponds to the oscillation transverse to the valley, transitions into a zero mode, because the depth of the valley vanishes. In terms of nonlinear dynamics, this transition means that no matter how small the total energy E is, the accessible region in the configuration space is always a square disk rather than a square annulus.

When $l_0 > l_{critical}$ (Fig. 3.7d), the impurity spring is compressed, which gives a minimum potential energy $E_{min} = \frac{1}{2}k(l_0 - l_{critical})^2$ for the static configuration. In a linear analysis, the two zero modes become normal modes with finite frequency, as the impurity spring pushes the two kinks to the chain ends, generating a finite restoring force for the motion of the modes. In the nonlinear dynamics, the accessible region of the kinks is still a square disk.

Fig. 3.8 summarizes the above results with E and l_0 as parameters. When $l_0 \leq l_{critical}$, the curve $E_c = \frac{1}{2}k(l_0 - l_{critical})^2$ marks the transition of the accessible region in configuration space from an annulus to a disk. Note that we only investigate the case of $l_0 > \bar{l}$, in which Fig. 3.8 is valid. For $l_0 < \bar{l}$ case, the potential landscape takes a different form, and so does the possible transition. We do not cover this case in this paper, however, as we have made the connection between linear mode analysis and nonlinear dynamics.

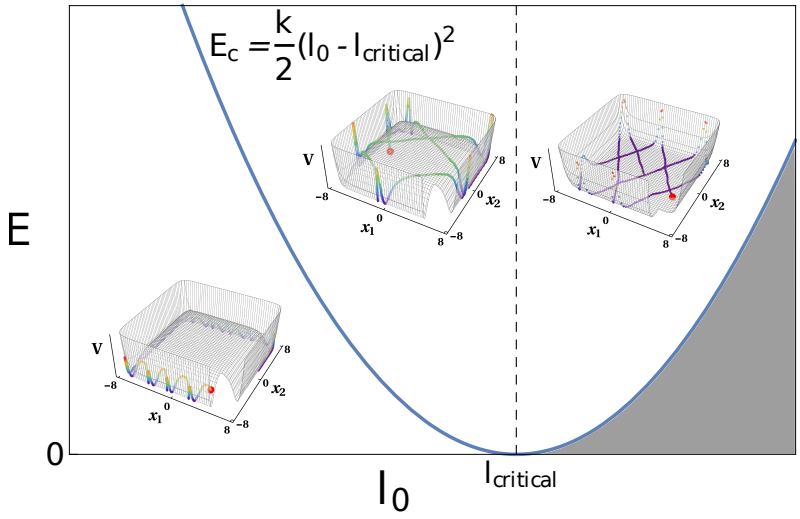

Figure 3.8. The parameter space of the total energy E and the impurity spring length l_0. The critical energy E_c as a function of l_0 forms a parabola. The chain shows different dynamical behaviors across the left branch of the parabola. The vertical dashed line of $l_0 = l_{critical}$ is the boundary line across which the shape of the potential function transitions qualitatively. The gray area below the right branch of the parabola is energetically forbidden.

Appendix

3.A Convention of kink coordinates in discrete models

The concept of kinks stems from the continuum ϕ^4 theory. To extend this concept to the discrete chain model, we define the coordinate system of a sub-chain kink as follows (Fig. 3.6a): The absolute value of the position of a kink equals the rotor's integer index if the rotor is vertical, otherwise the position is a real number interpolating between the indices of the two neighboring rotors that are leaning opposite to each other. The positional interpolation is proportional to the linear interpolation between the absolute values of the

angles of two neighbor rotors. The rotor angles are the measured against the vertical alternatively, as mentioned in Sec. 2.2. When a kink approaches the end points of the chain, the end rotor flips over. Here the kink profile from the continuum theory ceases to be valid. Thus we take as our convention that a kink is at the origin of the coordinate system when the end rotor is collinear with the spring connecting to the next rotor, and its sign depends on whether the end rotor leans upwards or downwards. The coordinate between 0 and 1 (or -2) is obtained by linear interpolation of the angles of the end rotor at 0 and 1 (or -2). In this *ad hoc* convention, the chain forms a state of self stress when both kinks are at origin. The two sub-chains are aligned head-to-head, and the two head rotors ($|x_i| = 8$) are coupled by the impurity spring.

Chapter 4

Twisted kagome lattices: band structure analysis

4.1 What is a kagome lattice

In this chapter we study the so-called kagome lattice. The name kagome comes from Japanese, where "kago" means "basket", and "me" means "eye". As shown in Fig. 4.1a, it is a pattern that has been used in Japanese basketry for a long time [68, 69]. If we extend this pattern into an infinite lattice, and put a mass at each crossing point of the bamboo ribbons and a spring between each pair of neighboring masses, then we obtain a mechanical model of kagome lattice (see Fig. 4.1b). It can be seen as a network of corner-sharing equilateral triangles. There are other ways of building a mechanical kagome lattice, such as pin-jointing rigid triangular plaquettes (Fig. 4.2) or rigid bars (Fig. 4.3).

The kagome lattice as a mechanical model has been studied quite extensively in terms of phonon spectrum, elasticity, and rigidity [13, 14, 26, 28, 42, 69, 71–73]. It features an internal zero-energy motion, in which neighboring triangles are twisted towards alternating directions [25, 43, 53, 74–77] (see Fig. 4.2 or Fig. 4.3). This is a finite "collapsing" mechanism that changes the geometry of the unit cell. We call it the *twisting mechanism*. Its infinitesimal counterpart is termed the *twisting mode*, which is known as a Guest-Hutchinson mode [74].

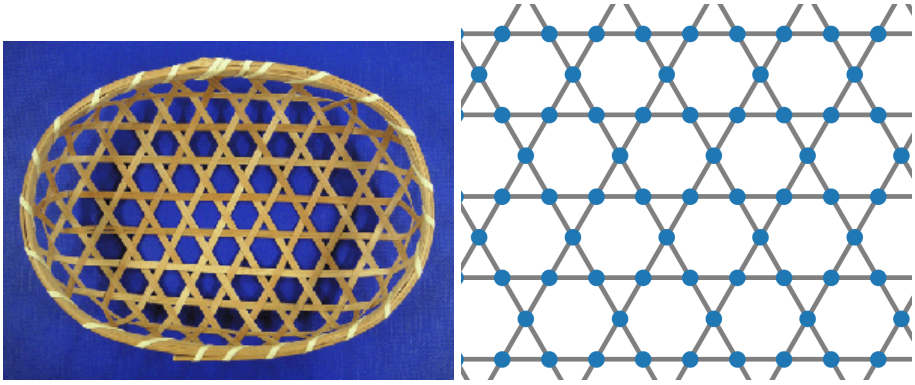

(a) (b)

Figure 4.1. (**a**) A basket with kagome pattern. The figure is from Ref. [70]. (**b**) A mechanical kagome lattice of masses and springs.

The infinitesimal vibrations of the lattice are described, in the harmonic approximation, by a phonon band structure. This band structure is determined by the content and geometry of the lattice unit cell. As the twisting mechanism changes the geometry without costing any energy, it turns out to be an easy way to tune the vibrational properties of the lattice. Although this idea has been considered before [53], we investigate it in a more detailed way and present the results in the following sections.

The twisting mechanism is the integrated version of the twist mode. As it has only one degree of freedom, it can be described by the twisting angle θ of each triangle around its center. We define ϑ to be the angle between two lines connecting two centers of adjacent triangles (see Fig. 4.4). Then θ is defined as

$$\theta = (180^\circ - \vartheta)/2 \tag{4.1}$$

In this work, θ ranges from 0° to 60°. When the lattice is untwisted, $\theta = 0^\circ$ (Fig. 4.2a). When the twisted triangles touch each other, $\theta = 60^\circ$ (Fig. 4.2d).

We choose a unit cell which has the shape of a rhombus with angle 60° and consists of two triangles (see Fig. 4.4). The Bravais lattice primitive vectors

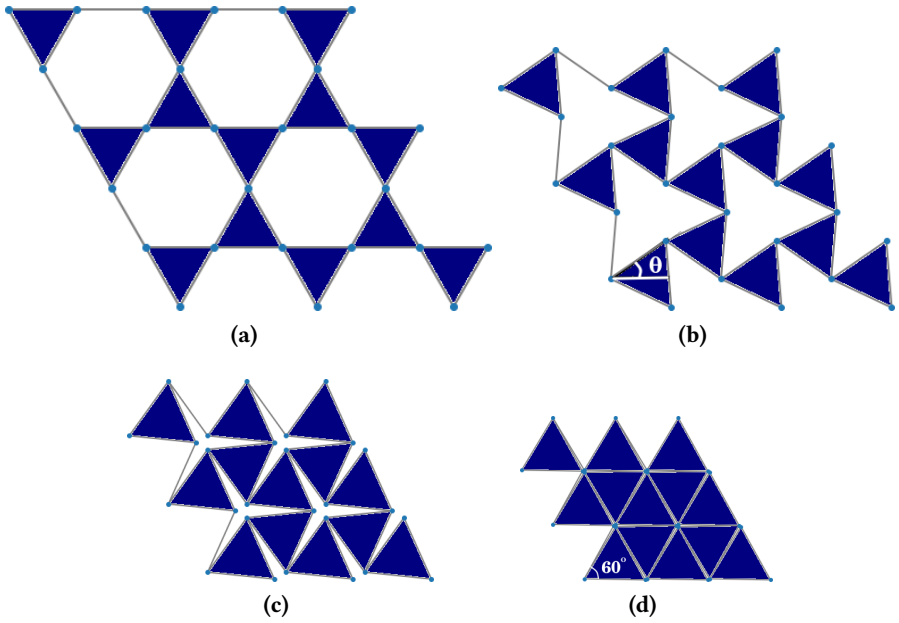

Figure 4.2. A mechanical kagome model made of triangular plaquettes. The framework collapses through a zero-energy mechanism without deformation of its rigid components.

are

$$a_1 = (2\ell\cos\theta, 0), \tag{4.2}$$

$$a_2 = (\ell\cos\theta, \sqrt{3}\ell\sin\theta), \tag{4.3}$$

where ℓ is the spring length.

The coordinates of the masses are

$$(x_1, y_1) = \left\{\frac{1}{3}\ell\left(\sin\left(30^\circ - \theta\right) + \cos\theta\right), \frac{1}{2}\ell\left(\sqrt{3}\cos\theta - \sin\theta\right)\right\}, \tag{4.4}$$

$$(x_2, y_2) = \left\{\ell\left(\frac{\sin\theta}{\sqrt{3}} + \cos\theta\right), 0\right\}, \tag{4.5}$$

$$(x_3, y_3) = \left\{-\frac{1}{6}\ell\left(\sqrt{3}\sin\theta - 9\cos\theta\right), \frac{1}{2}\ell\left(\sin\theta + \sqrt{3}\cos\theta\right)\right\}. \tag{4.6}$$

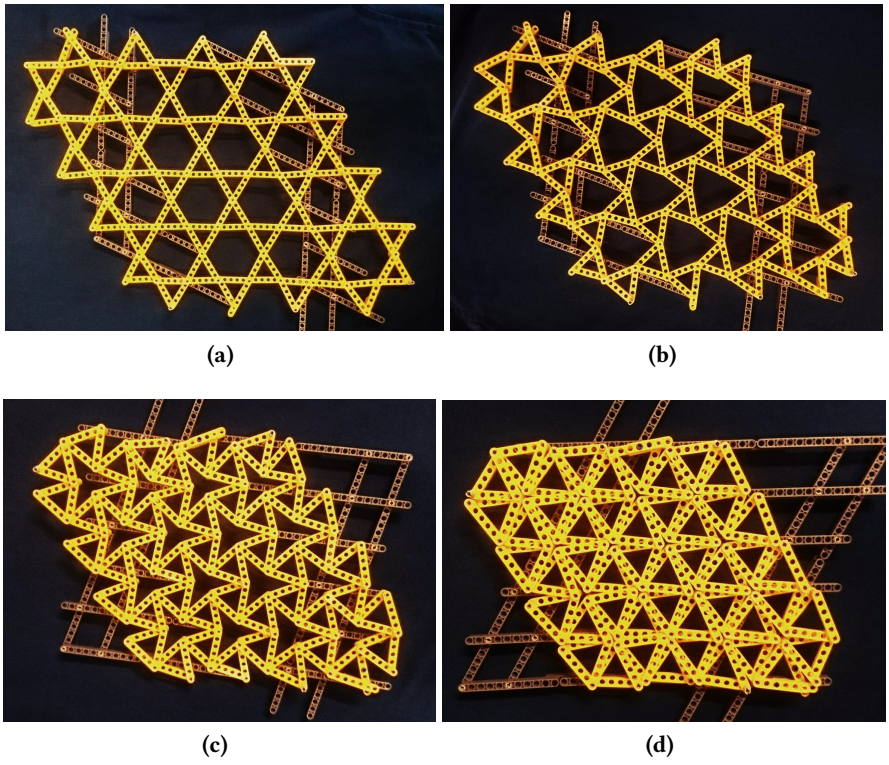

Figure 4.3. A mechanical kagome model made of LEGO. The yellow bars consist of the kagome framework, while the gray bars provide the handle for the twisting mechanism.

4.2 Lattice dynamics of kagome lattices

Since we study the vibrational properties of kagome lattices, we first briefly explain the theory of lattice dynamics, and concept of the phonon band structure. For rigorous details, we refer to the textbooks [78–80].

We study the harmonic oscillation of a lattice system of masses. Its equa-

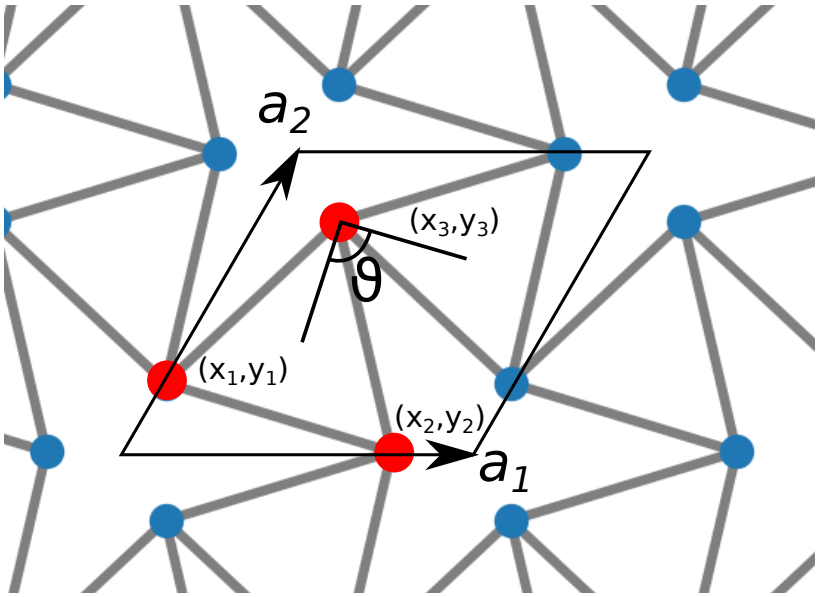

Figure 4.4. Our choice of the unit cell for the twisted kagome lattice. The masses inside the unit cell are shown in red. ϑ is the angle between two lines connecting two centres of adjacent triangles. The twisting angle $\theta = (180^\circ - \vartheta)/2$.

tion of motion in real space can be written as:

$$\boldsymbol{M}\ddot{\boldsymbol{u}} = -\partial_{\boldsymbol{u}}\Phi \approx -\left(\partial_{\boldsymbol{u}}^2\Phi\right)\Big|_{\boldsymbol{u}=0}\boldsymbol{u}, \tag{4.7}$$

where $\boldsymbol{M}$ is the mass matrix, Φ is the total potential energy, and $\boldsymbol{u}$ is the displacement vector of masses. We take the time Fourier transform of the Eqn. (4.7) to obtain the secular equation

$$\omega^2\hat{\boldsymbol{u}} = \boldsymbol{D}\hat{\boldsymbol{u}} \tag{4.8}$$

where $\boldsymbol{D} = -\boldsymbol{M}^{-1}\left(\partial_{\boldsymbol{u}}^2\Phi\right)\Big|_{\boldsymbol{u}=0}$ is the dynamical matrix in real space, and ω is the oscillation frequency.

Since the lattice is spatially periodic, we can decompose all solutions in terms of plane waves of the form

$$\boldsymbol{u}(\boldsymbol{x}, t) = \boldsymbol{\epsilon} \exp\left[i(\boldsymbol{k} \cdot \boldsymbol{x} - \omega t)\right], \tag{4.9}$$

where $\boldsymbol{\epsilon}$ is a polarization vector giving the displacement of the masses in a unit cell, $\boldsymbol{k}$ is the wave vector, $\boldsymbol{x}$ is a Bravais vector giving the position of unit cells, and t is time. This allows us to define the Fourier transformed dynamical matrix $\boldsymbol{D}(\boldsymbol{k})$ such as

$$\omega^2 \boldsymbol{\epsilon} = \boldsymbol{D}(\boldsymbol{k}) \boldsymbol{\epsilon}. \tag{4.10}$$

The eigenvalues $\omega(\boldsymbol{k})$ and eigenvectors $\boldsymbol{\epsilon}(\boldsymbol{k})$ of $\boldsymbol{D}(\boldsymbol{k})$ are called the dispersion relation and the polarization vectors. They form a complete set of solutions of the equation of motion of the lattice called normal modes, which describe the small oscillations of the lattice around its equilibrium configuration.

The wave vector $\boldsymbol{k}$ also lives in a periodic space called the reciprocal space. Its has a primitive cell in which the points are closer to the origin than any to any other reciprocal lattice points. It is uniquely defined as the first Brillouin zone. The first Brillouin zone of the kagome lattice is shown in Fig. 4.5. The points of high symmetry are denoted.

Now we study the eigenvalue equation (4.10) carefully. Since it is Fourier transformed, the dimension of $\boldsymbol{\epsilon}(\boldsymbol{k})$ equals the number of degrees of freedom in a unit cell. For the kagome lattice, each unit cell has six degrees of freedom. This means that $\boldsymbol{D}(\boldsymbol{k})$ is a 6×6 matrix. As it can be shown that $\boldsymbol{D}(\boldsymbol{k})$ is Hermitian [1], it has six real eigenvalues for each $\boldsymbol{k}$. Since the wave vector $\boldsymbol{k}$ can vary continuously, each eigenvalue $\omega(\boldsymbol{k})$ as a continuous function forms a "band" in the reciprocal space. We plot $\omega(\boldsymbol{k})$ to show the six phonon bands (see Fig. 4.6). Two bands whose frequencies equal zero at the Γ point in the reciprocal space are conventionally called acoustic bands, while the other four bands are optical bands.

We see that each of the six modes at the Γ point are identical in all unit cells. Among them are the two global translation modes, the twisting mode,

[1] With our convention, $\boldsymbol{D}(\boldsymbol{k})$ is only pseudo-Hermitian, but it is possible to define a Hermitian one. See Ref. [79].

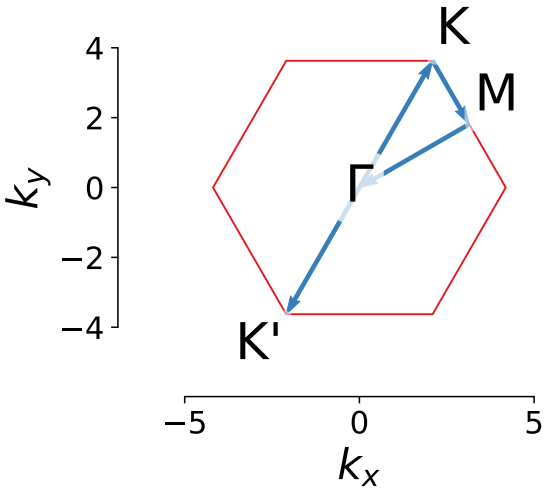

Figure 4.5. The first Brillouin zone of the kagome lattice, with its high symmetry points of $\Gamma = (0, 0)$, $K = (2\pi/3, 2\sqrt{3}\pi/3)$, $K' = (-2\pi/3, -2\sqrt{3}\pi/3)$ and $M = (\pi, \sqrt{3}\pi/3)$, in unit of $|a_1|^{-1}$, and a path used for the band structure in the following.

and three others. Notice that the frequency of the twisting mode is not zero for general twisting angle, which seems to be contradictory with what is said in the previous section that the twisting mechanism is a zero-energy finite motion. The subtlety is that we have to allow the unit cell to deform to be compatible with the changing framework along the finite mechanism. In this way the twisting mode is made to be a zero mode. This detail is well explained in Ref. [74–76]. Here in the theory of lattice dynamics, we do not make this assumption of deformable unit cell, so the twisting mode does not have zero frequency.

The phonon spectrum is obtained by projecting all the phonon bands to the ω axis. The density of states of phonons describes the number of states per interval of frequency and shows directly important lattice vibrational properties such as the band gaps, a frequency interval where no normal mode lies in. To estimate it, we compute the histogram of the phonon modes with respect to the frequency. We will show this in the next section in detail.

4.3 Influence of the twist: the band gap opens up

In the previous section, we show the linear theory of lattice motion, and ultimately, the phonon band structure. Usually, a mechanical lattice with give geometrical parameters of its component has fixed structure. If we forbid any process that costs energy such as deforming springs, then the lattice cannot change form. So the band structure associated with the lattice does not change either. However, as we mentioned before, the kagome lattice has a global zero-energy twisting mode. This enables us to deform the kagome lattice in a certain way, keep it at equilibrium state all along, and study how the band structure changes accordingly (see Fig. 4.6). [2].

First we notice that a gap opens when the twisting angle goes above $22°$. This is clearly shown in the phonon spectrum in Fig. 4.7. Looking at the band structure, we see that the band associated with the twisting mode lifts up. It is this process that opens up the gap, when the minimum of this band exceeds the maximum of the acoustic bands. In the next chapter, we will see how the band gap is used in studying the vibrational modes of the kagome lattice with defects.

Second we see there are linear crossings at K point for small θ and at Γ point for $\theta = 45°$. Such linear crossings are also related to the vanishing density of states in the spectrum at $\omega/\omega_0 = 2.0$ for small θ and at $\omega/\omega_0 = 1.7$ for $\theta = 45°$.

Third we find that at both $\theta = 30°$ and $\theta = 60°$, one of the bands becomes flat. The effect of flat bands on mechanical lattices has been studied in Ref. [81].

When the lattice is untwisted, the twisting mode has zero frequency. This has to do with the fact that the straight lines of connected springs across the unit cell form states of self stress. The twisting mode is just a linear combination of all the zero modes corresponding to these states of self stress.

4.4 Symmetry of twisted kagome lattices

To better understand the influence of the twisting angle on the band structure, it is useful to study the symmetry of the lattice. The plane symmetry group of

[2] Similar work has been done in phononic material as continuous media, but so far as we know, there is no such study on the discrete lattice network.

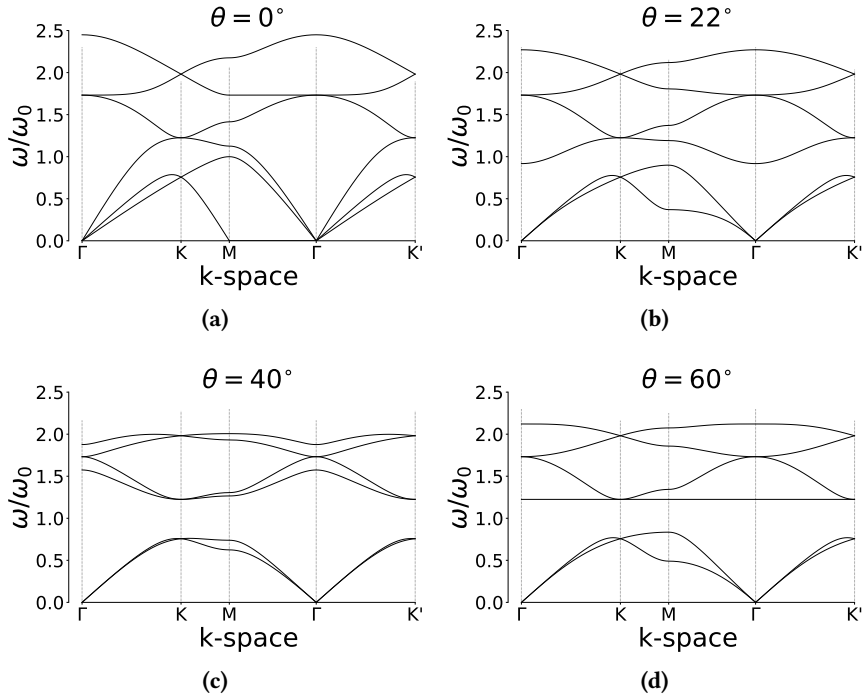

Figure 4.6. The band structure of the kagome lattice with varying twisting angle θ. The unit frequency ω_0 equals $\sqrt{k_0/m}$, where k_0 is the spring stiffness constant and m is the mass.

the twisted kagome lattice is p31m. The point group symmetry is 31m, which contains the identity, two three-fold rotation operation, and three mirror opertions (see Fig. 4.8).

Now we consider the effect of point group symmetry on the lattice vibration modes $\boldsymbol{u}(\boldsymbol{k})$. When acting upon a two-dimensional vector (x, y) in real space, the point group symmetry has the matrix representation:

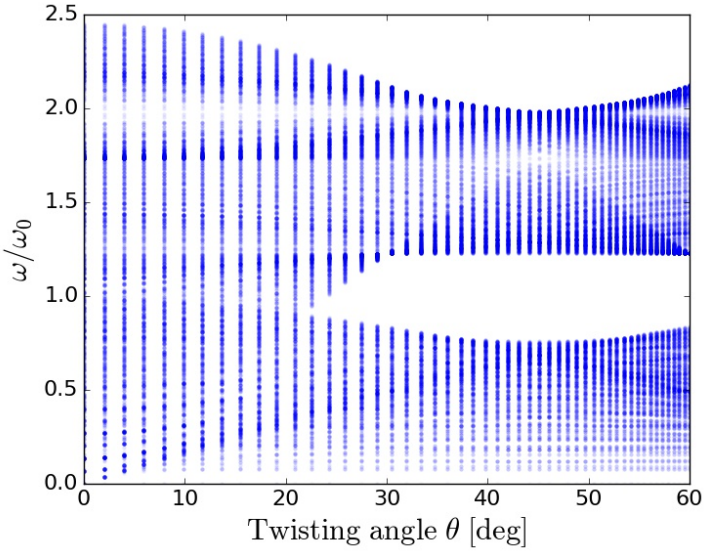

Figure 4.7. The phonon spectrum of the kagome lattice with varying twisting angle. The opacity of the data points indicates the density of states at each frequency bin. A band gap opens up at around $\theta = 22°$. The system has 20×20 unit cells with periodic boundary conditions.

$$
\begin{aligned}
R(1) &= \begin{pmatrix} 1 & 0 \\ 0 & 1 \end{pmatrix}, R(3^+) = \begin{pmatrix} -\frac{1}{2} & -\frac{\sqrt{3}}{2} \\ \frac{\sqrt{3}}{2} & -\frac{1}{2} \end{pmatrix}, \\
R(3^-) &= \begin{pmatrix} -\frac{1}{2} & \frac{\sqrt{3}}{2} \\ -\frac{\sqrt{3}}{2} & -\frac{1}{2} \end{pmatrix}, R(m_{-12}) = \begin{pmatrix} 1 & 0 \\ 0 & -1 \end{pmatrix}, \\
R(m_{2-1}) &= \begin{pmatrix} -\frac{1}{2} & \frac{\sqrt{3}}{2} \\ \frac{\sqrt{3}}{2} & \frac{1}{2} \end{pmatrix}, R(m_{11}) = \begin{pmatrix} -\frac{1}{2} & -\frac{\sqrt{3}}{2} \\ -\frac{\sqrt{3}}{2} & \frac{1}{2} \end{pmatrix}.
\end{aligned}
\tag{4.11}
$$

For the three masses in the unit cell, the point group symmetry has the representation

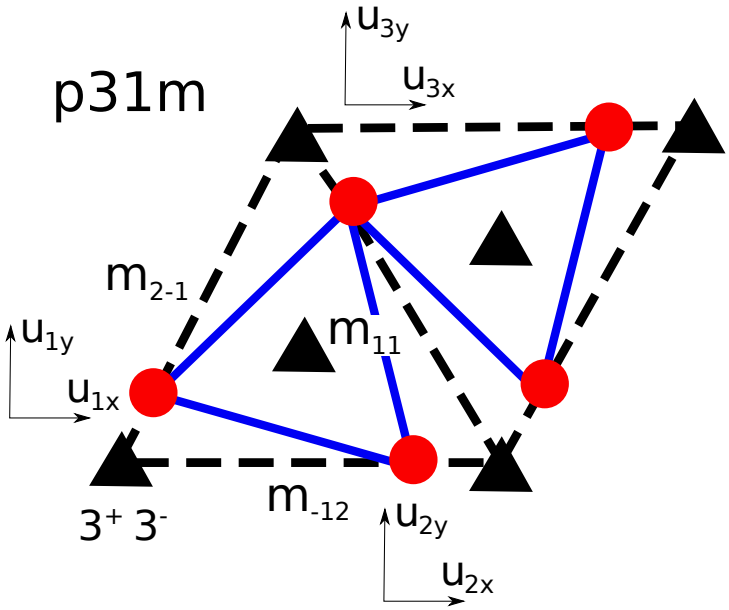

Figure 4.8. The unit cell of the twisted kagome lattice. The masses are the red dots. The bonds are the blue lines. The point group symmetries – the three-fold rotational axes and the mirrors – are labeled in black triangles and dashed lines respectively. The six components of vibrational modes – (u_{ix}, u_{iy}) for $i = 1, 2, 3$ – are also labeled near each mass.

$$
\begin{aligned}
P(1) &= \begin{pmatrix} 1 & 0 & 0 \\ 0 & 1 & 0 \\ 0 & 0 & 1 \end{pmatrix}, P(3^+) = \begin{pmatrix} 0 & 0 & 1 \\ 1 & 0 & 0 \\ 0 & 1 & 0 \end{pmatrix}, \\
P(3^-) &= \begin{pmatrix} 0 & 1 & 0 \\ 0 & 0 & 1 \\ 1 & 0 & 0 \end{pmatrix}, P(m_{-12}) = \begin{pmatrix} 0 & 0 & 1 \\ 0 & 1 & 0 \\ 1 & 0 & 0 \end{pmatrix}, \\
P(m_{2-1}) &= \begin{pmatrix} 1 & 0 & 0 \\ 0 & 0 & 1 \\ 0 & 1 & 0 \end{pmatrix}, P(m_{11}) = \begin{pmatrix} 0 & 1 & 0 \\ 1 & 0 & 0 \\ 0 & 0 & 1 \end{pmatrix}.
\end{aligned} \tag{4.12}
$$

Now the representation S of the point group symmetry on the six-dimensional vector $\boldsymbol{u}(\boldsymbol{k})$ is just the direct product of R and P

$$S(g) = R(g) \otimes P(g), \tag{4.13}$$

where g is a symmetry operation.

In general the effect of the symmetries on the dynamical matrix is

$$S(g)\boldsymbol{D}(\boldsymbol{k})S(g^{-1}) = \boldsymbol{D}(R(g)\cdot\boldsymbol{k}). \tag{4.14}$$

At high symmetry point $\boldsymbol{k}^*$ such as Γ and K, where $R(g)\cdot\boldsymbol{k}^* - \boldsymbol{k}^*$ is a reciprocal lattice vector, we find that $S(g)$ commutes with the dynamical matrix $\boldsymbol{D}(\boldsymbol{k})$

$$S(g)\boldsymbol{D}(\boldsymbol{k})S(g^{-1}) = \boldsymbol{D}(\boldsymbol{k}). \tag{4.15}$$

This explains the degeneracies at the high symmetry points observed in Fig. 4.6.

4.5 Critical twisting angle: double degeneracy

When the twist angle $\theta = 45°$, the lattice dynamics shows very special phenomena, which we will study in this section.

The first and the most obvious phenomenon is in the band structure. The six phonon bands collapse into three pairs everywhere in the Brillouin zone (see Fig. 4.9). In other words, the dynamical matrix $\boldsymbol{D}(\boldsymbol{k})$ has doubly degenerate eigenvalues everywhere in the reciprocal space. Notice that a four-band linear crossing occurs at the Γ point.

Besides the degenerate eigenvalues ω, we also investigate the eigenvectors $\boldsymbol{\epsilon}$. The second special phenomenon is that all the eigenvectors $\boldsymbol{\epsilon}(\boldsymbol{k})$ of $\boldsymbol{D}(\boldsymbol{k})$ have equal mode amplitude on each of the three masses, i.e. the norm of the vector $(\epsilon_{ix}, \epsilon_{iy})$ is identical for $i = 1, 2, 3$.

When approaching the critical twisting angle, for $\theta \to 45°$, we also find that for each pair of the almost degenerate eigenvectors $\boldsymbol{\epsilon}^a$ and $\boldsymbol{\epsilon}^b$ which are orthogonal as they are have different eigenvalues, the sub-vectors $(\epsilon^a_{ix}, \epsilon^a_{iy})$ and $(\epsilon^b_{ix}, \epsilon^b_{iy})$ are also orthogonal for $i = 1, 2, 3$, namely $\langle(\epsilon^a_{ix}, \epsilon^a_{iy}), (\epsilon^b_{ix}, \epsilon^b_{iy})\rangle = 0$.

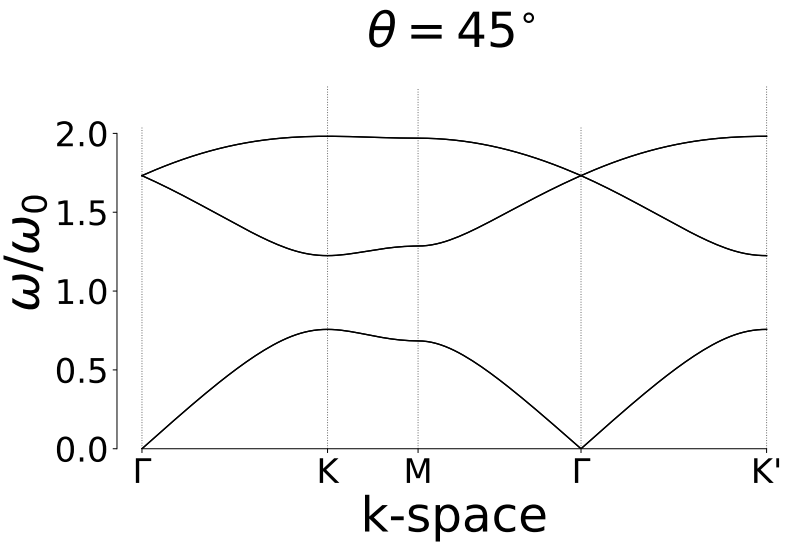

Figure 4.9. The band structure of the kagome lattice with the twisting angle $\theta = 45°$. The six bands are doubly degenerate everywhere in the reciprocal space, so only three bands can be seen in the figure. One of the finite-frequency vibrational modes at the four-band crossing at the Γ point is shown on the cover of this thesis.

All these phenomena together strongly imply that there is probably a symmetry of the dynamical matrix relating the eigenvectors in a special way. Currently we are still seeking the analytical form of this symmetry.

Mathematically, the expected symmetry operation with a matrix representation $\boldsymbol{S}$ in terms of the lattice vibration should commute with the dynamical matrix $\boldsymbol{D}(\boldsymbol{k})$ for all $\boldsymbol{k}$. This can be seen in the following. For each pair of bands, its eigenvectors $\boldsymbol{\epsilon}^a$ and $\boldsymbol{\epsilon}^b$ are related by this symmetry $\boldsymbol{S}$. Then we have

$$\boldsymbol{D}(\boldsymbol{k})\boldsymbol{S}\boldsymbol{\epsilon}^a = \boldsymbol{D}(\boldsymbol{k})\boldsymbol{\epsilon}^b = \lambda^b\boldsymbol{\epsilon}^b \tag{4.16}$$

and

$$\boldsymbol{S}\boldsymbol{D}(\boldsymbol{k})\boldsymbol{\epsilon}^a = \boldsymbol{S}\lambda^a\boldsymbol{\epsilon}^a = \lambda^a\boldsymbol{\epsilon}^b. \tag{4.17}$$

Since $\boldsymbol{D}(\boldsymbol{k})\boldsymbol{S} = \boldsymbol{S}\boldsymbol{D}(\boldsymbol{k})$, it means $\lambda^a = \lambda^b$, hence the degeneracy.

We know that $\boldsymbol{S}$ cannot simply be any point group symmetry, because the latter only commutes with $\boldsymbol{D}$ at certain high symmetry points, as we have seen in Eqn. (4.15).

Chapter 5

Defects in twisted kagome lattices: gap modes

In the previous chapter, we have studied the perfect twisted kagome lattices. In this chapter, we study the effect of defects on lattice vibrations in the framework of lattice dynamics [79, 82, 83]. As in chapter 3, we model a defect by changing the stiffness constant of one spring (Fig. 5.1).

As we shall see, such defects can induce localized and spectrally isolated modes inside the bulk band gap. We investigate such gap modes in detail for varying twisting angles. Remarkably, when several defects are present, the resulting vibrational modes can be understood in terms of the hybridization of single-defect modes. We investigate this situation through an effective tight-binding theory.

5.1 A single defect: localized gap modes

In this section we study a lattice where the stiffness of a single spring is changed from the uniform value k_0 to k. Due to the lattice symmetry, all springs in a perfect kagome lattice are equivalent, so we can modify any of them and get the same system. When a spring is removed, i.e. when $k/k_0 = 0$, the phonon spectrum is modified, going from Fig. 4.7 to Fig. 5.2.

When the twisting angle θ is low and the phonon spectrum is not gapped,

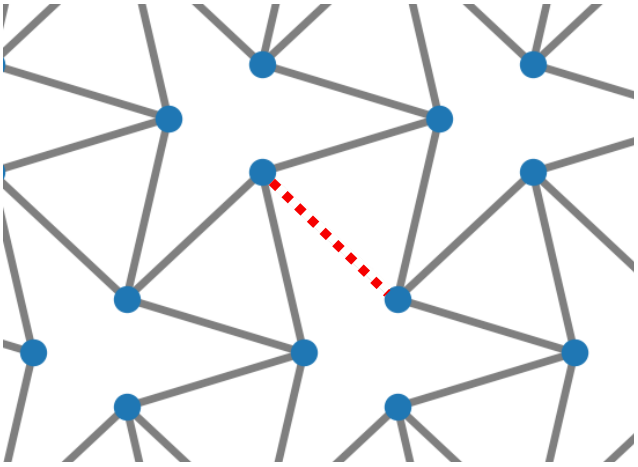

Figure 5.1. The twisted kagome lattice that has a defect of a single spring (dashed red line) whose stiffness constant k_0 is changed from the uniform value k of all other springs (solid gray lines).

there is no visible change. However, when the gap opens, for a twisting angle $\theta > 22°$, then we see that a vibrational mode appears inside the bulk band gap. Notably, this gap mode, due to the existence of the defect, is exponentially localized around the defect (see Fig. 5.3), i.e. $\phi(r) \sim e^{-r/\xi}$ where ϕ is the vibrational amplitude, r is the distance from the defect and ξ is a decay length.

The frequency of the defect mode slightly depends on the twisting angle and reaches its maximum at the critical twisting angle[1] $\theta = 45°$ (see Fig. 5.4). Interestingly, the maximum frequency $\omega/\omega_0 = 1$ is the frequency for a simple harmonic oscillator with the same spring and mass as those of the perfect kagome lattice. The underlying reason for this has yet to be understood.

The same effect can be observed when the defect spring stiffness $k/k_0 < 1$ is finite, see Fig. 5.5. When $k/k_0 > 1$, the defect mode leaves the optical band from its top. See the treatise by Maradudin [79] for the explanation of this behavior.

[1] See 4.5 for a discussion on the critical twisting angle.

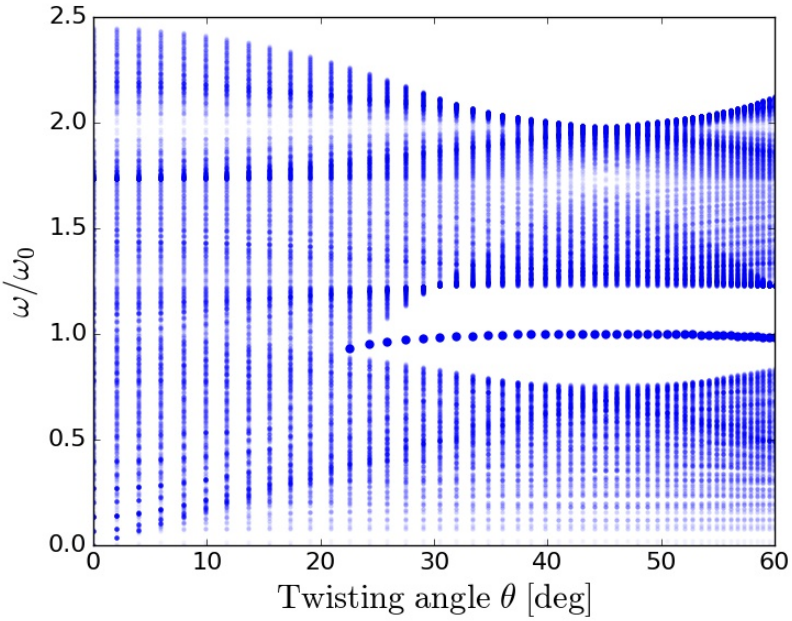

Figure 5.2. The phonon spectrum of the kagome lattice with varied twisting angle. The opacity of the data points indicates the density of states at each frequency bin. A band gap opens up at around $\theta = 22°$. The defect mode in the gap is emphasized via big solid dots. The system has 20×20 unit cells with periodic boundary conditions.

5.2 A pair of defects: the tight-binding theory

We have studied the system with a single defect. We can also consider multiple defects, and the most simple case is a pair of defects. When the two defects are far away from each other, the corresponding defect modes can be considered as single isolated defect modes, with the same frequency and mode pattern. This is because the defect modes are exponentially localized. When the defects are brought closer and closer, they hybridize, and the frequencies and mode patterns of the defect modes change. Crucially, we can understand this change through an effective tight-binding theory[2].

[2]While several combinations of pairs of defects are possible, corresponding to different removed springs in the unit cell, all of them have the same qualitative properties, and we focus

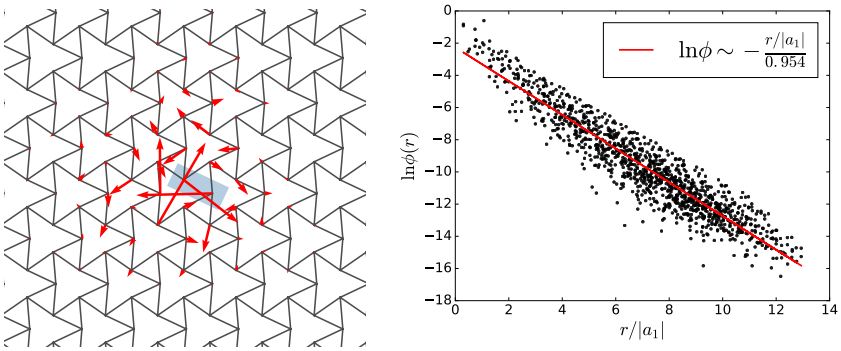

(a) **(b)**

Figure 5.3. The defect mode is localized. (**a**) The kagome lattice with one removed spring indicated in the shaded blue region. The defect mode is depicted by arrows representing the mode displacement of the masses. (**b**) The amplitude of the mode displacement decays exponentially with the normalized distance $r/|a_1|$ from the defect, where a_1 is a lattice vector in Eq. 4.2. Here we find the decay length $\xi/|a_1| = 0.954$. The twisting angle is $\theta = 34.7°$, and the system has 20×20 unit cells with periodic boundary conditions.

When only one defect is present, there is a single-defect mode ϕ with frequency ω_s. Let us now consider a lattice with two defects located respectively at the x_1th and the x_2th unit cell along the same horizontal line and separated by a distance $d = |x_1 - x_2|$ (see Fig. 5.6).

The dynamical matrix of the lattice $\boldsymbol{D}$ has two gap modes, which we denote as ψ_+ and ψ_-. By definition, we have

$$\boldsymbol{D}\psi_\pm = \omega_\pm^2 \psi_\pm, \tag{5.1}$$

where $\omega_\pm^2$ is the square of the gap-mode frequencies. ϕ's and ψ's are assumed to be normalized.

Following the principle of tight-binding models[3], we try to express ψ as a linear combination of the two single-defect modes ϕ_1 and ϕ_2, where $\phi_{1(2)}$

on only one of them.

[3]It is also known as the Hückel model or Linear Combination of Atomic Orbitals (LCAO) approximation in the context of quantum chemistry.

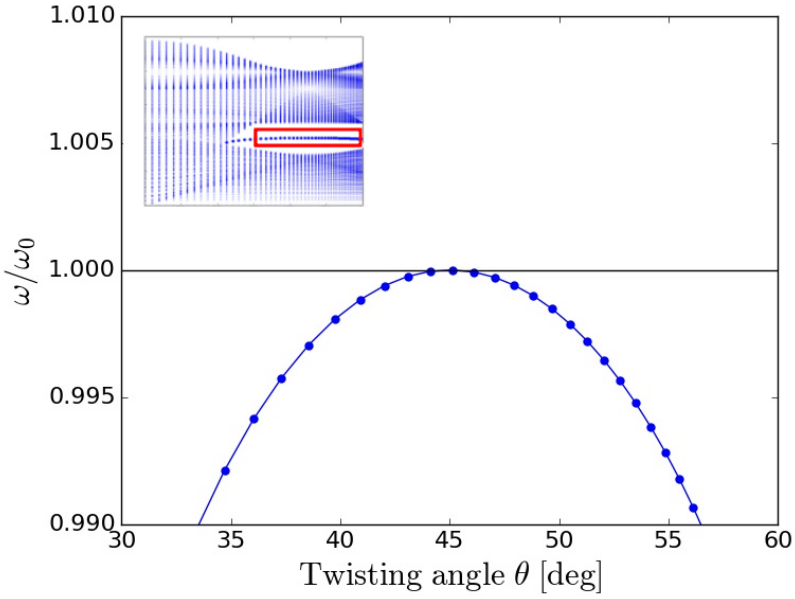

Figure 5.4. Zoom of Fig. 5.2. The gap mode that has its maximum frequency of $\omega/\omega_0 = 1$ at $\theta = 45°$.

corresponds to the single defect located at $x_{1(2)}$ (See Fig. 5.7). To do so, let us write

$$\psi_{\text{TB}} = c_1\phi_1 + c_2\phi_2, \tag{5.2}$$

where c_1 and c_2 are scalar constants. Multiplying both sides of Eq. 5.1 by ϕ_1 and ϕ_2 respectively, we get

$$c_1\langle\phi_1, \boldsymbol{D}\phi_1\rangle + c_2\langle\phi_1, \boldsymbol{D}\phi_2\rangle = \omega_{\text{TB}}^2(c_1\langle\phi_1, \phi_1\rangle + c_2\langle\phi_1, \phi_2\rangle) \tag{5.3}$$

$$c_1\langle\phi_2, \boldsymbol{D}\phi_1\rangle + c_2\langle\phi_2, \boldsymbol{D}\phi_2\rangle = \omega_{\text{TB}}^2(c_1\langle\phi_2, \phi_1\rangle + c_2\langle\phi_2, \phi_2\rangle) \tag{5.4}$$

or in the matrix form:

$$\begin{pmatrix} \alpha & \beta \\ \beta & \alpha \end{pmatrix} \begin{pmatrix} c_1 \\ c_2 \end{pmatrix} = \omega_{\text{TB}}^2 \begin{pmatrix} 1 & S \\ S & 1 \end{pmatrix} \begin{pmatrix} c_1 \\ c_2 \end{pmatrix} \tag{5.5}$$

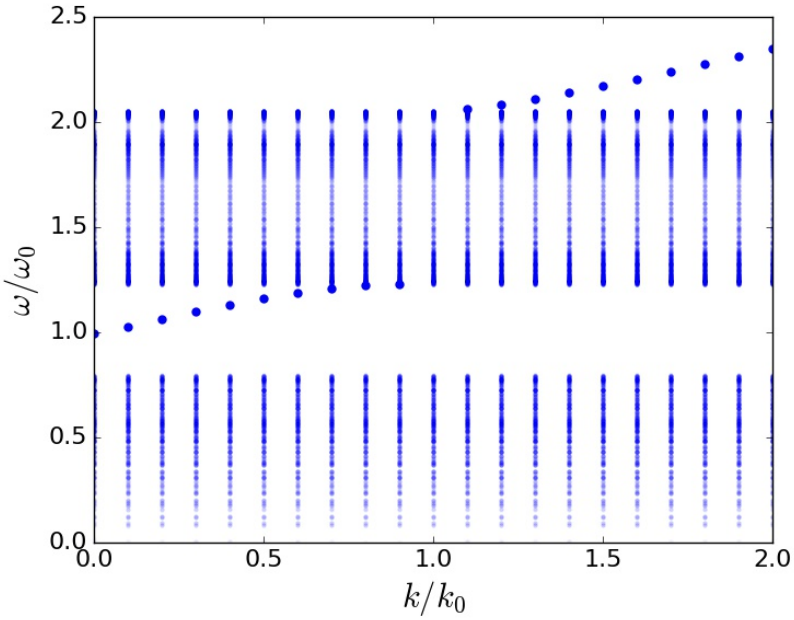

Figure 5.5. The spectrum with varying spring stiffness k. k_0 is the stiffness of the spring stiffness in perfect lattices. The system parameters are the same as Fig. 5.3.

where we defined $\alpha = \langle \phi_1, \boldsymbol{D}\phi_1 \rangle = \langle \phi_2, \boldsymbol{D}\phi_2 \rangle$, $\beta = \langle \phi_1, \boldsymbol{D}\phi_2 \rangle = \langle \phi_2, \boldsymbol{D}\phi_1 \rangle$ as $\boldsymbol{D}$ is hermitian, and the overlap integral $S = \langle \phi_2, \phi_1 \rangle$. The solution to the above eigenvalue problem is:

$$\omega^2_{+\mathrm{TB}} = \frac{\alpha + \beta}{1 + S}, \quad \omega^2_{-\mathrm{TB}} = \frac{\alpha - \beta}{1 - S}. \tag{5.6}$$

When the defects are far away from each other, i.e. $d \gg \xi$, both the overlap integral S and the matrix element β vanish as ϕ_1 and ϕ_2 are localized. In this case,

$$\omega^2_{+\mathrm{TB}} = \omega^2_{-\mathrm{TB}} = \alpha = \omega^2_s, \tag{5.7}$$

that is to say, the frequencies of both gap modes equal the single-defect gap mode frequency.

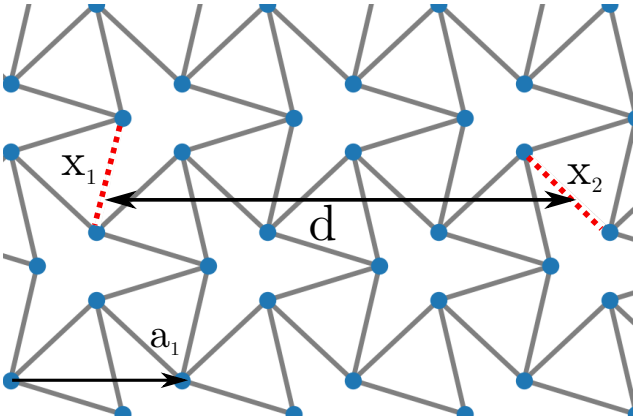

Figure 5.6. The twisted kagome lattice that has two defects located respectively at the x_1 and x_2 along the same horizontal line and separated by a distance $d = |x_1 - x_2|$. a_1 is a lattice vector.

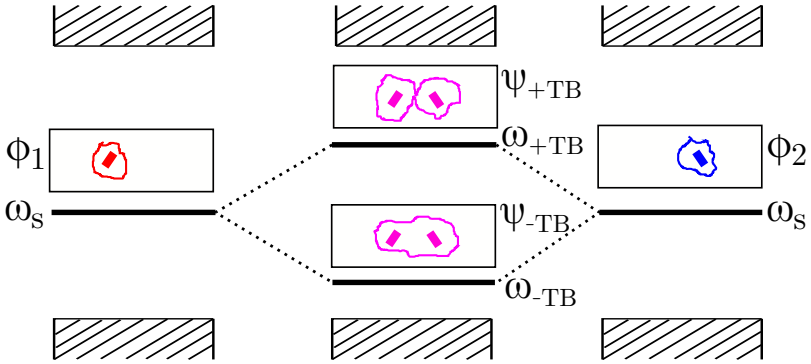

Figure 5.7. The scheme of tight-binding models for gap modes.

In Fig. 5.8, we compare this result with the values directly obtained from the diagonalization of $\boldsymbol{D}$. We see that the tight-binding theory predicts the hybridization frequency level quite well, even though it only keeps track of only two degrees of freedom ϕ_1 and ϕ_2. The reason why the theory works so well is because the defect modes lie in the band gap and therefore are spectrally isolated from the other vibrational modes. Notice there is a small discrepancy

between the tight-binding prediction and the direct diagonalization values.

We also compute the eigenvectors ψ_- and plot them in Fig. 5.9.

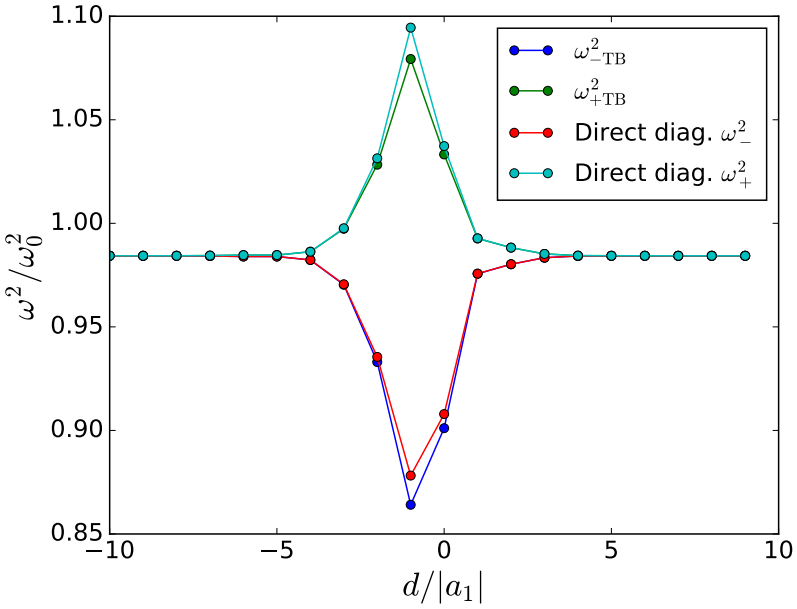

Figure 5.8. A comparison of the squared frequencies between the tight-binding theory and the direct diagonalization of the dynamical matrix. The defects are separated by a distance d. The system parameters are the same as Fig. 5.3.

5.3 Towards multiple defects

For a system with multiple defects, we raise two specific questions about the gap modes. While we do not include the results of these investigations in this thesis, it is worth pointing out the directions.

First, since the tight binding theory works for a pair of defects, we can wonder whether there is a hybridization of gap modes of multiple defects, just like the formation of a molecule out of multiple atoms via chemical bonds.

Second, for a perfect system, the band gap in the spectrum forbids signals to propagate. But the gap mode associated with each defect can help

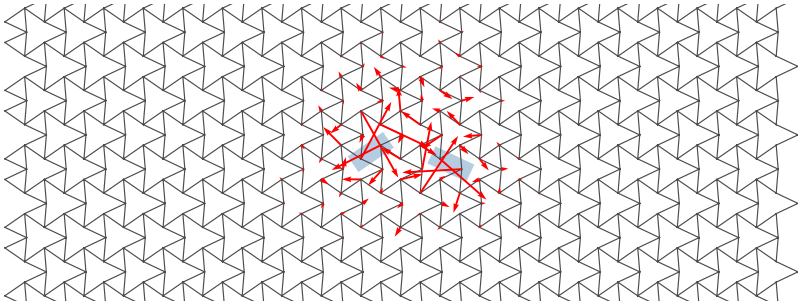

(a)

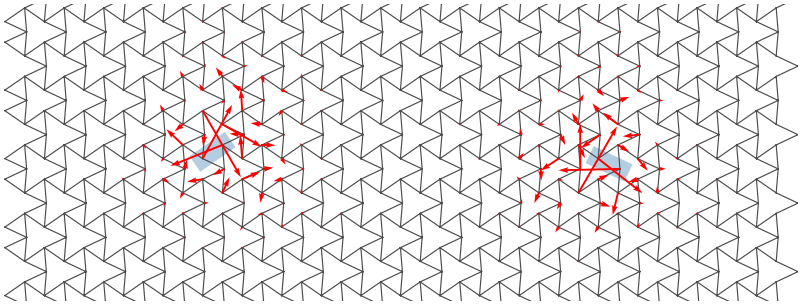

(b)

Figure 5.9. Lowest frequency gap modes ψ_- for **(a)** $d/|a_1| = 2$ and **(b)** $d/|a_1| = 10$. The shaded blue regions indicate the defects of removed springs. The system parameters are the same as Fig. 5.3.

mediate the forbidden signal. As we keep introducing defects into the system, there is presumably a percolation phenomenon in terms of the mechanical signal at the band-gap frequencies. The same concepts have been realized and investigated in the systems of continuum media like photonic [84] and phononic crystals [85], but never in the discrete mechanical lattice systems to the knowledge of the author.

Chapter 6

Elastic waves in flexible strings

In this chapter we study the elastic waves induced by an abrupt impact at a point. The impact has a constant velocity, and the string is initially straight and tensionless.

6.1 Introduction

The theory of flexible strings has been intensively developed in classic studies by Navier, Poisson, Stokes, Rayleigh and Kelvin, to name but a few [86]. The conceptual success of this classical field theory not only provides the general principle for the description of the mechanical behavior of strings, but also makes it possible to perform rational analysis in many physics and engineering problems [87–96]. Typically the linear theory only considers infinitesimal displacements and omits the coupling between transverse and longitudinal displacements. This approximation is, however, no longer accurate when the effect of nonlinearities becomes dominant, e.g., when the motion of the string has a large amplitude. Such studies of nonlinear dynamics of elastic waves in flexible strings are motivated by engineering challenges such as the deformation of yarns in weaving machines, the strength of ropes of parachutes or cables in mechanical structures like cranes and bridges [97–100].

In this chapter, we consider the case of a flexible string which is initially straight and tensionless. In this case, no linear transverse waves propagate. In general, such media are said to be in "sonic vacuum"[101], meaning that the velocity of linear waves vanishes. As a consequence, any small disturbance will generate a strongly nonlinear effect and dominate the dynamics. We consider a constant impact velocity, in which case nonlinear shock waves are generated. We study the nonlinear dynamics and obtain the shock velocity which scales with the impact velocity to a fractional exponent. This result has been obtained in literature as a special case [93, 102], but our interpretation articulates its mechanism, which hopefully can help explain similar types of shear shocks in mechanical models for solids in higher dimensions. Furthermore, we perform simulations that demonstrate this phenomenon in a simple model of wide applicability.

6.2 Lattice model and simulation

We start by considering the classical model of the 1D lattice of identical masses m confined in a plane (see Fig. 6.1a). The masses are coupled with their nearest neighbours by identical Hookean springs with the spring constant k and the rest length a. In linear theory the model supports elastic waves along both the longitudinal and the transverse direction and the two waves are decoupled. In the long-wave limit, the velocity of linear transverse waves is [103]

$$v_h = \sqrt{\tau/\rho}. \tag{6.1}$$

where τ is the constant tension in the springs and ρ the linear density. The nonlinear effect of the infinitesimal perturbation of longitudinal and transverse waves on τ is omitted. For the special case in which the spring rest length equals the equilibrium lattice spacing, τ goes to 0. In this case, the linear transverse wave has a vanishing speed and the effect of nonlinearities becomes dominant.

The perturbation that we choose to study in this chapter is an abrupt impact upon the mass at origin with constant velocity v_E along the transverse direction at time 0. This impact will generate a longitudinal front with velocity

$$v_l = a\sqrt{k/m} \tag{6.2}$$

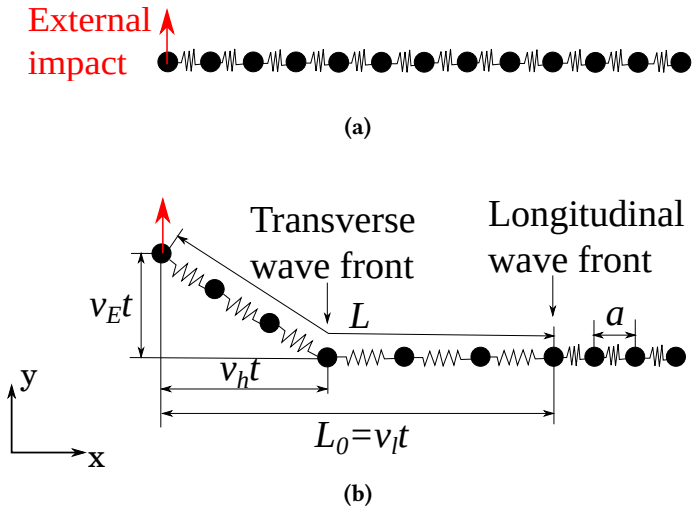

Figure 6.1. (**a**) The 1D lattice model within a plane, subject to an abrupt transverse impact of constant velocity v_E at time 0. (**b**) The impact results in two shocks: a transverse shock of speed v_h and a longitudinal shock of speed v_l. The lattice has the shape of a kink at the transverse shock.

as well as a nonlinear transverse shock whose velocity v_h is what we aim to derive. Because v_h is zero to linear order, we assume that the actual v_h is also smaller than v_l when the external impact $v_E \ll v_l$. In other words, the impact generates a fast longitudinal stress wave as well as a slow transverse displacement wave. The abrupt stimulus causes abrupt responses, i.e., the deformed structure takes the shape of a kink. This kink is a sharp transition in the direction of the spatial arrangement of the masses, which happens right at the transverse wave front. [1]

Now let us relate the shape and the propagation speed of the kink. We make use of the result that transverse waves do not influence longitudinal strain [93, 96–98]. In other words, the spring tensions in front of and behind the kink are the same. This suggests that transverse shocks propagate due to the tension induced by the longitudinal shock. We assume that behind

[1] The longitudinal wave also has a sharp wave front, but since the displacement is along the same direction of propagation there is no change of shape.

the longitudinal shock, all of the springs experience approximately the same tension. From Eq. (6.1), this implies that v_h is also nonzero and constant. This in turn suggests that the kink shape consists of two rectilinear parts, as shown in Fig. 6.1b.

Next, we derive v_h. At time t, the longitudinal wave propagates a distance of $L_0 = v_l t$. The number of springs in this region is L_0/a. The contour length of the lattice behind the front of longitudinal wave is L. Then, the uniform tension along the contour is

$$\tau = \frac{k(L - L_0)}{L_0/a}. \tag{6.3}$$

The mass at the origin subject to the impact moves a distance $v_E t$ in the y-direction and the transverse shock propagates a distance $v_h t$ in the x-direction. Using the geometry of the configuration, we find

$$L = \sqrt{(v_E t)^2 + (v_h t)^2} + L_0 - v_h t. \tag{6.4}$$

Combining Eq. (6.4) and Eq. (6.3), we find

$$\tau = ka\left(\sqrt{\left(\frac{v_E}{v_l}\right)^2 + \left(\frac{v_h}{v_l}\right)^2} - \frac{v_h}{v_l}\right). \tag{6.5}$$

Furthermore, combining Eq. (6.1), Eq. (6.2), Eq. (6.5) and using $\rho = m/a$, we obtain the desired relation

$$\left(\frac{v_E}{v_l}\right)^2 = \left(\frac{v_h}{v_l}\right)^4 + 2\left(\frac{v_h}{v_l}\right)^3. \tag{6.6}$$

If the external impact velocity v_E vanishes, v_h vanishes as well. Then, the last term in Eq. (6.6) dominates the right-hand side. Thus, we obtain the result

$$\frac{v_h}{v_l} = \frac{1}{2^{1/3}}\left(\frac{v_E}{v_l}\right)^{2/3}. \tag{6.7}$$

This power-law relation between v_E and v_h with a fractional exponent is a remarkable result of nonlinear dependence. This result has been obtained in Ref. [93, 102], and supported by experimental data [104].

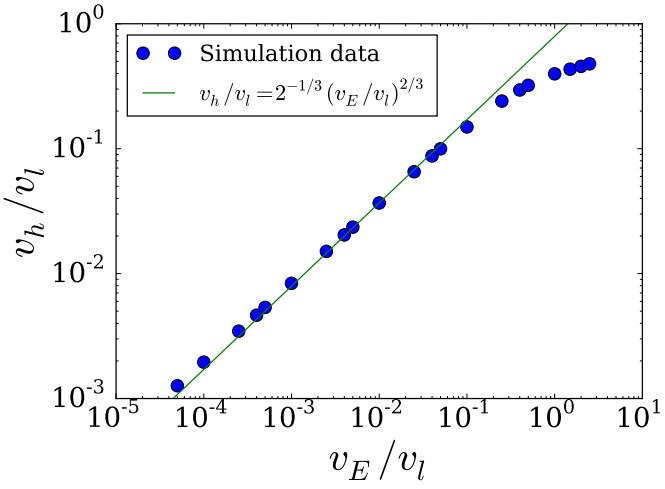

Figure 6.2. The velocity of the nonlinear transverse wave v_h vs the impact velocity v_E, with both velocities rescaled by the speed of sound v_l.

To check the relation (6.7) numerically, we performed Newtonian dynamics simulations on the lattice model to confirm the theoretical result, see Fig. 6.2. The theory fits well for small v_E. At higher ratios v_E/v_l the effect of higher-order nonlinearities cause deviations from this power law.

6.3 Continuum theory

In this section we derive v_h in the rectilinear flexible string – the continuum counterpart of the 1D lattice. We obtain the equations of motion and analyse them directly. Let l and h be the continuum fields of the longitudinal and transverse displacements and x the Lagrangian coordinate along the string. From the geometry shown in Fig. 6.3, we obtain the strain $\frac{\partial s}{\partial x}$, which to the lowest order is given by:

$$\frac{\partial s}{\partial x} = \frac{\partial l}{\partial x} + \frac{1}{2}\left(\frac{\partial h}{\partial x}\right)^2. \tag{6.8}$$

The flexible string has only stretching potential energy $V = \frac{\kappa}{2}(\frac{\partial s}{\partial x})^2$ is quadratic in $\frac{\partial s}{\partial x}$. Using this, we write down the Lagrangian density

$$\mathcal{L} = \frac{1}{2}\rho\left(\dot{h}^2 + \dot{l}^2\right) - \frac{\kappa}{2}\left(\frac{\partial l}{\partial x} + \frac{1}{2}\left[\frac{\partial h}{\partial x}\right]^2\right)^2 \tag{6.9}$$

where κ is the elastic modulus of the string. The Euler-Lagrange equations are

$$\rho\ddot{l} - \kappa\frac{\partial}{\partial x}\left(\frac{\partial l}{\partial x} + \frac{1}{2}\left[\frac{\partial h}{\partial x}\right]^2\right) = 0, \tag{6.10}$$

$$\rho\ddot{h} - \kappa\frac{\partial}{\partial x}\left\{\left(\frac{\partial l}{\partial x} + \frac{1}{2}\left[\frac{\partial h}{\partial x}\right]^2\right)\frac{\partial h}{\partial x}\right\} = 0. \tag{6.11}$$

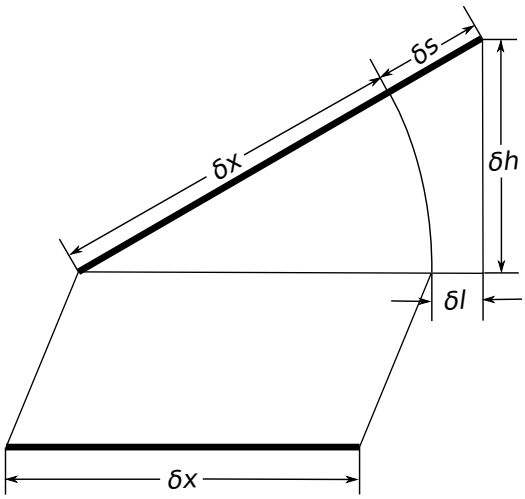

Figure 6.3. An infinitesimal element δx (thick line) subject to longitudinal and transverse displacements. This geometry lets us calculate $\frac{\partial s}{\partial x}$ in terms of $\frac{\partial l}{\partial x}$ and $\frac{\partial h}{\partial x}$, Eq. (6.8).

The external impact acts on the string transversely with constant velocity v_E at the origin starting at time 0. Eq. (6.10) is a linear wave equation for the longitudinal wave with a "source" term of second order in the transverse field

h. We seek steady-state solutions in which the displacement fields change at constant speed, i.e., $\ddot{l} = 0$ and $\ddot{h} = 0$. The condition $\ddot{l} = 0$ together with Eq. (6.10) requires that the tension $\frac{\partial l}{\partial x} + \frac{1}{2}\left(\frac{\partial h}{\partial x}\right)^2$ should be constant elsewhere except for the longitudinal wave front where there is a sharp jump of l. Then, Eq. (6.11) turns into the form of the linear wave equation in the tensioned region behind the longitudinal wave front:

$$\rho\ddot{h} - \kappa\frac{\partial s}{\partial x}\frac{\partial^2 h}{\partial x^2} = 0, \text{for } x < v_l t. \tag{6.12}$$

To obtain the tension $\frac{\partial s}{\partial x}$, we integrate the strain at time t along the string and use the boundary conditions to get the total deformation of the string in the tensioned region $[0, v_l t]$. The strain is this deformation divided by $v_l t$.

The boundary conditions of l are $l(x = 0, t) = 0$ and $l(x = v_l t, t) = 0$. The boundary conditions of h at the origin are $\dot{h}(x = 0, t) = v_E$ and $h(x = 0, t) = v_E t$. Because v_h is smaller than v_l, the boundary condition of h at the longitudinal wave front is $h(x = v_l t, t) = 0$. In addition, we assume that h has a traveling-wave solution of the form $h(x - v_h t)$, so $\frac{\partial h}{\partial x} = -\frac{1}{v_h}\frac{\partial h}{\partial t}$, and the steady-state solution requires $\frac{\partial^2 h}{\partial x^2} = \frac{1}{v_h^2}\frac{\partial^2 h}{\partial t^2} = 0$.

The total deformation along the string at time t is equal to the integral of the strain:

$$\int_0^{v_l t} \frac{\partial l}{\partial x} + \frac{1}{2}\left(\frac{\partial h}{\partial x}\right)^2 \mathrm{d}x \tag{6.13}$$

$$= l\Big|_{x=0}^{v_l t} + \frac{1}{2}h\frac{\partial h}{\partial x}\Big|_{x=0}^{v_l t} - \int_0^{v_l t} \frac{1}{2}h\frac{\partial^2 h}{\partial x^2}\mathrm{d}x \tag{6.14}$$

$$= -\frac{1}{2}h\frac{\partial h}{\partial x}\Big|_{x=0} \tag{6.15}$$

$$= \frac{v_E^2 t}{2v_h}. \tag{6.16}$$

Therefore, the strain is

$$\frac{\partial s}{\partial x} = \frac{v_E^2 t}{2v_h}/(v_l t) = \frac{v_E^2}{2v_h v_l}. \tag{6.17}$$

In addition, the linear transverse-wave equation Eq. (6.12), with traveling-wave solution $h(x - v_h t)$, gives

$$\rho v_h^2 - \kappa \frac{\partial s}{\partial x} = 0. \tag{6.18}$$

From Eq. (6.17) and (6.18), we obtain

$$\frac{v_h}{v_l} = \frac{1}{2^{1/3}} \left(\frac{v_E}{v_l} \right)^{2/3}. \tag{6.19}$$

In principle, the method used in this section provides insight into the governing differential equations of the string dynamics.

6.4 Outlook

In this chapter, we have demonstrated the propagation mechanism of the transverse shock waves in a tensionless flexible string under a constant impact. One may expect to discover nonlinear waves of the same nature in many classical mechanical models for solids, e.g., marginally-rigid random spring networks [105] and some isostatic lattice networks like kagome. For untwisted kagome lattices, the shear moduli vanish along special directions, along which there are zero-frequency transverse modes of all wave numbers across the Brillouin zone [53]. This situation is analogous to a tensionless string, where even infinitesimal perturbations will generate nonlinear responses. But for such two-dimensional lattices with more complex unit cells, the coupling between degrees of freedom in transverse and longitudinal directions will not be as simple as that in strings. Besides, we have only studied the response of a string to a perturbation of a constant impact at a single point. So, extending the analysis from this chapter to general cases will require further investigations.

Moreover, for some inhomogeneous structures in toplogical mechanical lattices, e.g., dislocations [13], and interfaces between different phases [25], there are topological zero modes associated. How do these zero modes behave in the context of nonlinear motions? Do any of them also propagate in forms of solitons like vortices or skyrmions, as high-dimensional counterpart of kinks in topological rotor chains. If so, how does the boundary condition influence

the behavior of such nonlinear objects. Or do they all remain localized and oscillate with large amplitudes? These are the open questions that we hope to get answers in future works.

Bibliography

[1] D. L. Goodstein, *States of matter* (Dover Publications, 1985).

[2] M. Kadic, T. Bückmann, R. Schittny, and M. Wegener, Reports on Progress in Physics **76**, 126501 (2013).

[3] Z. G. Nicolaou and A. E. Motter, Nature materials **11**, 608 (2012).

[4] M. Schenk and S. D. Guest, Proceedings of the National Academy of Sciences **110**, 3276 (2013).

[5] H. Yasuda and J. Yang, Physical review letters **114**, 185502 (2015).

[6] R. Gatt, L. Mizzi, J. I. Azzopardi, K. M. Azzopardi, D. Attard, A. Casha, J. Briffa, and J. N. Grima, Scientific reports **5**, srep08395 (2015).

[7] S. Babaee, J. Shim, J. C. Weaver, E. R. Chen, N. Patel, and K. Bertoldi, Advanced Materials **25**, 5044 (2013).

[8] J. Liu, T. Gu, S. Shan, S. H. Kang, J. C. Weaver, and K. Bertoldi, Advanced Materials **28**, 6619 (2016).

[9] C. Lv, D. Krishnaraju, G. Konjevod, H. Yu, and H. Jiang, Scientific reports **4** (2014).

[10] E. T. Filipov, T. Tachi, and G. H. Paulino, Proceedings of the National Academy of Sciences **112**, 12321 (2015).

[11] C. Coulais, E. Teomy, K. de Reus, Y. Shokef, and M. van Hecke, Nature **535**, 529 (2016).

[12] J. T. B. Overvelde, T. A. De Jong, Y. Shevchenko, S. A. Becerra, G. M. Whitesides, J. C. Weaver, C. Hoberman, and K. Bertoldi, Nature communications **7** (2016).

[13] J. Paulose, B. G.-g. Chen, and V. Vitelli, Nature Physics **11**, 153 (2015).

[14] J. Paulose, A. S. Meeussen, and V. Vitelli, Proceedings of the National Academy of Sciences of the United States of America **112**, 7639 (2015).

[15] L. Pauling, *The nature of the chemical bond and the structure of molecules and crystals: an introduction to modern structural chemistry*, Vol. 18 (Cornell university press, 1960).

[16] S. A. Cummer, J. Christensen, and A. Alù, Nature Reviews Materials **1**, 16001 (2016).

[17] R. Süsstrunk and S. D. Huber, Science **349**, 47 LP (2015).

[18] B. G.-g. Chen, N. Upadhyaya, and V. Vitelli, Proceedings of the National Academy of Sciences of the United States of America **111**, 8 (2014), arXiv:1404.2263 .

[19] V. Vitelli, N. Upadhyaya, and B. G.-g. Chen, arXiv:1407.2890 .

[20] Y. Zhou, B. G.-g. Chen, N. Upadhyaya, and V. Vitelli, Physical Review E **95**, 022202 (2017).

[21] B. Florijn, C. Coulais, and M. van Hecke, Physical Review Letters **113**, 175503 (2014).

[22] J. Christensen, M. Kadic, O. Kraft, and M. Wegener, Mrs Communications **5**, 453 (2015).

[23] N. Engheta, R. W. Ziolkowski, and Institute of Electrical and Electronics Engineers., *Metamaterials : physics and engineering explorations* (Wiley-Interscience, 2006) p. 414.

[24] P.-G. de Gennes, *Twentieth century physics*, edited by L. Brown, B. Pippard, and A. Pais (CRC Press, 1995) Chap. 21.

[25] C. L. Kane and T. C. Lubensky, Nature Physics **10**, 39 (2013).

[26] T. C. Lubensky, C. L. Kane, X. Mao, A. Souslov, and K. Sun, Reports on Progress in Physics **78**, 73901 (2015), arXiv:1503.01324 .

[27] T. Tarnai and A. Lengyel, Journal of Mechanics of Materials and Structures **6**, 591 (2011).

[28] D. Z. Rocklin, New Journal of Physics **19**, 65004 (2017).

[29] Y.-T. Wang, P.-G. Luan, and S. Zhang, New Journal of Physics **17**, 073031 (2015).

[30] P. Wang, L. Lu, and K. Bertoldi, Physical review letters **115**, 104302 (2015).

[31] S. H. Mousavi, A. B. Khanikaev, Z. Wang, M. R. Haberman, and A. Alù, Nature Communications **6**, 8682 (2015).

[32] A. B. Khanikaev, R. Fleury, S. H. Mousavi, A. Alù, and A. Alù, Nature Communications **6**, 8260 (2015).

[33] L. M. Nash, D. Kleckner, A. Read, V. Vitelli, A. M. Turner, and W. T. M. Irvine, Proceedings of the National Academy of Sciences of the United States of America **112**, 14495 (2015).

[34] Z. Yang, F. Gao, X. Shi, X. Lin, Z. Gao, Y. Chong, and B. Zhang, Physical Review Letters **114**, 114301 (2015).

[35] Z. Yang, F. Gao, and B. Zhang, Scientific Reports **6**, 29202 (2016).

[36] M. Xiao, W.-J. Chen, W.-Y. He, and C. T. Chan, Nature Physics **11**, 920 (2015).

[37] V. Peano, C. Brendel, M. Schmidt, and F. Marquardt, Physical Review X **5**, 31011 (2015).

[38] T. Kariyado and Y. Hatsugai, Scientific Reports **5**, 18107 (2015).

[39] P. A. Deymier, K. Runge, N. Swinteck, and K. Muralidharan, Comptes Rendus M{é}canique **1**, 1 (2015).

[40] R. Bi and Z. Wang, Physical Review B **92**, 241109 (2015).

[41] H. C. Po, Y. Bahri, and A. Vishwanath, Physical Review B **93**, 205158 (2016).

[42] M. J. Lawler, Physical Review B **94**, 165101 (2016).

[43] V. Vitelli, Proceedings of the National Academy of Sciences of the United States of America **109**, 12266 (2012).

[44] A. S. Meeussen, J. Paulose, and V. Vitelli, Physical Review X **6**, 041029 (2016).

[45] B. G.-g. Chen, B. Liu, A. A. Evans, J. Paulose, I. Cohen, V. Vitelli, and C. Santangelo, Physical Review Letters **116**, 135501 (2016).

[46] D. Z. Rocklin, B. G.-G. Chen, M. Falk, V. Vitelli, and T. C. Lubensky, Physical review letters **116**, 135503 (2016).

[47] R. Süsstrunk and S. D. Huber, Proceedings of the National Academy of Sciences **113**, E4767 (2016).

[48] J. C. Y. Teo and C. L. Kane, Physical Review B **82**, 115120 (2010).

[49] C.-K. Chiu, J. C. Teo, A. P. Schnyder, and S. Ryu, Reviews of Modern Physics **88**, 35005 (2016).

[50] N. Manton and P. Sutcliffe, *Topological Solitons* (Cambridge University Press, 2004).

[51] P. G. Kevrekidis, IMA Journal of Applied Mathematics **76**, 389 (2011).

[52] M. Dunajski and T. Physics, , 0 (2012).

[53] K. Sun, A. Souslov, X. Mao, and T. C. Lubensky, Proceedings of the National Academy of Sciences of the United States of America **109**, 12369 (2012).

[54] M. Z. Hasan and C. L. Kane, Reviews of Modern Physics **82**, 3045 (2010).

[55] E. Prodan and C. Prodan, Physical Review Letters **103**, 248101 (2009).

[56] N. Berg, K. Joel, M. Koolyk, and E. Prodan, Physical Review E **83**, 21913 (2011).

[57] J. C. Maxwell, Philosophical Magazine Series 4 **27**, 294 (1864).

[58] C. R. Calladine, International Journal of Solids and Structures **14**, 161 (1978).

[59] S. Guest, International Journal of Solids and Structures **43**, 842 (2006).

[60] J. A. Combs and S. Yip, Physical Review B **28**, 6873 (1983).

[61] O. M. Braun and Y. S. Kivshar, Physics Reports **306**, 1 (1998).

[62] I. Roy, S. V. Dmitriev, P. G. Kevrekidis, and A. Saxena, Phys. Rev. E **76**, 26601 (2007).

[63] D. K. Campbell, J. F. Schonfeld, and C. A. Wingate, Physica D: Nonlinear Phenomena **9**, 1 (1983).

[64] V. G. Makhankov, *Soliton Phenomenology* (Springer Netherlands, 1990).

[65] Y. S. Kivshar, D. E. Pelinovsky, T. Cretegny, and M. Peyrard, Physical Review Letters **80**, 5032 (1998).

[66] T. Fraggis, S. Pnevmatikos, and E. N. Economou, Physics Letters A **142**, 361 (1989).

[67] Z. Fei, Y. S. Kivshar, and L. Vázquez, Phys. Rev. A **46**, 5214 (1992).

[68] R. Sasaki, *THE COMPLETE JAPANESE BASKET MAKING* (Seibundo Shinkosha, Tokyo, 2013).

[69] M. Mekata, Physics Today **56**, 12 (2003).

[70] Z. Hiroi, H. Tsunetsugu, and H. Kawamura, Journal of Physics: Condensed Matter **19**, 140301 (2007).

[71] A. S. Phani, AIP Advances **1**, 41602 (2011).

[72] X. Mao and T. C. Lubensky, Physical Review E **83**, 11111 (2011).

[73] L. Zhang, J. Ren, J.-S. Wang, and B. Li, Journal of physics. Condensed matter : an Institute of Physics journal **23**, 305402 (2011).

[74] S. Guest and J. W. Hutchinson, Journal of the Mechanics and Physics of Solids **51**, 383 (2003).

[75] R. G. Hutchinson and N. A. Fleck, Journal of the Mechanics and Physics of Solids **54**, 756 (2006).

[76] V. Kapko, M. M. J. Treacy, M. F. Thorpe, and S. D. Guest, Proceedings of the Royal Society of London A: Mathematical, Physical and Engineering Sciences (2009).

[77] A. Souslov, A. J. Liu, and T. C. Lubensky, Physical Review Letters **103**, 205503 (2009).

[78] M. T. Dove, *Introduction to Lattice Dynamics* (1993).

[79] A. A. Maradudin, E. W. Montroll, G. H. Weiss, and I. P. Ipatova, *Theory of lattice dynamics in the harmonic approximation* (London, Academic Press., 1971).

[80] N. W. Ashcroft and N. D. Mermin, *Solid state physics* (Holt, Rinehart and Winston, New York, 1976).

[81] N. Perchikov and O. V. Gendelman, (2017), arXiv:1705.07376 .

[82] E. W. Montroll and R. B. Potts, "Effect of Defects on Lattice Vibrations," (1955).

[83] J. Eshelby, Solid State Physics **3**, 79 (1956).

[84] M. Bayindir, B. Temelkuran, and E. Ozbay, Physical Review Letters **84**, 2140 (2000).

[85] F. Lemoult, N. Kaina, M. Fink, and G. Lerosey, Nature Physics **9**, 55 (2012).

[86] P. M. P. M. Morse and K. U. Ingard, *Theoretical acoustics* (Princeton University Press, 1986) p. 927.

[87] G. F. Carrier, Quarterly of Applied Mathematics **3**, 157 (1945).

[88] J. C. Smith, F. L. McCrackin, and H. F. Schiefer, Textile Research Journal **28**, 288 (1958).

[89] J. B. Keller, American Journal of Physics **27**, 584 (1959).

[90] D. W. Oplinger, The Journal of the Acoustical Society of America **32**, 1529 (1960).

[91] N. Cristescu, Journal of the Mechanics and Physics of Solids **9**, 165 (1961).

[92] H. Kolsky, Journal of Sound and Vibration **1**, 88 (1964).

[93] K. A. Rakhmatulin and Y. A. Dem'yanov, *Strength under high transient loads* (Coronet Books Inc, 1966).

[94] S. S. Antman, The American Mathematical Monthly **87**, 359 (1980).

[95] K. Naugolnykh and L. Ostrovsky, *Nonlinear Wave Processes in Acoustics* (Cambridge University Press, 1998) p. 298.

[96] L. Wang, *Foundations of stress waves* (Elsevier, 2011).

[97] K. A. Rakhmatulin, Prikl. Mat. Mekh **9**, 449 (1945).

[98] J. W. Craggs, Journal of the Mechanics and Physics of Solids **2**, 286 (1954).

[99] G. V. Anand, The Journal of the Acoustical Society of America **45**, 1089 (1969).

[100] R. V. Goldstein, Y. A. Dem'yanov, L. V. Nikitin, N. N. Smirnov, and E. I. Shemyakin, Mechanics of Solids **45**, 3 (2010).

[101] V. F. Nesterenko, Fizika gorenia i vzryva (in Russian) **28**, 121 (1992).

[102] J. D. Cole, C. B. Dougherty, and J. H. Huth, Journal of Applied Mechanics **20**, 519 (1953).

[103] J. B. Marion and S. T. Thornton, *Classical dynamics of particles and systems* (1995).

[104] B. Song, H. Park, W.-Y. Lu, and W. Chen, Journal of Applied Mechanics **78**, 51023 (2011).

[105] S. Ulrich, N. Upadhyaya, B. V. Opheusden, and V. Vitelli, Proceedings of the National Academy of Sciences **2013**, 1 (2013).

Samenvatting

Systemen van mechanische metamaterialen die topologisch zijn met betrekking tot lineaire golven kunnen grote niet-lineaire deformaties ondergaan. De wisselwerking tussen deze niet-lineaire deformaties en de topologie van het systeem beïnvloedt de geleiding van geluidsgolven door het materiaal. Defecten in de orde van het systeem bieden de mogelijkheid om de eigenschappen van het materiaal te beïnvloeden. Tevens kunnen deze defecten interactie hebben met niet-lineairiteiten in het systeem en met de bulk topologie van het systeem. Om dit beter te begrijpen bekijken we deze effecten in drie verschillende mechanische systemen: eenling-golven in topologische rotorketens, roostergolven in gedraaide Kagome netwerken en dwarse schokgolven in flexibele snaren.

In hoofdstuk 2 bestuderen we de volledige niet-lineaire dynamica van topologische rotorketens. Met behulp van de continuümbeschrijving, leiden we een niet-lineaire veldentheorie af die topologische kinks, antikinks en niet-lineaire excitaties toelaat. Een topologische grensterm in de Lagangriaan breekt de symmetrie tussen de kink en antikink configuratie. Deze asymmetrie komt aan het licht als de propagatie van (anti)kinks wordt bekeken. In hoofdstuk 3 laten we zien hoe deze asymmetrie zich manifesteert als niet-lineaire excitaties wisselwerken met onzuiverheden in de keten.

Om soortgelijke niet-lineaire gedragingen in hogere ruimtelijke dimensies te kunnen onderzoeken, willen we eerst het gedrag in het lineaire regime begrijpen. Gedeformeerde Kagome roosters staan er om bekend topologische fases te vertonen en hebben configuraties waar niet-lineaire effecten niet achterwege gelaten kunnen worden. In hoofdstuk 4 bekijken we de lineaire mechanische golven in gedraaide Kagome roosters. In het perfecte rooster

blijkt dat het draaimechanisme de fononische bandenstructuur beïnvloedt door de bandkloven te vergroten. Bij een kritische draaihoek zien we een verrassende dubbele ontaarding in de fononische banden, wat gerelateerd lijkt aan het orthogonaal worden van de roosterbindingen. In hoofdstuk 5 introduceren we puntdefecten in de roosters. Niet-lineaire eigentrillingen van de defecten die ruimtelijk gelokaliseerd en spectraal geïsoleerd zijn verschijnen in de bandkloof. Met behulp van het "tight-binding"-elektronenmodel beschrijven we de hybridisatie van deze eigentrillingen.

Voor het reguliere Kagome rooster zijn er volledige rijen van atomen die gelijkgericht zijn wat nulwaardige eigentrillingen veroorzaakt. Deze nulwaardige eigentrillingen zijn gerelateerd aan het ontkoppelen van de vrijheidsgraden die alleen voorkomen in het lineaire regime. Hierdoor verwachten we dat de niet-lineairiteiten de materiaaleigenschappen veranderen. Om de volledige niet-lineaire analyse van de Kagome roosters te doen, focusseren we eerst op een simpeler één-dimensional model dat alle belangrijke eigenschappen reproduceert. In hoofdstuk 6 beschrijven we de geleiding van dwarse-schokgolven in ongespannen flexibele snaren bij een punt-inslag. We formuleren een theorie — voor het continue en discrete geval — die aanneemt dat de trage transversale golven achterblijven in de regio die verstoord is door de snellere longitudinale golven. Deze theorie voorspelt dat er een machtsverband is tussen de snelheden van de schok en de inslag. Dit verband is bevestigd door numerieke simulaties.

List of Publications

1. Y Zhou, BG Chen, N Upadhyaya, and V Vitelli.
   Kink-antikink asymmetry and impurity interactions in topological mechanical chains,
   Physical Review E 95(2), 022202 **2017**.

2. Y Zhou and W Hu.
   Kinetic analysis of quasi-one-dimensional growth of polymer lamellar crystals in dilute solutions,
   The Journal of Physical Chemistry B 117(10), 3047 **2013**.

3. L Zhao, H Yang, Y Song, Y Zhou, G Hu, and Q Zheng.
   Non-linear viscoelasticity of vapor grown carbon nanofiber/polystyrene composites,
   Journal of Materials Science 46(8), 2495 **2010**.

Curriculum Vitæ

I WAS BORN in the city of Hangzhou, Zhejiang province, China in September 1987. September 2003, I went to XueJun High School in Hangzhou. July 2010, I received my bachelor degree in polymer engineering at Zhejiang University. July 2013, I obtained my master's degree in polymer science at Nanjing University. September 2013, I started working with (now prof.) dr. Vincenzo Vitelli as a Doctor of Philosophy (Ph. D.) student at Leiden University.

Acknowledgements

The author thanks his supervisor Vincenzo Vitelli for directing the whole process of this PhD study. The writing of this thesis was supported by many people, to whom the author expresses gratitude. The work in Chapters 2 and 3 was done with Bryan G. Chen and Nitin Upadhyaya. The work in Chapters 4 and 5 received assistance from Michel Fruchart and Jayson Paulose. The work in Chapter 6 was aided by Anton Souslov and Jayson Paulose. The author shows appreciation to Michel Fruchart and Anton Souslov for proofreading the thesis, and acknowledges the help from Benny van Zuiden and Ke Liu in configuring LaTeX.